Internal Report
DESY F31-86-02
April 1986

A STUDY OF THE RADIATIVE CASCADE TRANSITIONS BETWEEN THE UPSILON-PRIME AND UPSILON RESONANCES

by

T. Skwarnicki
Institut of Nuclear Physics, Cracow
and
Deutsches Elektronen-Synchrotron DESY, Hamburg

ISSN 0418-9833

A STUDY OF THE RADIATIVE CASCADE TRANSITIONS BETWEEN THE UPSILON-PRIME AND UPSILON RESONANCES

Tomasz Skwarnicki

Institute of Nuclear Physics, Cracow
and
Deutsches Electronen-Synchrotron DESY, Hamburg

February 1986

Ph.D. dissertation
at Cracow Institute of Nuclear Physics

This study was performed within the Crystal Ball Collaboration :

D. Antreasyan, D. Aschman, D. Besset, J. K. Bienlein, E. D. Bloom, I. Brock, R. Cabenda, A. Cartacci, M. Cavalli-Sforza, R. Clare, G. Conforto, S. Cooper, R. Cowan, D. Coyne, D. de Judicibus, C. Edwards, A. Engler, G. Folger, A. Fridman, J. Gaiser, D. Gelphman, G. Godfrey, F. H. Heimlich, R. Hofstadter, J. Irion, Z. Jakubowski, S. Keh, H. Kilian, I. Kirkbride, T. Kloiber, W. Koch, A. C. Kõnig, K. Kõnigsmann, R. W. Kraemer, R. Lee, S. Leffler, R. Lekebusch, P. Lezoch, A. M. Litke, W. Lockman, S. Lowe, B. Lurz, D. Marlow, W. Maschmann, T. Matsui, F. Messing, W. J. Metzger, B. Monteleoni, R. Nernst, C. Newman-Holmes, B. Niczyporuk, G. Nowak, C. Peck, P. G. Pelfer, B. Pollock, F. C. Porter, D. Prindle, P. Ratoff, B. Renger, C. Rippich, M. Scheer, P. Schmitt, M. Schmitz, J. Schotanus, A. Schwarz, D. Sievers, T. Skwarnicki, K. Strauch, U. Strohbusch, J. Tompkins, H.-J. Trost, R. T. Van de Walle, H. Vogel, U. Volland, K. Wacker, W. Walk, H. Wegener, D. Williams, P. Zschorsch.

All these people contributed to the data taking, hardware and software maintenance. Whenever we explicitly used somebody else's work in our off-line data analysis we supplied a reference or footnote. Otherwise the author is solely responsible for the failures or mistakes.

The main research was done at DESY in Hamburg. Some work was also performed at Cracow Institute of Nuclear Physics. Prof. K. Rybicki was supervisor in writing this thesis up.

ABSTRACT

The cascade reaction $e^+e^- \to \Upsilon' \to \gamma\chi_b \to \gamma\gamma\Upsilon \to \gamma\gamma(\mu^+\mu^-$ *or* $e^+e^-)$ has been studied with the Crystal Ball detector at the e^+e^- storage ring DORIS-II. Two χ_b states are observed by monoenergetic photon lines at $107.7 \pm 1.1 \pm 1.0$ MeV and $132.4 \pm 0.9 \pm 1.0$ MeV, with amplitudes of 56 ± 6 and 82 ± 10 events correspondingly. Upper limits for full widths of those states at 90 % confidence level are < 6.2 MeV and < 6.9 MeV respectively.

Angular correlations among the final state particles are fully consistent with spin 2 of the higher mass χ_b state, spin 1 of the lower mass χ_b state and the pure dipole radiative transitions, although some other possibilities cannot be excluded. Spin 0 can be ruled out for both χ_b states. In addition, assuming pure dipole radiative transitions, we also show that it is not possible to assign, at the same time, spin 1 to the higher mass χ_b state and spin 2 to the lower mass χ_b state.

The cascade branching ratios $BR(\Upsilon' \to \gamma\chi_b)\cdot BR(\chi_b \to \gamma\Upsilon)\cdot BR(\Upsilon \to l^-l^-)$ are found to be $(4.6 \pm 0.7 \pm 0.5)\cdot 10^{-4}$ for the spin 2 χ_b state, and $(6.0 \pm 0.7 \pm 0.7)\cdot 10^{-4}$ for the spin 1 χ_b state. Upper limit for the spin 0 χ_b state at 90 % confidence level is $< 4 \cdot 10^{-5}$. Combining the above values with the world average value for $BR(\Upsilon \to l^+l^-)$ and with the inclusive results for $BR(\Upsilon' \to \gamma\chi_b)$, we obtain branching ratios for $\chi_b \to \gamma\Upsilon$.

Potential models, QCD sum rules and bag model predictions for the χ_b masses and their fine structure are compared with our results. Hadronic widths of the χ_b states derived from $BR(\chi_b \to \gamma\Upsilon)$ with help of the potential models are used to test the QCD predictions.

STRESZCZENIE

Detektor Crystal Ball został użyty do badania reakcji kaskadowej $e^+e^- \to \Upsilon' \to \gamma\chi_b \to \gamma\gamma\Upsilon \to \gamma\gamma(\mu^+\mu^-$ *or* $e^+e^-)$ na pierścieniu wiązek elektronowo-pozytronowych DORIS-II. Zaobserwowaliśmy dwa stany χ_b poprzez monoenergetyczne linie fotonów o energiach $107.7 \pm 1.1 \pm 1.0$ MeV i $132.4 \pm 0.9 \pm 1.0$ MeV oraz o odpowiadających amplitudach 56 ± 6 i 82 ± 10 przypadków. Górne granice pełnej szerokości tych stanów wynoszą : < 6.2 MeV i < 6.9 MeV, przy poziomie ufności 90 %.

Korelacje kątowe pomiędzy cząstkami stanu końcowego są w pełni zgodne ze spinem 2 stanu cięższego i spinem 1 stanu lżejszego, oraz z czysto dipolowymi przejściami fotonowymi, aczkolwiek nie wszystkie alternatywne możliwości mogą być wykluczone. Pokazujemy, że spiny obydwu zaobserwowanych stanów są różne od zera. Zakładając wyłącznie dipolowe przejścia radiacyjne, pokazujemy, że nie jest możliwe przypisanie jednocześnie spinu 1 do stanu o większej masie i spinu 2 do stanu o mniejszej masie.

Iloczyn częstości rozpadów $BR(\Upsilon' \to \gamma\chi_b)\cdot BR(\chi_b \to \gamma\Upsilon)\cdot BR(\Upsilon \to l^-l^-)$ wynosi $(4.6 \pm 0.7 \pm 0.5)\cdot 10^{-4}$ dla stanu o spinie 2, oraz $(6.0 \pm 0.7 \pm 0.7)\cdot 10^{-4}$ dla stanu o spinie 1. Górna granica dla stanu o spinie 0 przy poziomie ufności 90 % wynosi $< 4 \cdot 10^{-5}$. Łącząc powyższe wyniki w kanale ekskluzywnym z inkluzywnymi rezultatami o rozpadzie $\Upsilon' \to \gamma\chi_b$, oraz ze średnią światową wartością na $BR(\Upsilon \to l^+l^-)$ uzyskujemy częstości rozpadów $\chi_b \to \gamma\Upsilon$.

Przewidywania modeli potencjalnych, chromodynamicznych reguł sum i modeli worków na masy i strukturę subtelną stanów χ_b są porównane z naszymi wynikami. Przy pomocy modeli potencjalnych uzyskujemy hadronowe szerokości stanów χ_b z częstości rozpadów $\chi_b \to \gamma\Upsilon$. Porównujemy je z przewidywaniami chromodynamiki kwantowej.

TABLE OF CONTENTS

I. INTRODUCTION

I.1. Heavy Quarkonia

A great success of the electron-positron storage rings in high energy physics has been stimulated to a large extent by their suitability for studying vector mesons. The quantum numbers of vector mesons are identical to those of photon, i.e. $J^{PC} = 1^{--}$, therefore virtual photons from e^+e^- annihilation can directly convert into these states. The simplicity of the formation process results in clean resonance signals.

The existence of vector states in heavy quarkonia proved especially advantageous. Although the fixed target experiments, with incident proton beam on nuclear target, played an important role in the discoveries of the ψ[1] and Υ[2] systems, e^-e^- collisions provided almost all presently available information about features of these states.

The heavy quarkonia occur as families of resonances, which are close in mass. The lighter resonances are extremely narrow, contrary to the heavier ones, which exhibit larger total widths, typical for the strongly decaying particles. This feature found a natural explanation in the quarkonium model[3], which recognizes the ψ and Υ families as bound states of heavy quark-antiquark pairs with the same flavour : charm (c-quark) and bottom (b-quark) correspondingly. The states with masses below the threshold for the decay into a pair of mesons, each with only one heavy quark (D and B mesons), must be narrow, since their hadronic decays are suppressed by the OZI rule[4]. The mass differences between members of the quarkonium family are small compared to the masses themselves, indicating that constituent quarks are heavy, i.e. their interaction can be treated in a simple nonrelativistic manner. A number of potentials have been proposed to describe the interquark forces. The potential models give very good quantitative description of the heavy quark systems, providing convincing evidence for the quark structure of hadrons. There is a great hope that heavy quarkonia, thanks to their simplicity, will also efficiently test the theory of the quark dynamics — QCD. The basic challenge is to establish the Coulombic behaviour of the interquark potential at the short distance, predicted by the one gloun exchange picture. This ambitious program calls for extensive experimental data on the heavy quark systems.

The ψ family is well known experimentally. Unfortunately it is not well suited for the

QCD tests. The spatial dimensions of the $c\bar{c}$ bound states seem to be too large to probe the short range potential, indicating that the c-quark is still not heavy enough[1]. The precision of theoretical predictions is also often affected by non-negligible relativistic corrections. The b-quark is approximately 3 times heavier than the c-quark. Thus $b\bar{b}$ spectroscopy appears to be more promising.

I.2. $b\bar{b}$ Spectroscopy

As quarks are spin $\frac{1}{2}$ objects, the $b\bar{b}$ bound states form a positronium-like spectrum. Energy levels may be classified with use of three quantum numbers : n - counting the radial excitations (n=1,2,3 ...), L - describing the orbital excitations (L=S,P,D ...) and S - superposition of the quark spins (S=0 or 1). The total spin of the resonance is $\vec{J} = \vec{L} + \vec{S}$ ($|L - S| \leq J \leq |L + S|$), and the parities are : $P = (-1)^{L+1}$, $C = (-1)^{L+S}$. We will use the spectroscopic symbol $n^{2S+1}L_{J^{PC}}$ to denote the $b\bar{b}$ levels. The mass level scheme for the $b\bar{b}$ system predicted by a succesful model[6] is shown in Fig.1.

Most of the experimental data concerns the $n^3S_{1^{--}}$ resonances. Thanks to their quantum numbers and sizable wave function at origin[2], they couple to e^+e^- pairs. At least five states of this kind have been observed as bumps in the hadronic cross section in e^+e^- annihilation[8]. States with different quantum numbers can be studied at e^+e^- machines only if they result from decays of the $^3S_{1^{--}}$ resonances. Such a study is the topic of this work.

The three lowest $^3S_{1^{--}}$ states Υ, Υ' and Υ'' lie below the $B\bar{B}$ threshold. Their hadronic decays are therefore suppressed and the electromagnetic transitions become detectable.

The heavy b-quark mass has a large impact on a structure of the photon transitions. Sizes of the $b\bar{b}$ quarkonia are small compared to the photon wave lengths, thus the dipole transitions dominate[3]. The magnetic dipole transition (M1) must be much weaker than the electric dipole ones (E1). They were weak already in the $c\bar{c}$ quarkonium[12]. Further suppression is expected for the $b\bar{b}$ system[4].

[1] For the scaling law with quark quark mass see, for example, Ref.5 p. 186.

[2] $\Gamma_{ee} \propto \phi(0)^2$. Γ_{ee} - leptonic width of the $b\bar{b}$ state, $\phi(r)$ - radial wave function of the bound state (see e.g. Ref.7).

[3] $\Gamma_L/\Gamma_1 \propto (R/2\lambda)^{2L}$, Γ_L - width for the L-pole transition (see e.g. Ref.7). Taking for instance the radiative decays of the Υ', which will be discussed later; $R \equiv \sqrt{< r^2 >} \simeq 0.5$ fm (see e.g. Ref.9) and $\lambda = 1/E_\gamma \simeq 2.0$ fm, so $R/2\lambda = 1/8$.

[4] Γ_{M1}/Γ_{E1} scales like E_γ/m_Q, where m_Q is a quark mass (see e.g. Ref.7).

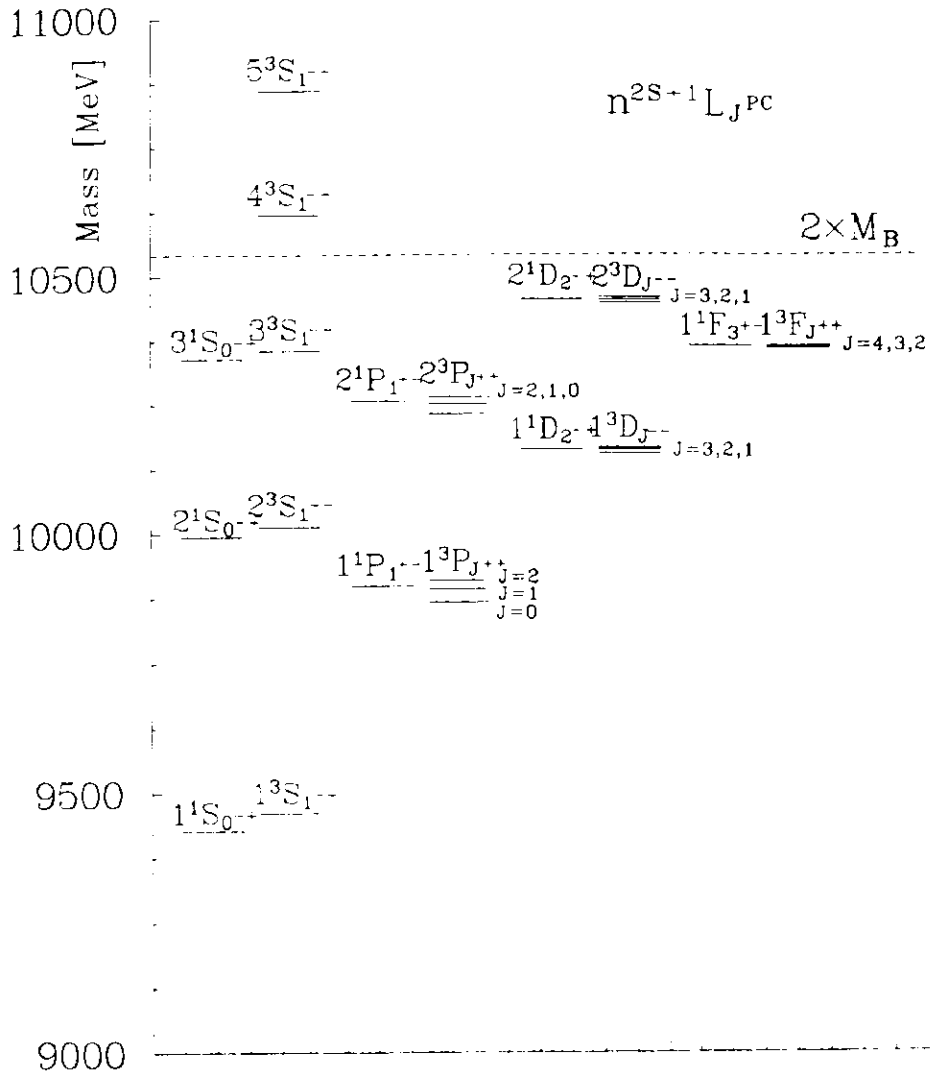

Figure 1.
The mass spectrum of $b\bar{b}$ bound states below the $B\bar{B}$ threshold (the dashed line) predicted by the potential model (Ref.6). The measured masses of 4S and 5S resonances are also indicated.

The C-parity of photon is negative, allowing electromagnetic transitions only between levels of the opposite charge conjugation. The electric dipole transitions require, in addition, a change of the P-parity. From figure 1, one sees that only the $1^3P_{J^{++}}$ and $2^3P_{J^{++}}$ states (J=0,1,2) can be produced by the electric dipole radiative decays of the Υ' ($2^3S_{1^{--}}$) and Υ'' ($3^3S_{1^{--}}$) resonances. They can subsequently decay radiatively into the lower $^3S_{1^{--}}$ states. Experimental candidates for the triplet P-states are called χ_b and χ_b' respectively. We will concentrate on the $1^3P_{J^{++}}$ states.

There are two experimental ways of studying these transitions. An inclusive analysis of photons from hadronic events coming from the Υ' decays may reveal monochromatic γ-lines corresponding to the $2S \xrightarrow{\gamma} 1P$ transitions and Doppler-broadened peaks due to the $1P \xrightarrow{\gamma} 1S$ radiative decays. The cascade transition $2S \xrightarrow{\gamma} 1P \xrightarrow{\gamma} 1S$ can also be detected in an exclusive mode by identifying the $\Upsilon(1S)$ by its leptonic decay $\Upsilon \rightarrow (\mu^+\mu^- \text{ or } e^+e^-)$.

The first experimental evidence for the existence of the χ_b and χ_b' states has been reported by CUSB experiment at the e^+e^- storage ring CESR[13,14,15,16]. Some results on the χ_b states came also from the CLEO experiment at CESR[17]. A parallel study of the χ_b states, with somewhat improved precision, has been performed by two other experiments, CRYSTAL BALL and ARGUS[18], at the e^+e^- storage ring DORIS-II.

We present here a study of the radiative cascade transitions $\Upsilon' \xrightarrow{\gamma} \chi_b \xrightarrow{\gamma} \Upsilon$ using the exclusive sample of $\gamma\gamma\mu^+\mu^-$ and $\gamma\gamma e^+e^-$ events collected by the Crystal Ball detector.

The event statistics in this channel suffer from the small branching ratio $\Upsilon' \rightarrow l^+l^-$ $(2.8 \pm 0.3)\%$ [19]. However the χ_b signals are practically background free, contrary to the inclusive photon analysis, which copes with the high background. This allows, for example, determination of the spins of the χ_b states by studying the angular correlations. Special attention is payed to that topic in our analysis, as the other detectors could not attempt this kind of study.

Measuring energies of the photon transitions one finds the χ_b masses, which are very interesting from the theoretical point of view. The sizes of these states, as calculated in the potential models, are the second smallest among the known quarkonia states[9] :

$$\langle r^2\rangle_\Upsilon^{1/2} \simeq 0.23 \text{ fm} \quad < \quad \langle r^2\rangle_{\chi_b}^{1/2} \simeq 0.39 \text{ fm} \quad < \quad \langle r^2\rangle_{J/\psi}^{1/2} \simeq 0.42 \text{ fm}$$

therefore the mass difference M_{χ_b}-M_Υ may be sensitive to the small distance potential. The mass splitting of the triplet χ_b states, corresponding to the fine interaction, gets a contribution

from the short range interaction and the long distance confining forces, as well. It provides valuable information about the spin dependence of the confining interaction, which is difficult to deduce on purely theoretical ground.

The energy resolution of the existing detectors is not good enough to resolve the Doppler-broadened peaks due to the $\chi_b \rightarrow \gamma\Upsilon$ transitions in the inclusive γ analysis. Therefore, the product branching ratios $BR(\Upsilon' \rightarrow \gamma\chi_b)\cdot BR(\chi_b \rightarrow \gamma\Upsilon)$ can be measured only in the exclusive cascade channel. This gives, together with the inclusive results for $BR(\Upsilon' \rightarrow \gamma\chi_b)$, the unique opportunity to obtain $BR(\chi_b \rightarrow \gamma\Upsilon)$. These branching ratios can be related to the hadronic widths of the χ_b states, leading to the quantitative tests of the QCD predictions based on multigluon annihilation graphs.

Only two of the three χ_b states are observed in the exclusive channel with the presently available statistics. The cascade transitions via the spin 0 χ_b state are suppressed due to the small value of $BR(\chi_b^{J=0} \rightarrow \gamma\Upsilon)$. The third χ_b state has been detected in the inclusive photon analysis, which benefits from the higher experimental rates, but suffers from the higher background.

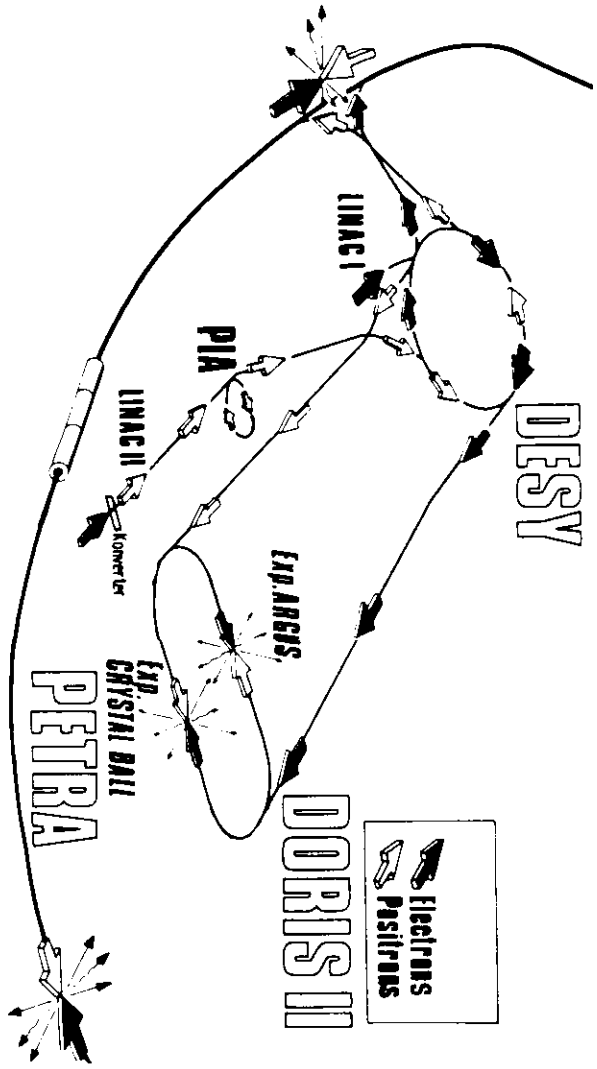

Figure 2.
The acceleration system at DESY.

II. EXPERIMENTAL LAYOUT

The electromagnetic radiative transitions are a fruitful source of information about structure and properties of the quarkonium levels below the flavour threshold. To take advantage of this, highly optimized photon detectors are needed. The Crystal Ball detector is such a device.

The Crystal Ball detector demonstrated its abilities exploring charmonium physics during 3 years of operation at SPEAR (starting at the end of 1978). As far as the radiative transitions between $c\bar{c}$ levels are concerned, it provided high precision measurements of the reactions[11,21] $\psi' \to \gamma\chi_c$ and $\chi_c \to \gamma\psi$. The χ_c spins were established by study of the exclusive cascade events[21]. In addition, the pseudoscalar states η_c and η_c' were discovered by observation of rare M1 transitions[12] : $\psi' \to \gamma\eta_c$, $\psi' \to \gamma\eta_c'$, $\psi \to \gamma\eta_c$.

In the beginning of 1982 the Crystal Ball detector was moved to the DORIS-II e^+e^- storage ring to perform analogous studies of the $b\bar{b}$ quarkonium, with the Υ' decays as a first goal.

II.1. DORIS-II

An electron and a positron, each with an energy of half the Υ' mass ($M_{\Upsilon'}$=10.023 GeV), can annihilate in head-on collisions, producing an Υ' at rest. The acceleration system at DESY is shown in Fig.2. Electrons are produced in hot filaments at the entries to the two linear accelerators. Electrons in the LINAC-II are directed into a tungsten target to create positrons. The positron beam is accumulated in the small intermediate storage ring PIA (**P**ositron **I**ntensity **A**ccumulator) to increase its intensity. Electrons from the LINAC-I and positrons from the LINAC-II, accelerated up to about 450 MeV, are injected to the DESY synchrotron (**D**eutsches **E**lectronen-**SY**nchrotron), which brings their energy up to about 5 GeV. The electron and positron beams are then transferred to the DORIS[1] storage ring, where they circulate and collide at two interaction points. The interaction regions are occupied by the Crystal Ball and ARGUS detectors.

DORIS has been in operation since 1974. It was initially designed for a maximum beam energy of 3.5 GeV, with a double ring structure (**DO**uble **RI**ng **S**torage facility), and

[1] DESY is used also as an injector for the PETRA storage ring.

multibunch operation[22]. In 1978 the two rings were combined into one ring, with single-bunch beams, to reach energy of the Υ and Υ', namely 5.1 GeV per beam (DORIS-I storage ring)[23]. This was rather temporary solution, because the maximum luminosity was only $1 \cdot 10^{30}$ cm^{-2}sec^{-1} with high power consumption of 10.8 MW (at 5.1 GeV). DORIS was rearranged again in 1982[24]. The bending power of the magnets was increased, allowing a maximal energy of 5.6 GeV. Several improvements brought the power consumption down to half of that of DORIS-I. High luminosity L > 10^{31} cm^{-2}sec^{-1} around 5 GeV region was obtained by the installation of mini-beta quadrupoles[1]. A new vacuum system for DORIS-II gives an average pressure of $2-8 \times 10^{-9}$ mbar depending on the beam current. Typical operation involve beams with lifetimes of 2-3 h, injected with currents of 2 × 30 mA, giving an integrated luminosity delivered by the machine of 600 nb^{-1} per day. The record score of more than 1000 nb^{-1} per day was achieved. The integrated luminosity per week, accepted by the Crystal Ball experiment during the Υ' run, is plotted in Fig.3.

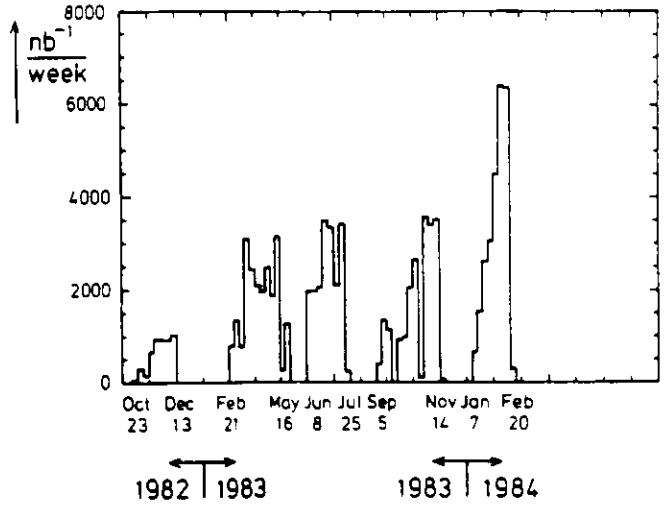

Figure 3.
Integrated luminosity per week collected by the Crystal Ball experiment during the period of Υ' run.

[1] Mini-beta quadrupoles improve beam focusing at the interaction points.

The natural width of the Υ' resonance ($\Gamma_{\Upsilon'} \simeq 30$ keV) is negligible in comparison with the beam energy spread at e^+e^- storage rings, thus the width and height of the observed resonance peak is a feature of the colliding beam machine. The beam energy spread of the DORIS-II (FWHM 9.6 MeV) results in ~3 nb resonance cross section on the Υ' peak, over ~3 nb continuum (Fig.4).

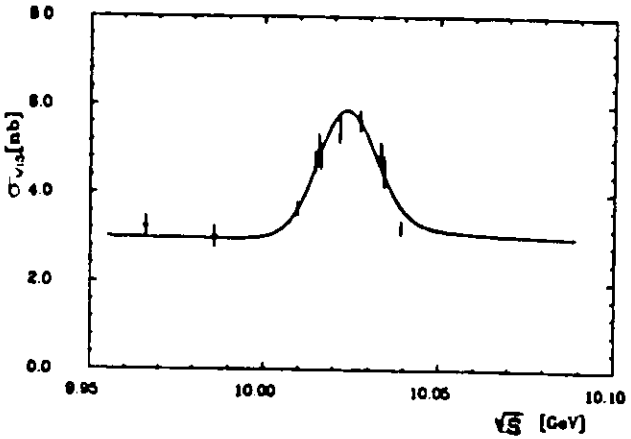

Figure 4.
The visible hadronic cross section of e^+e^- annihilation in the region of Υ' resonance at DORIS-II, as measured by the Crystal Ball experiment (Ref.25).

The longitudinal size of the electron bunches causes a spread of the interaction point along the beam axis. The spread is approximately gaussian with $\sigma \approx 1.5$ cm.

Electrons and positrons in the DORIS-II storage ring become polarized as a result of emission of synchrotron radiation according to the Sokolov-Ternov effect[26]. The polarization direction is parallel to the magnetic field of bending magnets, thus transverse to the beam direction. The maximum achievable polarization due to this mechanism is ~92 %. Beam polarization is limited[27] by the synchrotron radiation itself. Sudden energy loss by photon emission causes change of the particle orbit, which destroys correlation between orbital and spin motions. Also, unavoidable vertical misalignment of the storage ring components makes beam particles influenced by the depolarizing radial fields of the quadrupoles. Similarly, beam-beam forces at the interaction point cause depolarization. Finally, the solenoid field

of the ARGUS magnet, which is only partially compensated (87 %), acts to destroy the polarization. As a result of these depolarization effects, the beam polarization does not reach the theoretical limit. At certain beam energies, where depolarizing machine resonances occur, the beam polarization can be destroyed completely. Theoretical calculations for DORIS-II have shown [28] that beam polarization at the Υ' energy may be pretty high. In fact, we measured average beam polarization of (75±5)% for the Υ' data, as described in Appendix G. The beam polarization was very helpful in the spin determination of the χ_b states, as discussed in Appendix J.

II.2. The Crystal Ball Detector

The major component of the detector is an array of scintillating crystals. Its spherical design takes good advantage of the e^+e^- collisions, which are observed in the center of mass frame (Fig.5). The NaI(Tl) crystals, used as the scintillator, ensure good energy resolution for electromagnetically showering particles :

$$\frac{\sigma_E}{E} = \frac{2.8\ \%}{\sqrt[4]{E}} \qquad E \text{ in GeV} \tag{II.2-1}$$

They allow resolution of fine structure of the spin triplet χ_b states, thus playing a crucial role in this analysis.

The Crystal Ball geometry is based on a 20-sided regular polyhedron. Each of 20 major triangles (Fig.6) is subdivided into 4 minor triangles with vertices lying on the spheres. The radius of the inner sphere is 25.4 cm and that of the outer sphere is 66.0 cm, thus corresponding to 15.7 radiation lengths and 1.0 nuclear interaction length. Further subdivision of the minor triangles into 9 individual modules gives 720 crystals, which would cover the full solid angle. Six minor triangles on each side were removed to permit beam pipe entrance. The two layers of crystals closest to the beam pipe are called "the tunnel region" in the Crystal Ball terminology.

The ball proper covers 94 % of the entire solid angle. The solid angle coverage is increased to 96 % of 4π by the endcap NaI(Tl) counters. The endcap crystals, of hexagonal shape, are stacked perpendicularly to the beam pipe (radial space is limited by the DORIS-II mini-beta magnets), providing 3 – 9 radiation lengths. Solid angle which can be used for a good energy measurement of the electromagnetically showering particles is somewhat smaller, due to the

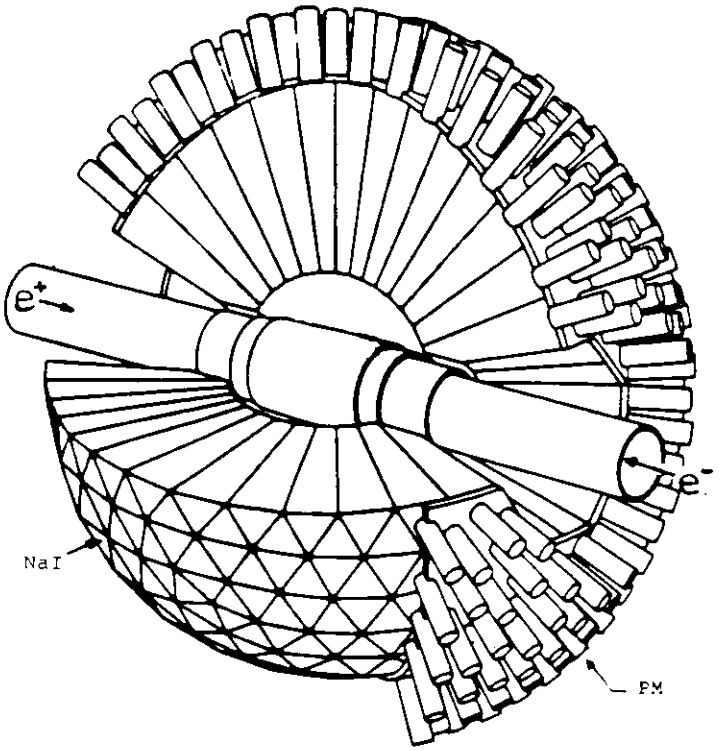

Figure 5.
The Crystal Ball detector.

edge effects.

More details of the Crystal Ball detector can be found in Ref.20.

The large uniform solid angle coverage provides the high geometric acceptance especially important for exclusive state studies, such as presented here. It also allows simple and reliable event triggering, based on energy depositions in the calorimeter.

The thickness of the ball proper sufficies for nearly 100 % absorption of an electromagnetic shower over 4 orders of magnitude in energy (~ 0.5 MeV-5.0 GeV).

The high degree of detector segmentation results in good photon direction reconstruc-

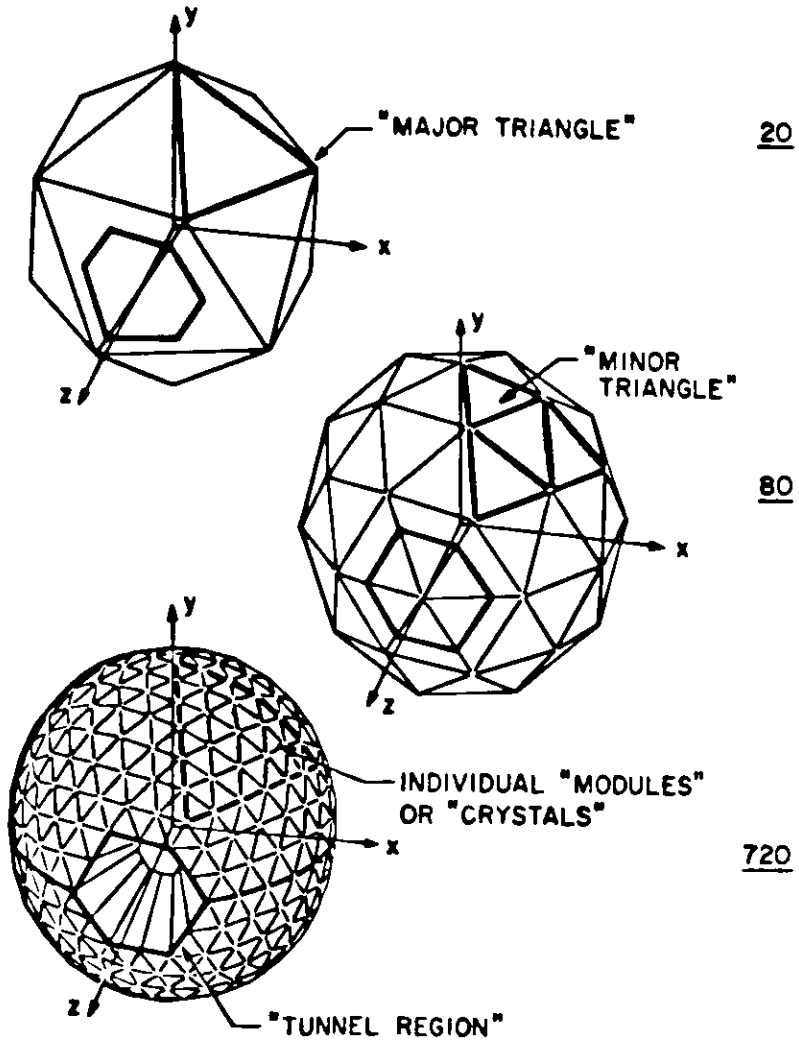

Figure 6.
The Crystal Ball geometry.

tion and in good resolution of overlapping particles. It allows, in addition, some particle identification by pattern recognition techniques of energy depositions.

Photons and electrons initiate electromagnetic showers in the Crystal Ball detector and deposite their total energy in 3 layers of crystals around the entry point. Muons do not initiate a shower, but pass through the detector leaving only about 210 MeV from ionization in very few crystals. Hadrons such as pions and kaons behave like muons unless they undergo nuclear interaction in the crystal. Nuclear interaction leads to an irregular energy deposition depending on the behaviour of the secondary particles in the detector.

Although only the electromagnetic calorimeter is used to select $\gamma\gamma l^+l^-$ events, we will also describe the other detector components, since they are used in some of our auxiliary analyses.

II.3. Tube Chambers

Inside the ball a set of proportional tube chambers was installed as a charge tracking device. About[1] 600 aluminium tubes, with stainless steel anode wires, were arranged in 3 double layers[2] (Fig.7). The tubes of ~5 mm diameter had a wall thickness of 0.08 mm. The conversion probability of a photon was about 5 % (including conversion at the beam pipe). The innermost radius of the chamber was 6.2 cm and of the outermost one 14.3 cm. The active lengths of the layers were 69, 53 and 36 cm respectively, which corresponded to solid angle coverage of 98, 96 and 75 %. The chambers were initially operated with "magic" gas (51 % Argon, 25 % Freon, 20 % Isobutane, 4 % Methylal), giving a large gas amplification. Because of high radiation background near the beam pipe, the chambers were quickly wearing out, therefore the magic gas was replaced by Ar-CO_2 gas mixture.

The chambers were calibrated with Bhabha events. Charge division readout allowed hit position measurement along the tubes, with a resolution of 1-2 % of the active lengths. The resolution in azimuthal angle was σ_φ=11-23 mrad. The efficiency of each double layer was typically 80-90 %, dropping down to 20-40 % in some periods of bad performance. The overall efficiency of the tracking system was always above 90 %.

[1] Three different geometrical set-ups, with slightly different numbers of tubes, were used during the Υ′ run.
[2] Since summer 1984, the Crystal Ball operates with 4 double layers of the tube chambers.

More details of the chambers may be found in Ref.29.

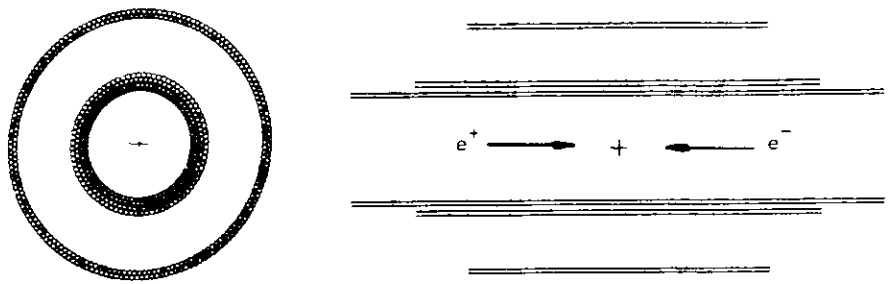

Figure 7.
The end view and side view of the tube chambers.

II.4. Time of Flight System

An array of 94 scintillation counters was installed above the Crystal Ball detector (Fig.8) to provide a shield against the cosmic background with use of the Time of Flight method. The distance between the interaction point and the ToF counters ranges from 3 to 5 m. The counters are 3.2 or 1.7 m long. They cover about 25 % of the solid angle, allowing rejection of ~80 % of cosmic background. Photomultipliers viewing each end of the counter provide two outputs. The anode output is used for a time measurement. The last dynode output is used to measure a pulse height.

The counters are calibrated with cosmic muons. A hit position along the counter is measured by the time difference at two ends of the counter, and by the pulse height ratio, with an accuracy of ~15 cm. The width of the pulse height distribution for minimum ionizing particles is 30 % (FWHM). Timing of the hit is calculated with a precision of 0.5 ns.

The ToF method needs a second time measurement along the track, in addition to that

measured with the ToF counters. The NaI crystals are used for that purpose. The achieved time resolution from the Crystal Ball detector is energy dependent : from 0.28 ns for high energy showers, to 0.80 ns for minimum ionizing particles.

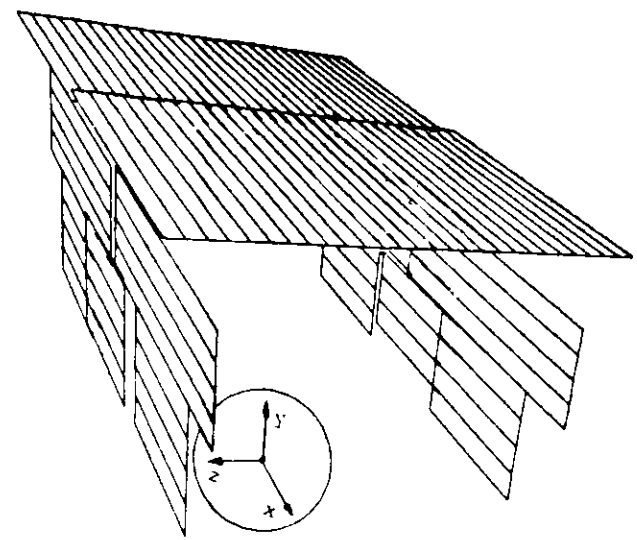

Figure 8.
The ToF counters.

III. DATA PROCESSING

The data used in this analysis were collected between October 1982 and February 1984. In total, 63 pb^{-1} of integrated luminosity were accumulated on the Υ' resonance, during 175 days of the data taking[1].

III.1. Trigger

The triggering system was based on fast analog sums of energies left in the NaI crystals. Only triggers relevant for the detection of the $\Upsilon' \to \gamma\gamma\Upsilon \to \gamma\gamma(\mu^+\mu^-$ *or* $e^+e^-)$ events will be described here.

The $\gamma\gamma e^+e^-$ events were easy to trigger on, due to the large energy deposition by the electrons. If energy deposited in the main ball (excluding the tunnel region and the endcaps) exceeded ~1700 MeV, within a time gate of ±25 ns with respect to the beam crossing, the trigger was satisfied.

Low total energy deposition by the $\gamma\gamma\mu^+\mu^-$ events, typical also for beam gas events, demanded more sophisticated triggers. In addition to a lowered total energy threshold and the time coincidence with the beam collisions, some topological patterns of the energy recorded in the ball had to be fulfilled.

The e^+e^- annihilation is observed in the center of mass frame. Therefore, momenta of the final state particles add up to zero. The beam gas events do not exhibit such a momentum balance. Using the major triangle structure (see section II.2), the Crystal Ball was divided into two opposite hemispheres in 11 different ways to trigger on events with balanced momentum. Each of the resulting 22 hemispheres had to have at least one major triangle with more than ~160 MeV (Fig.9). The total energy sum had to be above ~800 MeV. This topological trigger was 90 % efficient for $\gamma\gamma\mu^+\mu^-$ cascade events[2].

The trigger efficiency for this type of events was increased up to 97 % by the "μ-pair trigger". It was designed to pick-up events with the back-to-back energy clusters, as for example a pair of muons from the Υ decay in the cascade process. Two back-to-back or

[1] All numbers refer to the Υ' sample used in our analysis to select the $\gamma\gamma l^+l^-$ events

[2] Quoted trigger efficiencies refer to the events which might be reconstracted by our complete selection procedure. They were derived with the Monte Carlo studies.

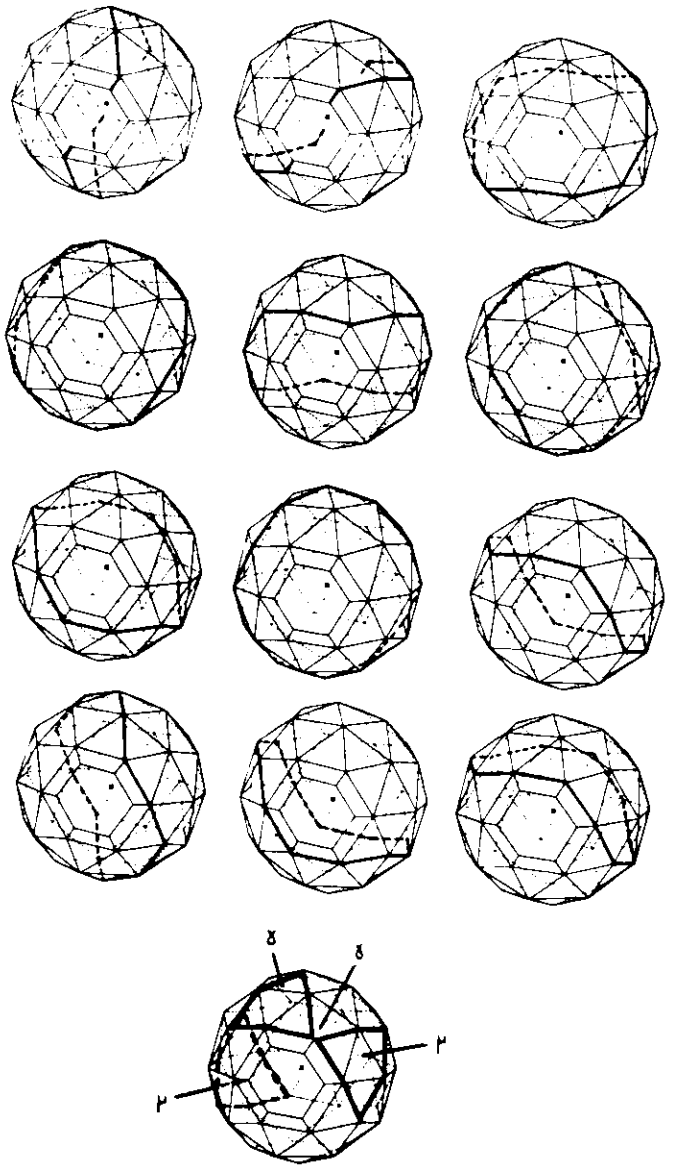

Figure 9.
The Topological trigger.
Each hemisphere indicated in the first 12 pictures, except for the two smaller ones from the last two asymmetrical divisions of the ball, must have at least one major triangle with energy above 160 MeV to satisfy this trigger.
The last picture shows one of the detected $\gamma\gamma\mu^+\mu^-$ events. Three major triangles with energy above the threshold are indicated. It is easy to check that the topological trigger was satisfied.

almost back-to-back minor triangles with energy above 95 MeV were required to satisfy this trigger (Fig.10). Because of the original design to trigger on the $e^+e^- \to \mu^+\mu^-$ events, a total energy threshold of only ~300 MeV was required in the main ball. To suppress the beam-gas events, which relatively easily satisfied the conditions described above, a veto on energy close to the beam pipe was imposed. Energy in the tunnel region could not exceed ~30 MeV on the either side. This caused 12 % inefficiency of the μ-pair trigger alone for the $\gamma\gamma\mu^+\mu^-$ events, due to a particle in the veto region.

Full detector information was stored in an intermediate PDP buffer for all triggered events. The data, without any on-line preselection, were transmitted by the on-line link to a large disk at the central IBM computer at DESY. After sufficient number of events had been accumulated, the data were dumped to the 6250 Bpi tapes. In total, ~28 million events were recorded during the Υ' on-resonance running. A typical event record length was around 1 Kbyte. The data were stored on 449 magnetic tapes.

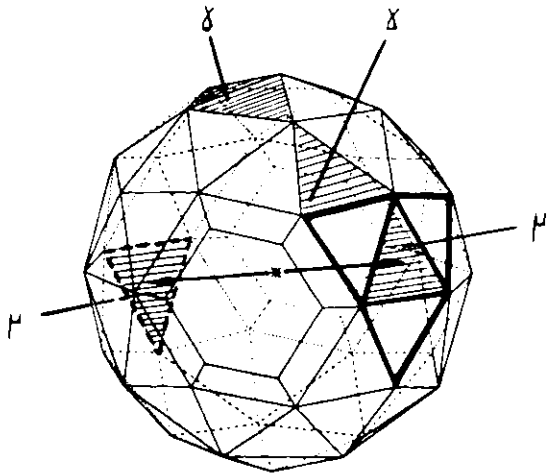

Figure 10.
The μ-pair trigger.
One of the four indicated minor triangles which are approximately back-to-back to the minor triangle shown by the dashed lines should have energy above 95 MeV to satisfy this trigger. This was the case for the displayed $\gamma\gamma\mu^+\mu^-$ event. The minor triangles with energy above the threshold are shaded.

III.2. Initial Off-line Data Processing

Once the data were available for off-line processing, they were used to calibrate the apparatus. For example, large angle Bhabha scattering events, $e^+e^- \to e^+e^-$, were used for the tracking chamber calibration and for the energy and time calibration of the ball.

Raw detector information was translated into physically meaningful quantities, like the crystal energies and the space coordinates of the tube chamber hits, by the production program[1]. Some obvious cosmic ray and beam-gas events were removed at this stage of the data processing. The production preselection did not cause any loss in efficiency for the $\gamma\gamma l^+l^-$ events.

The surviving 17 million events (60 % of all triggers) were written onto 425 magnetic tapes in an extended off-line data format.

III.3. Interpretation of Crystal Energies

The Crystal Ball is a nonmagnetic detector. Its power lies in good energy calorimetry. Our analysis of the $\gamma\gamma\mu^+\mu^-$ and $\gamma\gamma e^+e^-$ events makes no use of any part of the detector other than the NaI crystals[2]. Therefore, we will concentrate on the off-line particle reconstruction from the energy deposition in the Crystal Ball calorimeter alone. Some of our auxiliary analyses make use of the tube chambers and the ToF system. Necessary information about corresponding software will be provided in Appendices C, F, G.

Particles going through the NaI crystals lose energy triggering the scintillation process. The light output from the crystals is converted into electric pulse and then amplified by photo-multipliers mounted on the end of each NaI module. The crystal pulses are further amplified by electronic circuits and digitized. The detection system is specially designed to provide a linear relationship between the energy deposition in the NaI crystal and the corresponding ADC output. The slope of this linear dependence is determined, for each crystal, by the off-line calibration with use of Bhabha scattering events, $e^+e^- \to e^+e^-$.

[1] We mean here the standard Crystal Ball production program.

[2] Because of the beam related background problems at DORIS-II, the performance of the tracking chambers was often unreliable and time dependent during the period of the Υ' running. This would be difficult to simulate, especially in the analysis of the angular distribution. Using the tracking chambers we would also loose some detection efficiency of photons, due to the photon conversion in the tube chambers and overtagging caused by random hits.

Because of the fine detector granularity, electromagnetically showering particles, hadronically interacting particles and even minimum ionizing particles may leave their energy in several crystals. A search for energy clusters is the first step on the way to a reconstructed event. A cluster of crystals, all with an energy greater than 10 MeV, which touch one another on the side or at a vertex is called a "connected region" (Fig.11).

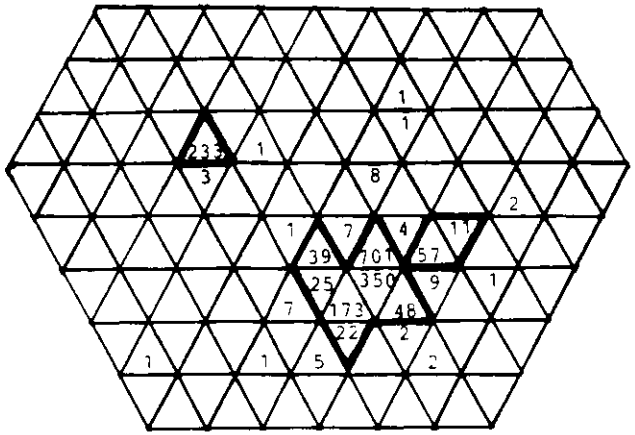

Figure 11.
Two examples of connected regions. The numbers denote energy in the crystals in MeV.

It may happen that more than one particle contributes energy to the same connected region. We check for overlapping energy clusters by looking for local energy maxima. Crystals which are accepted as "good" local energy maxima are called bump modules (or simply bumps). The author has developed a bump algorithm, which differs from the standard Crystal Ball bump search procedure described, for example, in Ref.20. We looked for crystals which had no neighbour in the next two layers of the crystals ("the group of 13"- see Fig.12), with energy greater than the bump candidate itself. A detailed description of our algorithm is given in Appendix A.

Because of the different geometry and the radiation length, the endcap crystals were excluded in this analysis from the bump search. The endcaps were used only as veto counters to remove events with particles missing the main detector.

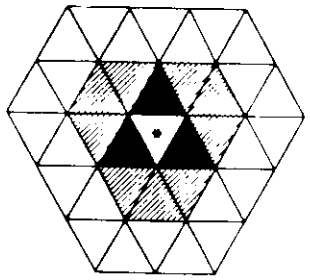

Figure 12.
The group of 13 (shaded and black) crystals and the group of 4 (black) crystals with the bump module (indicated by the star) at the central position.

Photons and electrons leave almost all their energy in the group of 13 crystals, with the bump module in the central position (Fig.12). Therefore, this group of 13 crystals is used to measure energy of the electromagnetically showering particles. We applied the standard Crystal Ball energy algorithm described in Appendix B.

Contrary to the electrons and photons, the other particles do not initiate shower development in the NaI crystals. They leave usually only a small fraction of their total energy by the ionization process. Their momenta remain unknown, and their energy depositions are used only in attempts to identify them and to measure their directions.

We used the center of the bump module as an estimate of the direction of nonshowering particles. Resolution of this method is about 0.060 rad. Directions of the showering particles can be reconstructed much better. One may calculate the energy weighted average of the crystal directions in the group of 13. However, this kind of estimate is biased towards the center of the bump module. The algorithm applied in our analysis[1] removes this bias by a correction, developed with Monte Carlo generated photons. The obtained resolution improves with the photon energy from ~0.035 rad at 100 MeV up to ~0.013 rad for photon energies above 1500 MeV. As the exact position of the interaction vertex is not known (see section II.1), the resolution in the polar angle to the beam axis is degradated by ~0.033 rad.

[1] The algorithm is called SHOWER. It was developed by T. Burnett.

III.4. Event Selection

As the rate of the cascade reaction :

$$e^+e^- \rightarrow \Upsilon' \rightarrow \gamma\chi_b \rightarrow \gamma\gamma\Upsilon \rightarrow \gamma\gamma l^+l^-$$

was rather small, and the background was fairly large, a careful and well tuned event selection was a non-trivial part of the analysis presented here.

The event topology we looked for was strongly constrained by the small mass difference between the Υ' and Υ resonances compared to their masses. After two photons are emitted by the radiative decays of the Υ' and χ_b resonances, the Υ resonance is produced almost at rest. Therefore, two leptons from the Υ decay, carrying approximately half of the Υ mass, must be almost collinear. A maximal acollinearity angle of 6 degrees is allowed kinematically. The lepton acollinearity observed from the center of the ball may be somewhat greater due to the position uncertainty of the interaction point.

A pair of back-to-back high energy leptons, in addition to two photons, is the main signature of the cascade events. Unfortunately, particle identification in the Crystal Ball is very limited. Some particle-type identification with the Crystal Ball detector is possible via patterns of energy deposition. However, selection criteria must be adjusted for each particular analysis independently, as a compromise between the detection efficiency and the background suppression.

High energy electrons deposite their entire momenta in the calorimeter, and therefore are relatively easy to identify. A single bump connected region with energy greater than 3750 MeV was an electron candidate in our selection.

For the lack of muon identification by iron filters and of a muon momentum measurement, cuts to select muons had to be more elaborate. Muon energy deposition patterns have been studied in detail with the $e^+e^- \rightarrow \mu^+\mu^-$ events. The description can be found in Appendix C. Fast muons passing through the ball leave only a small fraction of their energy by the minimum ionizing process. The mean energy deposition is a function of the NaI thickness only, and turns out to be around 210 MeV. Our cut $150<E13_\mu<310$ MeV, where $E13_\mu$ denotes energy deposited by the muon in the group of 13 crystals, left out some muons at the high energy side, because of the long Landau tail in the muon energy deposition towards the higher values, as seen in Fig.13. A muon passing the ball radially may leave energy in only

one crystal. Some neighbouring crystals may be, however, also involved, because of deviations from the radial trajectory due to the spread of the interaction point, multiple scattering in the NaI and the radiation of knock-on electrons. It was found that a significant fraction of the energy was deposited by a muon in only two crystals. This kind of lateral energy pattern is rather unlikely for the electromagnetically showering particles or interaction hadrons, thus we applied the cut : E2/E13 > 0.90 (where E2 is a sum of energies in the bump module and the second energetic module in the group of 13) for a muon candidate. The fraction of muons and photons surviving this cut can be read from Fig.14. Charged hadrons (e.g. pions) escaping the ball without interaction (37 % probability) fake muons in our detector.

Unique identification of photons is also difficult to achieve. Electrons could not be distinguished from photons in our analysis, since we did not use the tracking chambers. Some discrimination against the other particles was possible by cuts on the lateral energy distribution, known from the EGS Monte Carlo. In our analysis we avoided stronger cuts to secure high detection efficiency. Only a moderate cut against minimum ionizing particles was applied : E2/E13 < 0.98 (see again Fig.14). The photon candidate had to be, in addition, a single bump connected region with energy above 50 MeV. Lower photon energies were not investigated because of the high background from the hadronic split-off's[1] in this energy region.

With the above particle selection criteria we looked for the $\gamma\gamma e^+e^-$ and $\gamma\gamma\mu^+\mu^-$ events coming from the cascade reaction. All final state particles had to be reconstructed to distinguish the desired events from background processes. In addition to the four connected regions which could be interpreted as two photons and two back-to-back electrons or muons (30° acollinearity cut was applied), not more than two spurious low energy (E<50 MeV) connected regions were allowed. We could not require exactly four energy clusters, since the synchrotron radiation and beam particles lost from the beam orbit very often provided additional energy. To get rid of events with a particle missing the main detector, events with the total energy in the endcaps greater than 80 MeV were rejected.

To prevent energy leakage at the edge of the ball, photons and electrons were not allowed to penetrate the tunnel crystals too much. This was ensured by a cut on the polar angle to the beam axis $|\cos\theta| < 0.866$. Because of the trigger inefficiency, the muon directions were restricted to the $\cos\theta < 0.85$ volume. Events with particles going too close to each other were

[1] Energy depositions, by interaction of the secondary hadrons, splitting off from the main energy cluster.

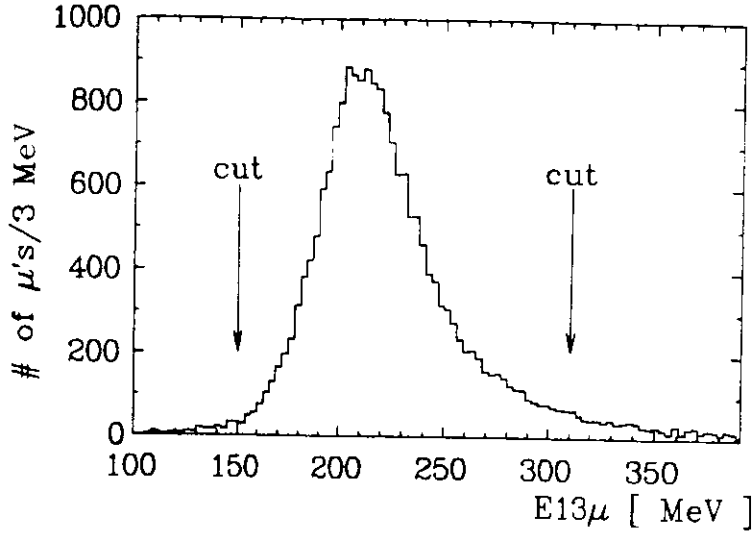

Figure 13.
The energy deposition by muons from $e^+e^- \to \mu^+\mu^-$ events. The cuts used in the selection of $\gamma\gamma\mu^+\mu^-$ events are indicated.

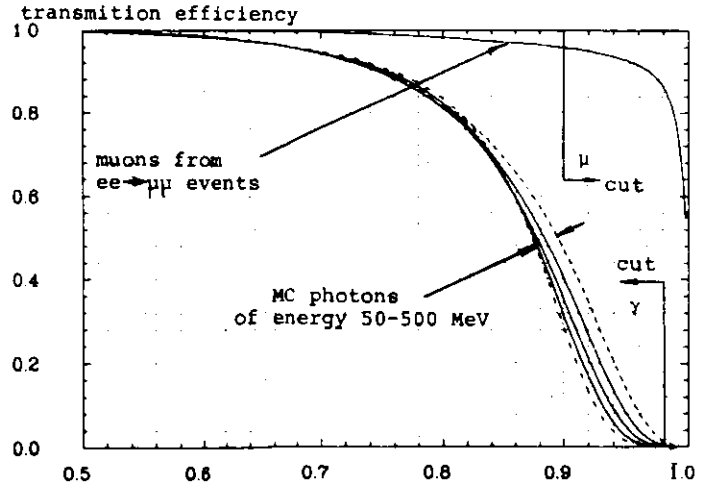

Figure 14.
The energy pattern cuts of muon and photon identifications in the selection of $\gamma\gamma\mu^+\mu^-$ events. The curves show the fraction of muons/photons passing the cut : E2/E13 greater than the value given by the x-axis.
The cut E2/E13> 0.90 is 96 % efficient for muons, removing 30-50 % of electromagnetic showers.
All photons and only 14 % (100 − 86 % as read from the picture) of minimum ionizing particles pass E2/E13< 0.98 cut.

rejected, to secure a good energy measurement of photons. A high energy electron shower in the neighbourhood was the greatest threat to the energy measurement of the photon. A nearby muon was the least dangerous. The following overlap cuts, tuned on the Monte Carlo sample, were applied:

$$\cos\theta_{e\gamma} < 0.82 \qquad \cos\theta_{\gamma\gamma} < 0.86 \qquad \cos\theta_{\mu\gamma} < 0.93 \ .$$

The explicit overlap cuts only slightly lowered the selection efficiency, as overlapping particles often merged into one connected region anyway.

There was some overlap between the photon and the muon definitions, thus double interpretation of the $\gamma\gamma\mu^+\mu^-$ candidate events was allowed. At the end of the selection, however, all events in our sample were unambiguously interpreted. There was no ambiguity in the $\gamma\gamma e^+e^-$ channel, because we asked for exactly two high energy electrons.

To save computer time, events with $E_{\gamma_1} + E_{\gamma_2} < 200$ MeV were rejected, since the cascade signal was expected at $E_{\gamma_1} + E_{\gamma_2} \approx 360$ MeV. The total energy in the ball and endcaps was restricted to the 500-1600 MeV range for the $\gamma\gamma\mu^+\mu^-$ candidates and to the 7700-12000 MeV range in the $\gamma\gamma e^+e^-$ channel. One of the triggers described in section III.1 had to be statisfied.

Using the selection criteria described above, the 17 million events of the production data were reduced to 882 $\gamma\gamma e^+e^-$ candidates and to 3587 $\gamma\gamma\mu^+\mu^-$ candidates. To find a signal from the cascade process, we plot the mass difference between the Υ' and the system recoiling against two photons, versus the energy of the less energetic photon[1] for these events. The quantities should peak for the cascade events at values :

$$\begin{aligned} M_{\Upsilon'} - M^{\text{recoiling}}_{\text{against }\gamma\gamma} &= M_{\Upsilon'} - M_{\Upsilon} = 563.3 \pm 0.4 \text{ MeV}^{[19]} \\ E^{\text{low}}_{\gamma} &= \frac{M^2_{\Upsilon'} - M^2_{\chi_b}}{2 \cdot M_{\Upsilon'}} \approx M_{\Upsilon'} - M_{\chi_b} \ . \end{aligned} \tag{III.4-1}$$

For the $\gamma\gamma e^+e^-$ sample the event clustering at the expected value of $M_{\Upsilon'} - M_{\Upsilon}$ and photon energies 100-140 MeV is apparent (Fig.15). The same clustering is observed for the $\gamma\gamma\mu^+\mu^-$ events, however, the background contamination is much higher (Fig.16). There is no reason to expect more background for the genuine $\gamma\gamma\mu^+\mu^-$ events, than for the $\gamma\gamma e^+e^-$ events, thus the excess of the $\gamma\gamma\mu^+\mu^-$ candidates is clearly due to the problem of a muon identification.

[1] See also section IV.1 for a discussion of these quantities.

Figure 20.
The final sample of $\gamma\gamma\mu^+\mu^-$ events (63 pb^{-1} on T').

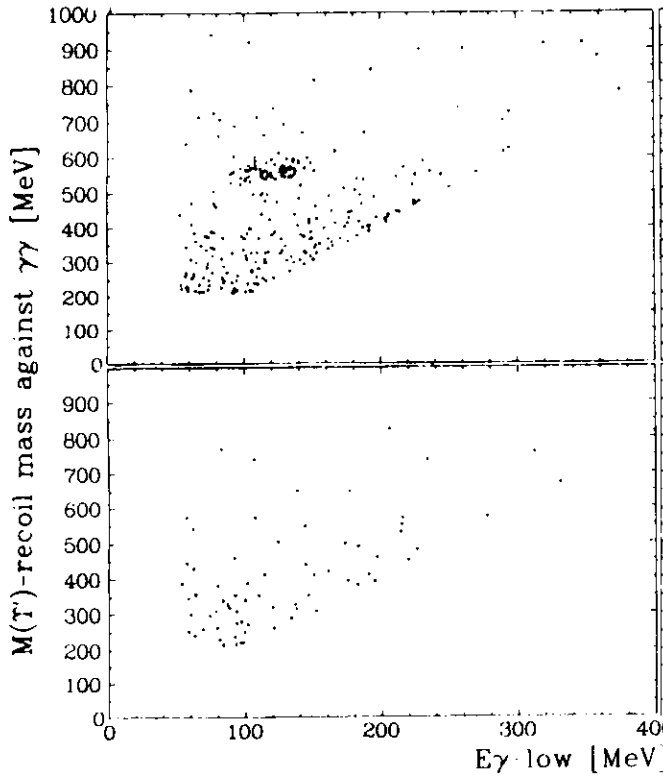

Figure 19.
The final sample of $\gamma\gamma e^+e^-$ events (63 pb^{-1} on T').

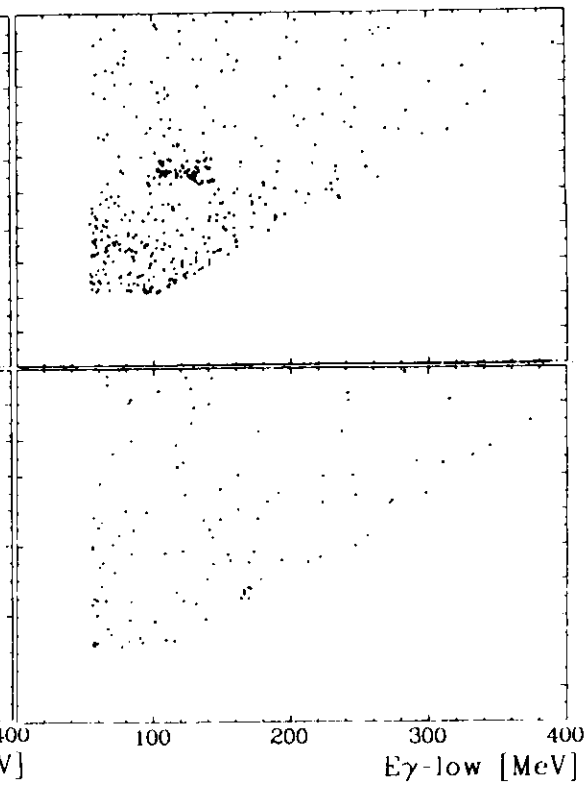

Figure 22.
The $\gamma\gamma\mu^+\mu^-$ events off the T' (26 pb^{-1}).

Figure 21.
The $\gamma\gamma e^+e^-$ events off the T' (26 pb^{-1}).

Figure 16.
The $\gamma\gamma\mu^+\mu^-$ events after preselection.

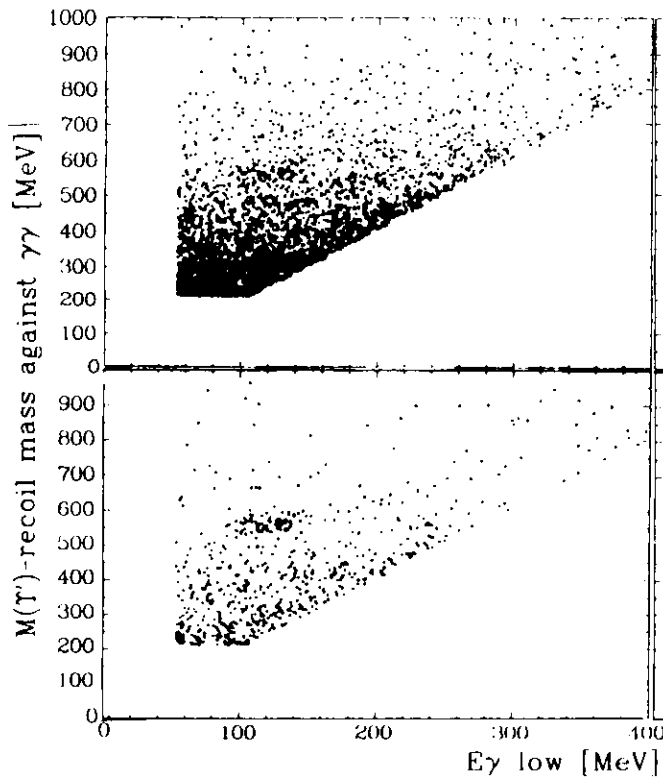

Figure 15.
The $\gamma\gamma e^+e^-$ events after preselection.

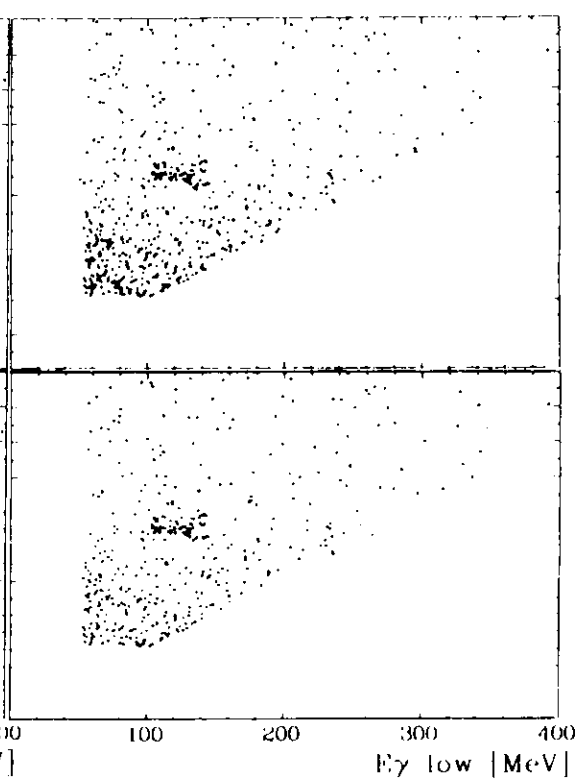

Figure 18.
The $\gamma\gamma\mu^+\mu^-$ events after further cuts.

Figure 17.
The $\gamma\gamma e^+e^-$ events after further cuts.

An efficient cut to suppress this background was found. Instead of identifying photons and muons locally, by energy patterns inside the groups of 13 crystals around the bumps, one may check a global energy spread outside these regions ("excess energy"). Misidentified hadrons tend to deposite some energy outside the group of 13 crystals via interaction of the secondary particles. An energy deposition outside the group of 13 crystals is very unlikely for muons and small for relatively soft photons (2.25 % of E_γ). The shower leakage of electromagnetic showers outside the groups of 13 crystals was subtracted in an average way. The main source of the excess energy for the real $\gamma\gamma\mu^+\mu^-$ events was accidentally superimposed low energy beam-related background. As this kind of background peaks at small angles to the beam axis, the endcap and tunnel region crystals were excluded from the excess energy sum (E_{excess}).

The distribution of the excess energy for our $\gamma\gamma\mu^+\mu^-$ candidates is compared to the distribution for the $\gamma\gamma\mu^+\mu^-$ Monte Carlo events in Fig.23.24. The real events coming from a special trigger, firing every 10^7 beam crossing, were merged with the clean Monte Carlo events. This ensured the proper simulation of the excess energy. Distributions in Fig.23.24 show that, in fact, our $\gamma\gamma\mu^+\mu^-$ candidates have little similarity to good $\gamma\gamma\mu^+\mu^-$ events. Events with $E_{excess} > 40$ MeV were rejected. Some additional cuts were applied for events with $15 < E_{excess} < 40$ MeV to suppress steeply rising background in this region :

endcap energy < 40 MeV,

excess energy in the tunnel region < 15 MeV,

$\frac{E2}{E4} > 0.99$ for muons.

These cuts reduced number of the $\gamma\gamma\mu^+\mu^-$ candidates to 665 events, clearly enhancing the cascade signal (Fig.18).

The excess energy algorithm did not help in the $\gamma\gamma e^+e^-$ channel, since even small fluctuations in the leakage of an electron shower outside the group of 13 crystals reduced the sensitivity to hadrons misidentified as photons. We applied, instead, an additional cut on the lateral energy distribution for photons in the sample of $\gamma\gamma e^+e^-$ candidates : $0.46 < E1/E4 < 0.96$ reducing the number of events to 695 (Fig.17).

The final background reduction was done by a kinematic fit, checking the four-momentum conservation according to the $\gamma\gamma l^+l^-$ hypothesis. Complete measurement of photon and electron four-momenta led to the four constraint fit (4C) to the $\gamma\gamma e^+e^-$ events. Since only directions were measured for muons, a fit in the $\gamma\gamma\mu^+\mu^-$ channel was less constrained (2C

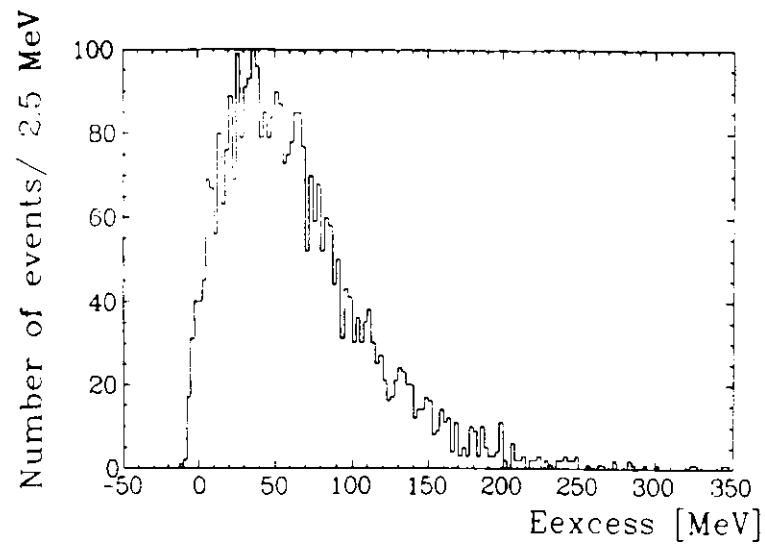

Figure 23.
The excess energy distribution for the preselected data of $\gamma\gamma\mu^+\mu^-$ events.

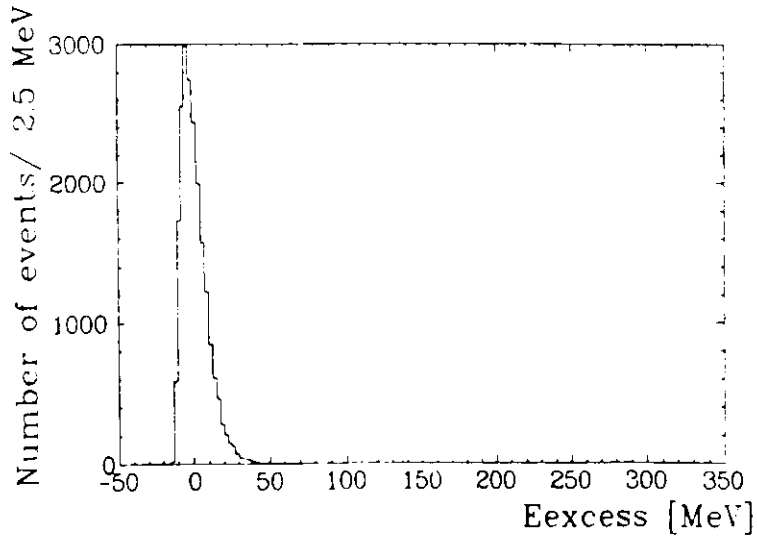

Figure 24.
The excess energy distribution for the genuine $\gamma\gamma\mu^+\mu^-$ events from the Monte Carlo.

fit). Some details of the kinematic fit procedure can be found in Appendix D. Cut on the confidence level of the fit at 1 % left 291 $\gamma\gamma\mu^+\mu^-$ events and 628 $\gamma\gamma e^+e^-$ events. The large event rejection in the muon channel showed that there had still been a lot of $\gamma\gamma\mu^+\mu^-$ candidates with misidentified particles. The cascade signal is very clean in the final $\gamma\gamma\mu^+\mu^-$ sample (Fig.20). The effect of the kinematic fit was marginal on the electron sample. Despite the fit, there remains higher background under the cascade signal for the $\gamma\gamma e^+e^-$ events (Fig.19). This is because of the double radiative Bhabha events $e^+e^- \to e^+e^-\gamma\gamma$. The heavier muon mass relative to the electron mass suppresses final state radition in the similar QED process : $e^+e^- \to \mu^+\mu^-\gamma\gamma$. Thus, double radiative annihilation into a muon pair, with both photons detected at large angles to the beam, is rare, since directions of the bremsstrahlung photons peak along the directions of the radiating beam particles. The higher background in $\gamma\gamma e^+e^-$ channel is reflected by the larger number of selected $\gamma\gamma e^+e$ events, compared to the $\gamma\gamma\mu^+\mu^-$ events.

There is no clustering of events in the cascade region for $\sim$26 pb^{-1} of the data taken off the Υ' resonance (Υ, continuum, Υ'''), as shown in Fig.21,22.

Examples of the selected cascade events are shown in Fig.25 26.

Figure 25. An example of $\gamma\gamma\mu^+\mu^-$ event.

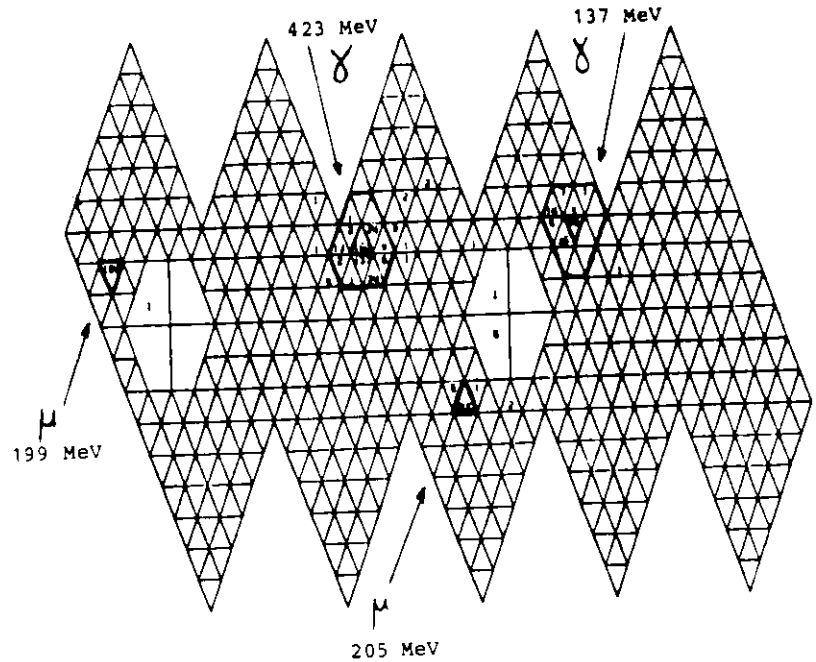

Figure 26. An example of $\gamma\gamma e^+e^-$ event.

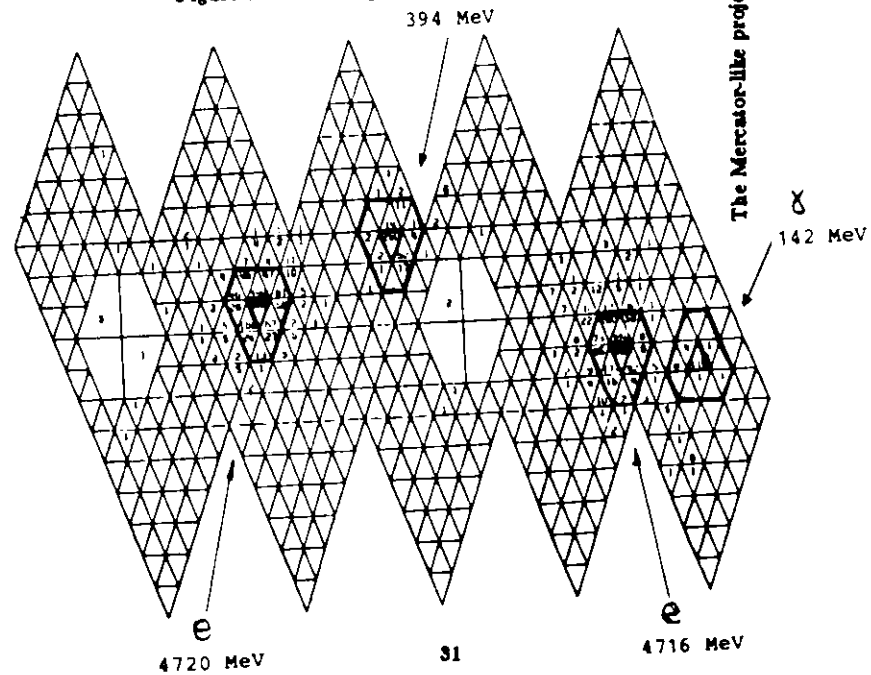

The Mercator-like projection of all modules in the Crystal Ball.

IV. DATA ANALYSIS

IV.1. Cascade Signal

A measurement of the photon energies plays a key role in the interpretation of the signal observed in the $\gamma\gamma\mu^+\mu^-$ and $\gamma\gamma e^+e^-$ events. The lepton pair must be proven to come from the Υ decay, to identify the cascade reaction. Even in the electron channel, the only way to do that is to calculate the invariant mass of the system recoiling against the two photons. The muon energies are not measured at all, and the precision of the $M_{e^+e^-}$ mass, calculated from the electron four-vectors, is not sufficient[1]

$$M^{\text{recoiling}}_{\text{against }\gamma\gamma} = \sqrt{(P^{\nu}_{\Upsilon'} - P^{\nu}_{\gamma\gamma})^2} = \sqrt{M^2_{\Upsilon'} - 2M_{\Upsilon'}(E_{\gamma_1} + E_{\gamma_2}) + 2E_{\gamma_1}E_{\gamma_2}(1 - \cos\theta_{\gamma\gamma})}$$

$$= M_{\Upsilon'}\sqrt{1 - 2\frac{E_{\gamma_1} + E_{\gamma_2}}{M_{\Upsilon'}} + 2\frac{E_{\gamma_1}E_{\gamma_2}}{M_{\Upsilon'}M_{\Upsilon'}}(1 - \cos\theta_{\gamma\gamma})} \qquad \text{(IV.1-1)}$$

As the ratios $\frac{E_{\gamma_1}}{M_{\Upsilon'}} < \frac{0.56\text{ GeV}}{10.0\text{ GeV}} \simeq 0.06$ are small, the last term, dependent on the photon directions, may be neglected. Using the approximation of a square root one obtains :

$$M^{\text{recoiling}}_{\text{against }\gamma\gamma} \approx M_{\Upsilon'}\left(1 - \frac{E_{\gamma_1} + E_{\gamma_2}}{M_{\Upsilon'}}\right)$$

$$M_{\Upsilon'} - M^{\text{recoiling}}_{\text{against }\gamma\gamma} \approx E_{\gamma_1} + E_{\gamma_2} \qquad \text{(IV.1-2)}$$

showing that, in fact, the energy measurement of photons is the most important in our analysis.

The cascade transition via the different spin χ_b states will show up as monoenergetic[2] lines in the photon spectrum from the $\gamma\gamma l^+l^-$ events. To resolve these lines, a high precision measurement of the photon energies is again necessary. Fortunately the Crystal Ball detector meets this requirement.

The energy of the less energetic photon (E^{low}_{γ}) is plotted for the $\gamma\gamma\mu^+\mu^-$ and $\gamma\gamma e^+e^-$ events, against the $M_{\Upsilon'} - M^{\text{recoiling}}_{\text{against }\gamma\gamma}$ in Fig.27. A projection of events, from the band $85 < E^{\text{low}}_{\gamma} < 155$ MeV, onto $M_{\Upsilon'} - M^{\text{recoiling}}_{\text{against }\gamma\gamma}$ axis is shown in Fig.28. The fitted position

[1] Although the relative experimental energy spread is smaller for the high energy electron, than for the low energy photons, the absolute fluctuations are larger $\Delta M_{\Upsilon}^{from\ e^+e^-} \sim 150$ MeV, $\Delta M_{\Upsilon}^{from\ \gamma\gamma} \sim 18$ MeV.

[2] As shown in section VI.3, the natural widths of the χ_b states are smaller than our experimental resolution at least by a factor of 10.

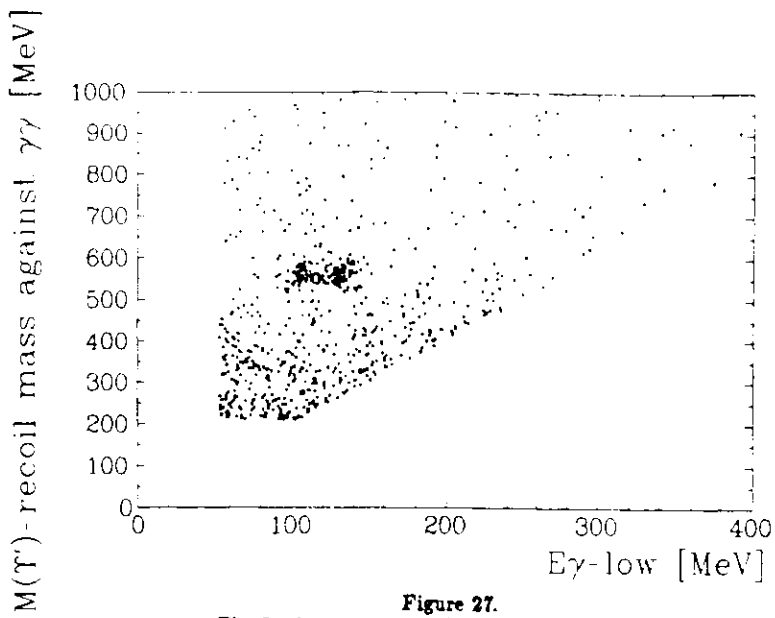

Figure 27.
The final sample of $\gamma\gamma e^+e^-$ and $\gamma\gamma\mu^+\mu^-$ events.

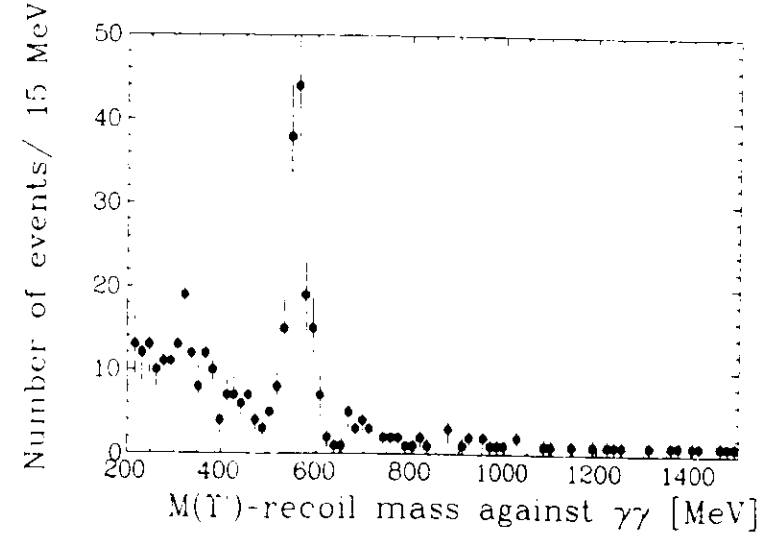

Figure 28.
The distribution of $M_{\Upsilon'} - M^{\text{recoiling}}_{\text{against }\gamma\gamma}$ for events from the $85 \le E^{low}_{\gamma} \le 155$ MeV band. The cascade events peak at the value of $M_{\Upsilon'} - M_{\Upsilon}$.

of the cascade peak : 560.6 ± 3.3 MeV is in reasonable agreement with the world average[19] value : 563.3 ± 0.4 MeV.

To investigate the fine structure of the photon transitions we apply the cut : $518 < M_{\Upsilon'} - M^{recoiling}_{against\ \gamma\gamma} < 609$ MeV and project events onto E_γ^{low} (Fig.29). Two lines, corresponding to two χ_b states, are observed. We will call them temporarily the "α" and "β" lines. To unfold the line positions and amplitudes, a fit to this spectrum was performed. We fitted two monoenergetic photon lines on a flat background. To use most efficiently an information comprised in our sample, the maximum likelihood fit to the unbinned data was applied. The fit is described in detail in Appendix E and displayed in Fig.30. The fit results, also for the muon and electron data independently, are summarized in Table 1.

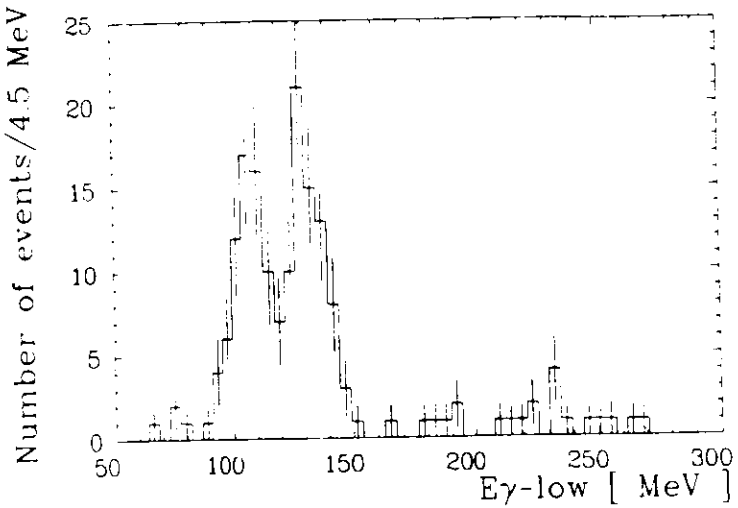

Figure 29.
The energy distribution of less energetic photons for the selected $\gamma\gamma\mu^+\mu^-$ and $\gamma\gamma e^+e^-$ events from the $518 \le M_{\Upsilon'} - M^{recoiling}_{against\ \gamma\gamma} \le 609$ MeV region.

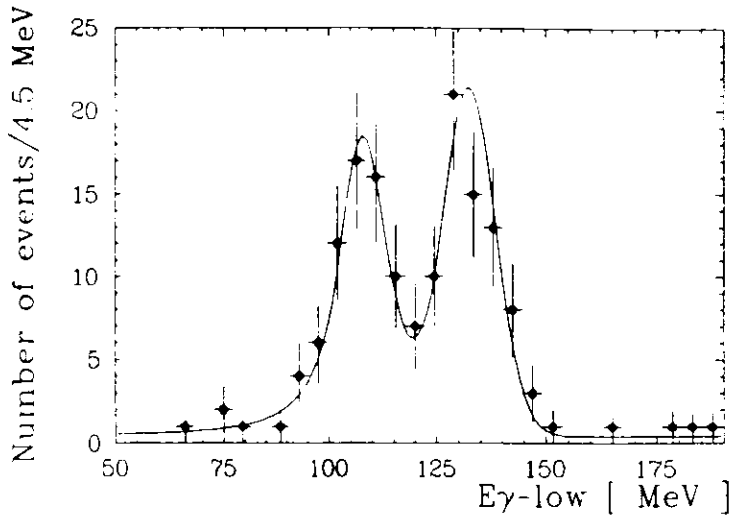

Figure 30.
The fit to the energy spectrum of the lower energy photons from the selected $\gamma\gamma l^+l^-$ events. The fit is described in Appendix E.

Table 1. The results of the fit to the E_γ^{low} spectrum.
E – line energy, A – line amplitude (number of the cascade events), B – number of background events in the fit range $50 < E_\gamma^{low} < 190$ MeV.

	$\gamma\gamma l^+l^-$	$\gamma\gamma\mu^+\mu^-$	$\gamma\gamma e^+e^-$
E_α	107.7 ± 1.1 MeV	109.1 ± 1.9 MeV	107.0 ± 1.4 MeV
E_β	132.4 ± 0.9 MeV	132.9 ± 1.5 MeV	132.2 ± 1.2 MeV
A_α	$56.4^{+8.7}_{-8.9}$	$29.7^{+6.4}_{-6.6}$	$27.9^{+6.0}_{-6.2}$
A_β	$82.1^{+10.1}_{-10.3}$	$37.0^{+6.9}_{-7.1}$	$44.2^{+7.2}_{-7.4}$
B	$13.5^{+5.5}_{-5.9}$	$6.3^{+3.8}_{-4.5}$	$6.9^{+3.9}_{-4.4}$
C.L.	28 %	17 %	48 %

IV.2. Energies of χ_b Lines

The fitted photon energies of the $\Upsilon' \to \gamma\chi_b$ transitions, observed in our cascade sample, are given in the Table 1. The results from the $\gamma\gamma\mu^+\mu^-$ and $\gamma\gamma e^+e^-$ channels are compatible within the statistical errors.

The results carry some systematic uncertainties. The energy calibration was accurate within ± 0.5 MeV in the range of the χ_b lines. The measured energies of the photon lines may be slightly dependent on the data selection. Energy pattern cuts on the photon candidates may pick up some specific types of the shower fluctuations biasing the mean shower energy. Overlap cuts affect the energy leaking into the photon shower from the nearby particles, thus influencing the photon energy measurement. To estimate this kind of systematics, the selection criteria were varied. Statistical fluctuations, due to changes of the event sample, were subtracted from the observed spread of the line energies leaving 0.5 MeV as the systematic error connected to the cuts applied on the data. The uncertainties in the fitting procedure (see Appendix E) turned out to be small (< 0.04 MeV). The contributions to the total systematic errors of the line energies were added linearly (the second error quoted) :

$$E_\alpha = (107.7 \pm 1.1 \pm 1.0) \quad \text{MeV}$$

$$E_\beta = (132.4 \pm 0.9 \pm 1.0) \quad \text{MeV}$$

The results are consistent with the similar study of the cascade transitions done by the CUSB collaboration[16]: $E_\alpha = (107.0^{+2.5}_{-2.0} \pm 2.0)$ MeV, $E_\beta = (128.0 \pm 1.5 \pm 2.0)$ MeV. The positions of the lines coincide with the two less energetic of the three lines observed in the inclusive photon spectrum from the Υ' decays by this experiment[31] (see Fig.31) : $E_\alpha = (110.4 \pm 0.8 \pm 2.2)$ MeV, $E_\beta = (130.6 \pm 0.8 \pm 2.4)$ MeV; and by other detectors [15,17,18]. The comparison of all available results on the energies of the photon transitions $\Upsilon' \to \gamma\chi_b$ are summarized in Table 2. Only results from the magnetic detectors are more accurate than our determination of the photon energies. The third line expected at about 164 MeV is not observed in the cascade channel, which indicates a suppression of the $\chi_b \to \gamma\Upsilon$ transition for the corresponding χ_b state. We discuss this problem in more detail in section VI.3.

According to the quarkonium potential models (see section VI.2), the χ_b^α state should have spin 2, the χ_b^β state spin 1, and the χ_b^γ state (not seen here) spin 0. An experimental justification of this spin assignment, based on the analysis of the angular distribution in our data sample, will be given in section V.2.

Using the formula $M_{\chi_b} = \sqrt{M^2_{\Upsilon'} - 2M_{\Upsilon'}E_\gamma}$, and the world average value of the Υ' mass [19] : (10023.4 ± 0.3) MeV, we can translate our photon line energies into the following χ_b masses :

$$M_{\chi_b}(1^3P_{2^{++}}) = (9915.1 \pm 1.5) \quad \text{MeV}$$

$$M_{\chi_b}(1^3P_{1^{++}}) = (9890.1 \pm 1.4) \quad \text{MeV}$$

Table 2. The comparison of the results on the photon energies from the Υ' radiative decays. Statistical and systematic errors have been added in quadrature. All results are in MeV.

type of analysis	experiment	$1^3P_{2^{++}}$	$1^3P_{1^{++}}$	$1^3P_{0^{++}}$
exclusive cascade events	this analysis	107.7 ± 1.5	132.4 ± 1.3	—
	CUSB [16]	107.0 ± 3.0	128.0 ± 2.5	—
inclusive photon spectrum	this experiment [31]	110.4 ± 2.3	130.6 ± 2.5	163.8 ± 3.1
	CUSB [15]	108.2 ± 2.0	128.1 ± 3.0	149.4 ± 5.0
inclusive photons detected by e^+e^-	ARGUS [18]	110.6 ± 1.0	131.7 ± 1.1	162.1 ± 1.5
	CLEO [17]	109.6 ± 0.7	128.6 ± 1.0	(165.1 ± 2.8)*
WEIGHTED AVERAGE		109.2 ± 0.5	130.4 ± 0.6	161.5 ± 1.3

*The third photon line is not clearly implied by the data, thus it is not included in the calculation of the average.

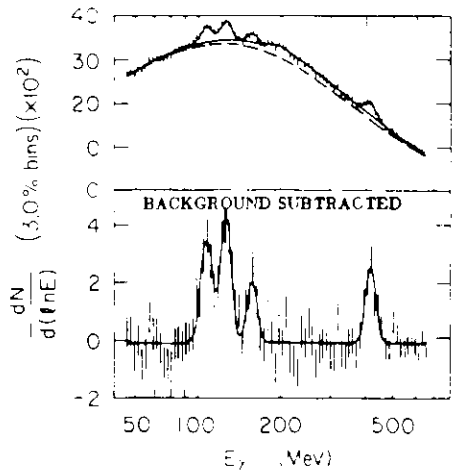

Figure 31.
The inclusive photon spectrum from the Υ' hadronic decays obtained by the Crystal Ball Collaboration (from Ref.31). The curves represent the result of the fit, as described in Ref.31. Three lines in the energy region of 100-170 MeV come from the $\Upsilon' \to \gamma\chi_b$ transitions. The line at 430 MeV is due to the $\chi_b \to \gamma\Upsilon$ transitions.

IV.3. Natural Widths of χ_b Lines

The widths of the both lines observed in the E_γ^{low} distribution (Fig.29) are consistent with the Crystal Ball energy resolution, and one can only determine upper limits for the natural widths (Γ) of these lines.

Appendix E describes the method used to obtain these upper limits. The results are :

$$\Gamma_{^3P_2} < 6.2 \text{ MeV } (90\ \%\ C.L.),$$

$$\Gamma_{^3P_1} < 6.9 \text{ MeV } (90\ \%\ C.L.)$$

Actually, the branching ratios of the cascade process indicate that the χ_b widths are smaller, at least by factor of 10, than the above values. This will be discussed in section VI.3.

More stringent limits of $\Gamma_{^3P_2} < 1.0$ MeV (90 % $C.L.$), and $\Gamma_{^3P_1} < 2.6$ MeV (90 % $C.L.$) were set by the ARGUS experiment[18], in which photon energies were determined by momentum measurement of electrons from the pair conversion in the beam pipe. This method gives very good energy resolution, but very low detection efficiency, preventing studies of the exclusive channels.

IV.4. Detection Efficiency

To obtain the branching ratios for the cascade process from the observed number of events, the detection efficiency must be known. It was studied with the Monte Carlo method.

A large sample of ~50000 $\gamma\gamma\mu^+\mu^-$ and ~20000 $\gamma\gamma e^+e^-$ events was generated, with isotropic decays of all intermediate resonances in the cascade process : $\Upsilon' \rightarrow \gamma\chi_b$, $\chi_b \rightarrow \gamma\Upsilon$ and $\Upsilon \rightarrow l^+l^-$.

The detector response for electrons and photons was simulated by the standard Crystal Ball program, based on the Electron-Gamma Simulation code[33] (hereafter called EGS). The energy resolution came out better than the observed one, since, for example, intercalibration drifts of electronics could not be simulated. Energies of the EGS generated electromagnetic showers were smeared in a gaussian manner to compensate this discrepancy. The asymmetric NaI line shape and the lateral energy distribution of the shower were approximately reproduced by the Monte Carlo program.

Energy depositions by muons were implanted in the Monte Carlo events from $e^+e^- \rightarrow \mu^+\mu^-$ events (see Appendix C).

To simulate the DORIS-II machine background superimposed on the e^+e^- annihilation events, the events collected with a special trigger firing every 10^7 beam crossing were added to the clean Monte Carlo events. The sample of these special "no-interaction" events was representative of the whole Υ' run.

The triggers described in section III.1 were simulated taking into account the hardware inefficiencies during the Υ' running[1].

The Monte Carlo events were analyzed by the same selection programs as the real data.

Efficiencies for the particular angular distribution model were obtained by the methods of weights :

$$\epsilon = \frac{\sum_{j=1}^{N_{acc}} W(\Omega_j|model)}{\sum_{i=1}^{N_{gen}} W(\Omega_i,model)} \qquad \text{(IV.4-1)}$$

where :

ϵ – *selection efficiency,*

Ω – *angular configuration of a MC event,*

$W(\Omega_i,model)$ – *angular correlation function, according to the specific "model", calculated for the angular configuration* Ω,

N_{gen} – *number of all generated MC events,*

N_{acc} – *number of MC events, which passed through the complete selection chain.*

Theoretical formulae for the angular correlation functions are discussed in section V.1. They depend on the χ_b spin, the multipoles of the photon transitions and the beam polarization. The transverse beam polarization was measured to be (75 ± 5) % with $e^+e^- \rightarrow \mu^+\mu^-$ events as presented in Appendix G. All transitions were assumed to be pure electric dipole (E1). The obtained selection efficiencies are not sensitive to small changes of the beam polarization value or to the multipole model. Efficiency calculations were done for spin 0, 1 and 2 for the χ_b state.

To estimate the sensitivity of the results to details of the detector response simulation, another completely independent simulation was done. The second simulation was intentionally crude. The electromagnetic showers in the Monte Carlo events were taken from Bhabha events. All crystal energies in the Bhabha electron shower were scaled to the energy of the photon or electron in the Monte Carlo cascade event. The electron and photon energies were smeared with the NaI energy response function (formula E-1). The energy patterns of low

[1] The trigger simulation program was written by David Gelphman and Wim Walk.

energy photons were only roughly reproduced in this way, as the shower fluctuations depend on the photon energy. The directions of electrons and photons were reproduced only with accuracy to the bump module direction. The muons were simulated this time by a special version of the EGS program supporting knock-on electrons.

The final efficiencies were calculated with the first Monte Carlo method. The auxiliary Monte Carlo was used to calculate the systematic error of the simulation. The final errors on efficiencies include this sytematic contribution and the Monte Carlo statistical error as well :

$$\Delta\epsilon = \sqrt{\Delta^2_{stat.}\epsilon + (\epsilon - \epsilon_{aux})^2} \qquad \text{(IV.4-2)}$$

where :

ϵ – *efficiency from the ezact MC,*

ϵ_{aux} – *efficiency from the auziliary MC.*

The results are listed in Table 3. One sees that our detection efficiencies are weakly dependent on the angular distribution. They are considerably better than in the CUSB [16] experiment[1], $\epsilon_{\gamma\gamma\mu^+\mu^-} = 0.084$, $\epsilon_{\gamma\gamma e^+e^-} = 0.147$.

The pure geometrical acceptance after the cosθ and the overlap cuts (section III.4) is $\epsilon_{\gamma\gamma\mu^+\mu^-} = 0.426 \pm 0.002$ and $\epsilon_{\gamma\gamma e^+e^-} = 0.357 \pm 0.002$ for the isotropic angular distribution. From Table.3 one sees that all other cuts added 19 % and 8 % inefficiencies respectively, as a price for the background suppression.

Table 3. The detection efficiencies.

angular distribution	$\gamma\gamma\mu^+\mu^-$	$\gamma\gamma e^+e^-$
uniform	0.345 ± 0.017	0.328 ± 0.014
J=2	0.320 ± 0.016	0.302 ± 0.013
J=1	0.347 ± 0.018	0.340 ± 0.017
J=0	0.316 ± 0.013	0.286 ± 0.010

[1] The angular correlation model is not specified in Ref.16. It most likely corresponds to the uniform angular distribution.

IV.5. Branching Ratios

The branching ratios for the cascade process may be calculated from the formula :

$$\mathrm{BR}(\Upsilon' \to \gamma\chi^J_b \to \gamma\gamma\Upsilon \to \gamma\gamma l^+l^-) = \frac{A^J_{\gamma\gamma l^+l^-}}{N_{\Upsilon'} \cdot \epsilon^J_{\gamma\gamma l^+l^-}} \qquad \text{(IV.5-1)}$$

where :

$A^J_{\gamma\gamma l^+l^-}$ – *number of observed* $\gamma\gamma l^+l^-$ *events for the* χ^J_b *signal,*

$N_{\Upsilon'}$ – *number of produced* Υ' *decays,*

$\epsilon^J_{\gamma\gamma l^+l^-}$ – *detection efficiency.*

The number of produced Υ' decays can be found by counting the number of detected hadronic events (N^{on}_{had}), correcting for continuum contribution (N^{on}_{cont}) and the hadronic detection efficiency (ϵ_{had}) :

$$N_{\Upsilon'} = \frac{(N^{on}_{had} - N^{on}_{cont})}{\epsilon_{had}} \qquad \text{(IV.5-2)}$$

The continuum subtraction was done by using the data taken in the continuum below the resonance. Number of detected hadronic events for the continuum (N^{off}_{had}) was scaled by the ratio of continuum hadronic cross section *on* and *off* the resonance : $\left(E^{off}_{beam}/E^{on}_{beam}\right)^2$, and the ratio of luminosities : L^{on}/L^{off}. The luminosity was calculated by counting the number of detected large angle Bhabha events : $L \propto N_{Bha} \cdot E^2_{beam}$. Since large angle Bhabha scattering has the same beam energy dependence as the continuum hadronic production ($\sim 1/E^2_{beam}$), the final scaling factor for the continuum subtraction can be expressed simply by the ratio of the detected Bhabha events *on* and *off* the resonance :

$$N^{on}_{cont} = N^{off}_{had} \cdot \frac{N^{on}_{Bha}}{N^{off}_{Bha}} \qquad \text{(IV.5-3)}$$

The Bhabha events were easy to identify by their back-to-back high energy clusters. Hadronic events were selected by removing the beam-gas interaction, cosmic rays, two-photon interaction and $e^+e^- \to e^+e^-, \mu^+\mu^-, \gamma\gamma$ events. The selection efficiency for the Υ' decays, $\epsilon_{had} = 0.86 \pm 0.07$, was found by the Monte Carlo simulation. Description of the hadronic selection and the hadronic efficiency calculation can be found in Ref.34.

From the numbers listed in Table 4 we obtained : $N_{\Upsilon'} = 200\,000 \pm 16\,000$. The error is

entirely dominated by the systematic uncertainty in ϵ_{had}.

Table 4. Hadronic and Bhabha events *on* and *off* the resonance.

Run	CMS energy	Luminosity	N_{had}	N_{Bha}*
Υ'	10.02 GeV	63.0 pb^{-1}	350 110	1 381 257
continuum	9.98 GeV	4.6 pb^{-1}	13 141	101 760

* $\cos\theta < 0.85$

Because of lepton universality, branching ratios measured in the $\gamma\gamma\mu^+\mu^-$ channel and in the $\gamma\gamma e^+e^-$ channel have to be the same. Therefore, we can combine data from both channels to obtain one value of $BR(\Upsilon' \to \gamma\chi_b \to \gamma\gamma\Upsilon \to \gamma\gamma l^+l^-)$, where the type of lepton does not need to be specified[1]. Results averaged over both observed lepton channels were obtained not by taking weighted average of the results in each channel independently, but by fit to the photon spectrum from combined data of both channels. We present also results in the electron and muon channel independently to show consistency of our results.

As discussed in section IV.2, spin 2 is assigned to the χ_b^α state, spin 1 to the χ_b^β state, and spin 0 to the (here unobserved) χ_b^γ state. The numbers of observed cascade events are listed in Table 1, and the detection efficiencies in Table 3. Only an upper limit on the number of observed cascade transitions (A_γ) via spin 0 state could be calculated. The calculation described in Appendix E yielded (90 % C.L.) :

$$A_\gamma(\gamma\gamma l^+l^-) < 4.9 \qquad A_\gamma(\gamma\gamma\mu^+\mu^-) < 4.0 \qquad A_\gamma(\gamma\gamma e^+e^-) < 4.6$$

The results for the branching ratios are given in Table 5.

Table 5. The branching ratios for the cascade process $\Upsilon' \to \gamma\chi_b \to \gamma\gamma\Upsilon \to \gamma\gamma l^+l^-$.

χ_b state	$\gamma\gamma l^+l^-$ *	$\gamma\gamma\mu^+\mu^-$	$\gamma\gamma e^+e^-$
$1^3P_{2^{++}}$	$(4.6 \pm 0.7 \pm 0.5)\cdot 10^{-4}$	$(4.6 \pm 1.0 \pm 0.5)\cdot 10^{-4}$	$(4.6 \pm 1.0 \pm 0.5)\cdot 10^{-4}$
$1^3P_{1^{++}}$	$(6.0 \pm 0.7 \pm 0.7)\cdot 10^{-4}$	$(5.3 \pm 1.0 \pm 0.7)\cdot 10^{-4}$	$(6.5 \pm 1.0 \pm 0.7)\cdot 10^{-4}$
$1^3P_{0^{++}}$	$< 0.4\cdot 10^{-4}$ 90 % C.L.	$< 0.6\cdot 10^{-4}$ 90 % C.L.	$< 0.8\cdot 10^{-4}$ 90 % C.L.

*The fit results to the combined data of $\gamma\gamma\mu^+\mu^-$ and $\gamma\gamma e^+e^-$ events were used.

[1] By notation "l^+l^-" we do not mean, however, that the given branching ratios correspond to a sum over all leptons

Independent results from the electron and muon channels agree very well. The results are also in agreement with the CUSB values[16] as shown in Table 6. The number of observed events was improved in our experiment almost by factor of 3 compared to the CUSB experiment.

Using the world average value[19] of the $BR(\Upsilon \to l^+l^-) = (2.8 \pm 0.3)$ %, we derive from our results :

$$\begin{aligned} &BR(\Upsilon' \to \gamma\chi_b^{J=2})\cdot BR(\chi_b^{J=2} \to \gamma\Upsilon) = (1.6 \pm 0.3 \pm 0.2)\ \% \\ &BR(\Upsilon' \to \gamma\chi_b^{J=1})\cdot BR(\chi_b^{J=1} \to \gamma\Upsilon) = (2.1 \pm 0.3 \pm 0.3)\ \% \\ &BR(\Upsilon' \to \gamma\chi_b^{J=0})\cdot BR(\chi_b^{J=0} \to \gamma\Upsilon) < 0.15\ \% \quad (90\ \%\ \text{C.L.}) \end{aligned} \tag{IV.5-5}$$

These product branching ratios were also measured in our experiment by the inclusive photon study. All three photon lines from the secondary transitions $\chi_b \to \gamma\Upsilon$ were, however, merged into one line, therefore only a sum over all three χ_b states was obtained. The inclusive result[31] $BR(\Upsilon' \to \gamma\chi_b)\cdot BR(\chi_b \to \gamma\Upsilon) = (3.6 \pm 0.7 \pm 0.5)$ % is in very good agreement with the sum of our results for the individual χ_b states : $(3.7 \pm 0.4 \pm 0.4)$ %.

Table 6. Comparison between the Crystal Ball and CUSB results on the cascade branching ratios. Statistical and systematic errors have been added in quadrature.

experiment	$1^3P_{2^{++}}$	$1^3P_{1^{++}}$	$1^3P_{0^{++}}$
this analysis	$(4.6 \pm 0.9)\cdot 10^{-4}$	$(6.0 \pm 1.0)\cdot 10^{-4}$	$< 0.4\cdot 10^{-4}$ (90 % C.L.)
CUSB[16]	$(3.4 \pm 1.4)\cdot 10^{-4}$	$(6.7 \pm 1.7)\cdot 10^{-4}$	$< 1.1\cdot 10^{-4}$ (90 % C.L.)
WEIGHTED AVERAGE	$(4.2 \pm 0.8)\cdot 10^{-4}$	$(6.2 \pm 0.9)\cdot 10^{-4}$	–

Let us mention here, that the CUSB experiment observed also the other radiative cascade transitions in the $b\bar{b}$ family. They reported[14] evidence for the $\Upsilon'' \to \gamma\chi_b' \to \gamma\gamma\Upsilon'$ and $\Upsilon'' \to \gamma\chi_b' \to \gamma\gamma\Upsilon$ cascade decays. The number of events was rather small (~10 events per each reaction), and the χ_b' lines were not resolved.

V. ANALYSIS OF THE ANGULAR DISTRIBUTION

Angular correlations in the cascade channel carry information on the χ_b spins and on the multipole structure of the photon transitions.

According to the quarkonium model, the χ_b states are the lowest radial excitations of the P-wave ($1^3P_{J=+}$) in a system of bound $b\bar{b}$ quarks (see section I.2). This implies spin 0, 1 and 2 for these states. Spin dependent forces of $Q\bar{Q}$ interaction split this triplet into three mass levels. Potential models (see section VI.2), which correctly reproduce the spin structure of the $1^3P_{J=+}$ levels in the $c\bar{c}$ system, all predict that the higher the spin the higher the mass of the χ_b state. Nevertheless, theoretically the reverse ordering could also be possible if, for instance, the scalar confining part of the potential would dominate over the vector Coulomb part[35](see section VI.2). Thus, an experimental verification of the spin assignment is important. It may also justify our spin assumptions made for the branching ratio calculation.

The photon transitions are expected to be pure dipole. We check our data against this assumption, too.

Although we are limited by the poor statistics, a spin analysis of the χ_b states is worth trying. From four experiments on the χ_b states, the Crystal Ball is the only one which can attempt this study. CLEO and ARGUS observed the χ_b states only in the inclusive mode[17,18]. High background under the resonance signals obscures the χ_b spins in the inclusive channel, leaving the cascade reaction as the only tool[1]. The statistics collected by the CUSB experiment in the cascade channel were limited by relatively poor detector acceptance. Moreover, the fine structure of the χ_b states was poorly resolved by the CUSB experiment compared to our case. But even in our case only the lowest spin hypotheses ($J \leq 2$) could be tested, due to the low statistics. Furthermore, we had to assume photon transitions of pure dipole character for the spin tests of $J \neq 0$.

Fig.32 shows the definition of two data samples used in the analysis of the angular correlations. The energy region between the lines was excluded from the analysis, because the line overlap. In the regions indicated on the plot, there are 66 events for the χ_b^α state, and 71 events for the χ_b^β state. The number of $\gamma\gamma\mu^+\mu^-$ and $\gamma\gamma e^+e^-$ events are roughly

[1]Other exclusive modes are unlikely to be observed soon, due to very small branching ratios.

equal. The background contributions can be estimated from the fit, displayed in Fig.32. We find 2.9 ± 1.1 events in each χ_b sample coming from the background processes (mainly from double radiative Bhabha scattering). Because of the asymmetric NaI energy response function (Appendix E), we expect a feed-down from the χ_b resonance to the χ_b^α sample of 7.7 ± 0.9 events. A feed-down from the χ_b^α signal to the χ_b^β sample is negligible. The overall background contribution is 16 % in the χ_b^α sample and 4 % in the χ_b^β sample.

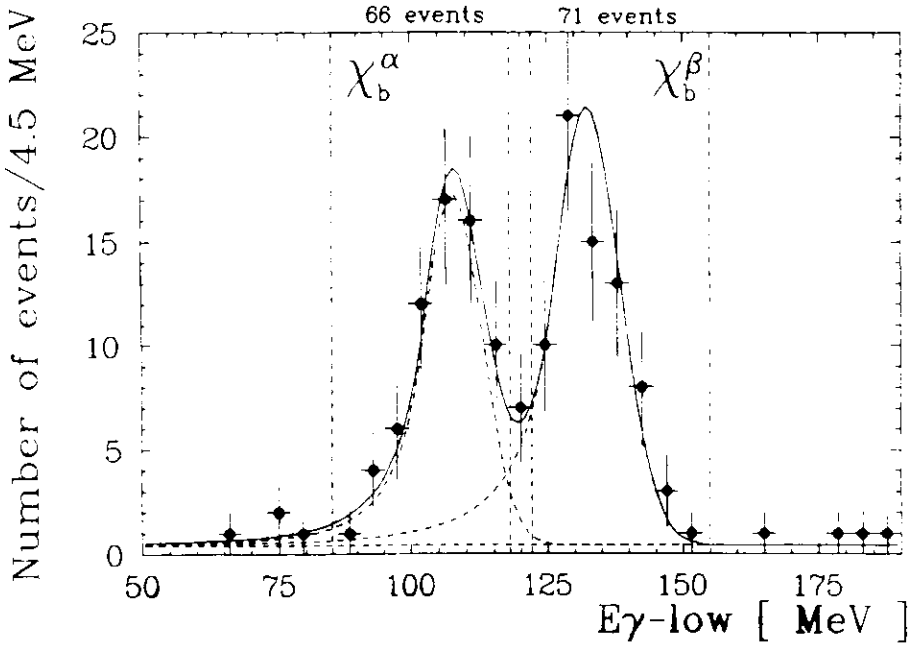

Figure 32.
The definition of the data samples for the analysis of the angular correlations. The fitted contributions from the photon lines and from the background are indicated.

V.1. Angular Correlation Functions

The cascade process :

(V.1-1) $$e^+e^- \to \Upsilon' \xrightarrow{\gamma'} \chi_b \xrightarrow{\gamma} \Upsilon \to l^+l^-$$

has a symmetry around the χ_b state. The χ_b state, with unknown spin, couples by the radiative transitions to well known spin 1 resonances : the Υ' and Υ. The reaction is experimentally determined by detection of the photons and the initial and final state leptons, which couple to the Υ' and Υ by the annihilation steps.

The angular distribution of photons depends on the χ_b spin. It also depends on the multipole structure of the photon transitions and on polarization of the Υ' and Υ. The Υ' polarization is determined by the beam direction and the beam polarization. Angular distribution of the final state leptons is used to analyze the Υ polarization. Therefore, full angular correlations of all observed particles must be studied in order to extract all available information about the χ_b spin.

The beam direction and the direction of the transverse beam polarization define the laboratory reference frame (LAB : $\hat{z} = \hat{e}^+$, $\hat{y} = \hat{P}$). The final state leptons are exactly back-to-back in the Υ rest frame, thus they contribute only one independent direction. Together with directions of the two photons, there are 6 independent angular variables describing a configuration of the cascade event (Ω), since each direction can be described by two angles.

The form of the angular distribution $W(\Omega\, J, \beta', \beta, P)$, corresponding to the spin J of the χ_b state and the multipole structure of the first (β') and the second (β) radiative transitions, is given in Ref.36 and 37. The formulae in Ref.36 assume pure dipole transitions. They are sufficient for our spin analysis (section V.2), but not for study of multipoles (section V.3). Reference 37 deals with the more general case of arbitrary multipoles, but the beam polarization is not included. Here we will recall formalism developed in Ref.37, and we will extend it to the case of polarized beams.

The angular correlation function can be written in a simple form while preserving the symmetry of the cascade process expressed by V.1-1. For this purpose one defines 5 independent angles, in the absence of the beam polarization, in the following way :

θ', φ' – polar and azimuthal angles of the initial state electrons in the rest frame of the Υ', where the γ' direction defines the z-axis, and the x-axis is in γ'-γ plane ($frame-I$: $\hat{z} = \hat{\gamma}'$, $\hat{y} = \hat{\gamma}' \times \hat{\gamma}$, $\hat{x} = (\hat{\gamma}' \times \hat{\gamma}) \times \hat{\gamma}'$ see Fig.33),

$\theta_{\gamma\gamma}$ – angle between the γ' and γ in the rest frame of the χ_b, where the z and x axes are defined like in the $frame-I$ ($frame-II$ see Fig.34)[1],

θ, φ – polar and azimuthal angles of the final state leptons in the rest frame of the Υ, where the γ direction defines the z-axis, and the x-axis is in γ'-γ plane ($frame-III$: $\hat{z} = \hat{\gamma}$, $\hat{y} = \hat{\gamma}' \times \hat{\gamma}$, $\hat{x} = (\hat{\gamma}' \times \hat{\gamma}) \times \hat{\gamma}$ see Fig.35).

We will use helicity amplitudes for the first and the second radiative decay, therefore we define :

υ' – helicity of the Υ'	υ – helicity of the Υ
γ' – helicity of the γ'	γ – helicity of the γ
χ' – helicity of the χ_b	χ – helicity of the χ_b
$A'_{\chi',\gamma'}$ – helicity amplitude for the $\Upsilon' \to \gamma'\chi_b$ transition in $frame-I$	$A_{\chi,\gamma}$ – helicity amplitude for the $\chi_b \to \gamma\Upsilon$ transition in $frame-III$

where:

(V.1-2) $$|\upsilon'|, |\gamma| \le 1 \quad , \quad \gamma'|, |\gamma| = 1 \quad , \quad |\chi'|, |\chi| \le J \quad .$$

The amplitudes for the photon transitions must be real.

Angular momentum conservation implies[2] :

(V.1-3) $$\upsilon' = \gamma' - \chi' \quad , \quad \upsilon = \gamma - \chi$$

Parity invariance requires :

(V.1-4) $$A'_{-\chi',-\gamma'} = (-1)^J P_\chi A'_{\chi',\gamma'} \quad , \quad A_{-\chi,-\gamma} = (-1)^J P_\chi A_{\chi,\gamma}$$

(P_χ – parity of the χ_b) so one defines :

(V.1-5) $$A'_{\chi'} = A'_{\chi',+1} \quad , \quad A_\chi \equiv A_{\chi,+1}$$

[1] The z-axis can be chosen also along the γ direction, with no effect on the $\theta_{\gamma\gamma}$ definition, thus the symmetry of the first and the second transition is not broken in this definition.

[2] We use here the convention from Ref.37 putting minus sign before the χ_b helicities

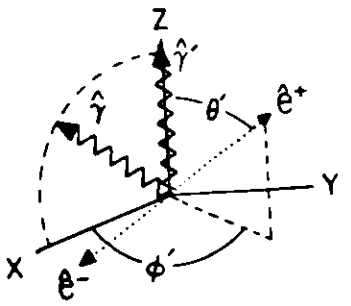

Figure 33.
The rest frame of the Υ' ($frame - I$).

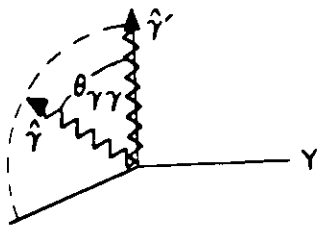

Figure 34.
The rest frame of the χ_b ($frame - II$).

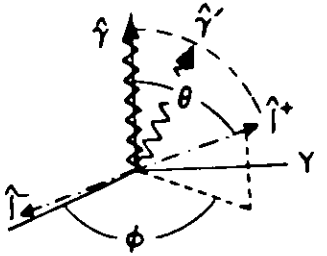

Figure 35.
The rest frame of the Υ ($frame - III$).

where : $0 \le \chi' \le J$, $0 \le \chi \le J$ to satisfy V.1-3.

Summing over unmeasured photon polarizations and the χ_b helicities, one obtains :

(V.1-6)

$$W(\cos\theta', \varphi', \cos\theta_{\gamma\gamma}, \cos\theta, \varphi) \propto$$

$$\sum_{\gamma'\,\tilde{\gamma}'\,\chi'} \varrho_{\Upsilon'}^{(\gamma'-\chi',\tilde{\gamma}'-\tilde{\chi}')}(\theta',\varphi')\, A'_{\chi'}\; A'_{\tilde{\chi}'}\; d^{J}_{-\chi',\chi}(\theta_{\gamma\gamma})\, d^{J}_{-\tilde{\chi}',\tilde{\chi}}(\theta_{\gamma\gamma})\, A_{\chi}\; A_{|\tilde{\chi}|}\, \varrho_{\Upsilon}^{*(\gamma-\chi,\tilde{\gamma}-\tilde{\chi})}(\theta,\varphi)$$

The d-functions can be found for example in Ref.19. The density matrices of the Υ' and Υ can be expressed by the lepton directions :

(V.1-7)
$$\varrho^{(\nu,\tilde{\nu})}(\theta,\phi) = \sum_{ij} \epsilon_i^{*(\nu)}\, \epsilon_j^{(\tilde{\nu})}\, (\delta_{ij} - l_i l_j)$$

where :

$$\textit{polarization vectors} : \epsilon^{(+1)} = \begin{pmatrix} -\frac{1}{\sqrt{2}} \\ -\frac{i}{\sqrt{2}} \\ 0 \end{pmatrix} \quad \epsilon^{(0)} = \begin{pmatrix} 0 \\ 0 \\ 1 \end{pmatrix} \quad \epsilon^{(-1)} = -\epsilon^{*(+1)}$$

$$\textit{the lepton direction} : \hat{l} = \begin{pmatrix} \cos\varphi \sin\theta \\ \sin\varphi \sin\theta \\ \cos\theta \end{pmatrix}$$

Performing summation in V.1-7 one obtains :

(V.1-8)
$$\varrho^{(\nu,\tilde{\nu})}(\theta,\phi) = \begin{pmatrix} \frac{1+\cos^2\theta}{2} & \frac{\sin\theta\cos\theta}{\sqrt{2}} e^{-i\varphi} & \frac{\sin^2\theta}{2} e^{-2i\varphi} \\ \varrho^{*(+1,0)} & \sin^2\theta & -\varrho^{(+1,0)} \\ \varrho^{*(+1,-1)} & -\varrho^{*(+1,0)} & \varrho^{(+1,+1)} \end{pmatrix}$$

To extend V.1-5 to the polarized beam case, we replace V.1-7 by :

(V.1-9)
$$\varrho^{(\nu',\tilde{\nu}')} = \sum_{ij} \epsilon_i^{*(\nu')}\, \epsilon_j^{(\tilde{\nu}')}\, (1 - P^2) \cdot (\delta_{ij} - l_i l_j) + 2\,P^2 \cdot h_i h_j$$

where $\hat{h}$ is the polarization direction and P is the degree of the polarization. In the LAB frame $\hat{h}$ coincides with the y-axis :

(V.1-10)
$$\hat{h}_{\mathrm{LAB}} = \begin{pmatrix} 0 \\ 1 \\ 0 \end{pmatrix}$$

We can obtain $\hat{h}$ in the $frame - I$ by the Euler rotation[1] :

(V.1-11)
$$\hat{h}_I = R_z(\tfrac{\pi}{2} - \varphi')\, R_z(\theta')\, R_z(\psi') \cdot \hat{h}_{\mathrm{LAB}}$$

[1]The strange argument of the third rotation : $\frac{\pi}{2} - \varphi'$ comes from the unfortunate convention adopted here, namely that the second rotation is around x-axis, rather than y-axis.

Of course, the Euler transformation depends on 3 independent angles. Therefore, Eq.V.1-11 introduces the ψ' angle, in addition to the earlier defined φ', θ'. For unpolarized beams the polarization direction $\hat{h}$, and consequently the ψ' angle are not defined. Eq.V.1-11 gives :

$$\hat{h}_l = \begin{pmatrix} \sin\varphi'\sin\psi' + \cos\varphi'\cos\psi'\cos\theta' \\ -\cos\varphi'\sin\psi' + \sin\varphi'\cos\psi'\cos\theta' \\ -\cos\psi'\sin\theta' \end{pmatrix} \tag{V.1-12}$$

The density matrix of the Υ' depends now on 3 angles :

(V.1-13)

$$\varrho^{(\psi',\tilde{\psi}')}(\theta',\phi',\psi') =$$

$$(1-P^2)\cdot\begin{pmatrix} \frac{1+\cos^2\theta'}{2} & \frac{\sin\theta'\cos\theta'}{\sqrt{2}}e^{-i\varphi'} & \frac{\sin^2\theta'}{2}e^{-2i\varphi'} \\ \varrho^{*(+1,0)} & \sin^2\theta' & -\varrho^{(+1,0)} \\ \varrho^{*(+1,-1)} & -\varrho^{*(+1,0)} & \varrho^{(+1,+1)} \end{pmatrix} + 2P^2\cdot$$

$$\begin{pmatrix} \frac{\sin^2\psi'+\cos^2\psi'\cos^2\theta'}{2} & \frac{(\cos\psi'\cos\theta'+i\sin\psi')}{\sqrt{2}}\sin\theta'\cos\psi'e^{-i\varphi'} & \frac{(\sin\psi'-i\cos\psi'\cos\theta')^2}{2}e^{-2i\varphi'} \\ \varrho^{*(+1,0)} & \sin^2\theta'\cos^2\psi' & -\varrho^{(+1,0)} \\ \varrho^{*(+1,-1)} & -\varrho^{*(+1,0)} & \varrho^{(+1,+1)} \end{pmatrix}$$

The helicity amplitudes may be expressed by the multipole amplitudes[1,36] :

$$A_\chi = \sum_{j=1}^{J+1} a_j \sqrt{\frac{2j+1}{2J+1}} \underbrace{< j,-1,1,|\chi-1\ J,\ \chi >}_{\text{Clebsch-Gordan coefficients}} \tag{V.1-14}$$

The multipole coefficients a_j, and similarly a'_j, are not all independent since :

$$\Gamma(\chi_b \to \gamma\Upsilon) \propto \sum_{\chi=0}^{J} A_\chi^2 = \sum_{j=1}^{J-1} a_j^2 \quad , \quad \Gamma(\Upsilon' \to \gamma\chi_b) \propto \sum_{\chi'=0}^{J} A_{\chi'}'^2 = \sum_{j=1}^{J-1} a_j'^2 \tag{V.1-15}$$

The derived formulae do not depend on the quarkonium model, but on spins of the particles involved in the reaction.

The angles used in our formula may be found from the measured particle directions using the relations :

[1] We used the following notation of the Clebsch-Gordan coefficients : $< J_1, m_1, J_2, m_2 | J, m >$.

$$\left.\begin{aligned} \tan(\psi' - \tfrac{\pi}{2}) &= \frac{\hat{\gamma}'\cdot\hat{h}}{\hat{\gamma}'\cdot(\hat{h}\times\hat{e}^+)} \\ \cos\theta' &= \hat{\gamma}'\cdot\hat{e}^+ \\ \tan\varphi' &= \frac{\hat{e}^+\cdot(\hat{\gamma}'\times\hat{\gamma})}{\hat{e}^+\cdot[(\hat{\gamma}'\times\hat{\gamma})\times\hat{\gamma}']} \end{aligned}\right\} \text{in the rest frame of the } \Upsilon'$$

$$\cos\theta_{\gamma\gamma} = \hat{\gamma}'\cdot\hat{\gamma} \qquad \} \text{in the rest frame of the } \chi_b \tag{V.1-16}$$

$$\left.\begin{aligned} \cos\theta &= \hat{\gamma}\cdot\hat{e}^+ \\ \tan\varphi &= \frac{\hat{l}^+\cdot(\hat{\gamma}'\times\hat{\gamma})}{\hat{l}^+\cdot[(\hat{\gamma}'\times\hat{\gamma})\times\hat{\gamma}]} \end{aligned}\right\} \text{in the rest frame of the } \Upsilon$$

In practice, recoil effects on the angular distribution of the cascade events can be neglected (although, we did not do that in our programs). In this case, all quoted reference frames coincide, and boosting of measured directions in the LAB frame to the rest frames of decaying particles is not necessary.

The charges of the outgoing leptons are not identified in our experiment, but the angular correlation function V.1-6 is invariant under the replacement $\hat{l}^+ \to \hat{l}^-$, which is ensured by the conservation of parity in the Υ decay[1].

The formulae given in Ref.36, derived with use of Cartesian tensors rather than spherical tensors, like presented here, were used for debugging our calculations and programs in the case of the pure dipole transitions.

V.2. Spin Analysis

V.2.a. Multipole Assumptions

Although our apparatus was well suited for detection of the cascade events, and our Υ' experiment quite long, the final yield of the cascade events was rather modest, due to the small reaction rate. Under those circumstances, the most general analysis of the angular distribution, which probes the χ_b spin and the multipole structure of both the photon transitions in the same time, cannot give statistically significant results. Therefore, we will accept

[1] This may be seen explicitly, by invariance of V.1-8 under : $\cos\theta \to -\cos\theta$, $\varphi \to \varphi + \pi$.

some theoretical input in our spin analysis, concerning the transition multipoles. Fortunately the assumptions we will make are quite plausible and commonly agreed to.

In accordance with the quarkonium model, we consider only three possible spin values of a χ_b state : 0, 1 or 2. Multipoles of allowed photon transitions are restricted by the χ_b spin itself (see equation V.1-15). The radiative transitions via a spin 0 state must be pure electric[1] dipole (E1). For χ_b states of spin 1 and 2, higher multipoles can contribute : magnetic quadrupole (M2) for spin 1 and up to electric octupole (E3) for spin 2.

Once we accept $Q\bar{Q}$ structure of the Υ family and the single quark transition picture, the octupole transitions are forbidden[37]. In fact, $\Delta L = \pm 1$ in S↔P transitions, and $\Delta S \leq 1$ when only one quark interacts, thus photons carry off at most two units of angular momentum.

The magnetic quadrupole amplitudes are expected to be very small, too. As relativistic effects, the magnetic transitions are suppressed by the heavy b-quark mass. The nonrelativistic quark model predicts[36,39] :

$$\text{(V.2.a-1)} \qquad \frac{\Gamma_{M2}}{\Gamma_{E1}} = \left[\frac{E_\gamma}{4\,m_Q}(1+\kappa)\right]^2 \times \begin{cases} 1 & \text{for } J=1 \\ \frac{9}{5} & \text{for } J=2 \end{cases}$$

where :

E_γ – *photon energy,*

m_Q – *quark mass,*

κ – *anomalous magnetic moment of quark.*

In the worst case of the second transition via spin 2 state, this gives for $\kappa = 0$ and $m_b = 4500$ MeV[9] :

$$\frac{\Gamma_{M2}}{\Gamma_{E1}} \simeq 0.001 \quad .$$

Suppression of M2 transitions in the cascade process was observed by the Crystal Ball experiment[21] already for the charmonium ($m_c \simeq 1500$ MeV). All transition were proved to be pure dipole, except for a possibly non-zero quadrupole amplitude in the radiative decay of the spin 2 χ_c state (see Table 7). Preliminary results of the R704 experiment at the ISR seem to indicate a measureable M2 amplitude in this decay, as well[40]. This may mean large anomalous magnetic moment of the c-quark. Anyway, the heavier b-quark mass would suppress this effect by an order of the magnitude. Therefore we assume that all photon transitions are of pure dipole character.

[1] This assumes positive χ_b parity, like in the quarkonium model. Negative χ_b parity would lead to magnetic dipole transitions. However, our analysis is independent of any χ_b parity assumption, since the angular distribution does not depend on P_χ (see V.1-9).

Table 7. Measured transition multipoles in the cascade $\psi' \to \gamma\chi_c \to \gamma\gamma\psi$ from Ref.21.

Spin of the	Γ_{M2}/Γ_{E1} [%]	
χ_c state	$\psi' \to \gamma\chi_c$	$\chi_c \to \gamma\psi$
J = 1	0.6 ± 0.1	$0.004^{+0.050}_{-0.004}$
J = 2	$1.8^{+3.8}_{-1.5}$	12^{+52}_{-8}

V.2.b. Statistical Methods

The small sample of the cascade events forced us to look for the most efficient statistical methods in our analysis. In particular the goodness-of-fit[1] spin tests on binned data, applied in the analogous studies in the charmonium system[42,21] turned out not to be sensitive enough.

After the transition multipoles have been fixed and the beam polarization has been measured (see Appendix G), the angular distribution in the cascade channel (V.1-9) depends only on the χ_b spin : $W_J(\Omega)$, leading to the single parameter tests. In this case, the most powerful [41] Neyman-Pearson likelihood ratio test can be applied to distinguish between two spin hypotheses : $J_{hyp}=J_1$ and $J_{hyp}=J_2$. The test function takes the form :

$$\text{(V.2.b-1)} \qquad T(\Omega_1,\ldots,\Omega_N) = \frac{1}{N} ln \frac{\prod_{i=1}^{N} W_{J_2}(\Omega_i)}{\prod_{i=1}^{N} W_{J_1}(\Omega_i)} = \frac{1}{N}\sum_{i=1}^{N} ln\left[W_{J_2}(\Omega_i), W_{J_1}(\Omega_i)\right]$$

where :

Ω_i – *6 independent angles in the i^{th} cascade event,*

N – *number of events in the data sample.*

The normalization factor $\frac{1}{N}$ is only used for convenience, as it does not influence test results. When applied to the data Eq.V.2.b-1 gives just a number (T_{data}), which we compare with the probability density distributions of the test function under $J_{hyp}=J_1$ hypothesis : $f(T|J_1)$, and

[2] We use in this chapter a lot of statistical expressions like e.g. "goodness-of-fit", "probability density function", "test function" etc. We do not define all of them here and we refer the reader to e.g. Ref.41.

$J_{hyp}=J_2$ hypothesis : $f(T|J_2)$. The confidence level can be assigned to the tested hypothesis by :

(V.2.b-2) $$C.L.(J_{hyp} = J_1) = \int_{-\infty}^{T_{data}} f(T|J_1)\,dT$$

or

(V.2.b-3) $$C.L.(J_{hyp} = J_1) = \int_{T_{data}}^{+\infty} f(T|J_1)\,dT$$

depending on which side of $f(T|J_1)$ the probability density distribution of the test function under the alternative hypothesis, $f(T|J_2)$, turns out to be. We also investigate another test function of the type :

(V.2.b-4) $$T(\Omega_1,\ldots,\Omega_N) = \frac{1}{N} ln \prod_{i=1}^{N} W_J(\Omega_i) = \frac{1}{N}\sum_{i=1}^{N} ln\, W_J(\Omega_i)$$

which can be useful while testing more than just two spin values.

One should stress here that, event though our test functions are constructed from likelihoods, their probability density functions, $f(T|J)$, are not known a priori (e.g. from a general statistical theorem), since the tested parameter, J, is not continous.

In the expressions for a likelihood, $\prod_{i=1}^{N} W_J(\Omega_i)$, we use the theoretical angular distribution. In principle, one should use theoretical formulae corrected for detector resolution and acceptance effects to get the most powerful tests. However, these corrections could not be obtained in practice, as $W_J(\Omega)$ was six-dimensional. Using theoratical formulae in the likelihoods we still obtain strict results, as the detector effects are taken into account while obtaining distributions of such defined likelihoods (see next section). Sensitivity of the tests cannot be much effected, neither. Angular resolution effects are small for our detector, compared to the smooth variation of the theoretical $W_J(\Omega)$. Acceptance function of our detector, $\epsilon(\Omega)$, does not approximately depend on Ω for all accepted events ($\epsilon(\Omega) \simeq 1$ for all accepted events, $\epsilon(\Omega) \simeq 0$ for all rejected events). Therefore it does not contribute to likelihood functions, which are always calculated for the accepted events. The detector acceptance still effects a normalization of the angular distribution function used in the likelihood, however, in our method a normalization of the likelihood function cancels out[1].

[1]The proper normalization of a likelihood is necessary only for its probabilistic interpretation, which is not used here.

V.2.c. Monte Carlo Simulation

All our test functions take the form :

(V.2.c-1) $$T(\Omega_1,\ldots,\Omega_N) = \frac{1}{N}\sum_{i=1}^{N} t(\Omega_i) \quad .$$

The Central Limit Theorem [41] predicts that the $T(\Omega_1,\ldots,\Omega_N)$ should be distributed normally[1] with :

(V.2.c-2) $$< T(\Omega_1,\ldots,\Omega_N) >= < t(\Omega) >$$
$$\sigma^2(T(\Omega_1,\ldots,\Omega_N)) = \frac{\sigma^2(t(\Omega))}{N} = \frac{< t^2(\Omega) > - < t(\Omega) >^2}{N}$$

independent of the shape of the parent distribution of $t(\Omega)$. Therefore the problem of finding the probability density distribution of the test function, $T(\Omega_1,\ldots,\Omega_N)$, under spin hypothesis J_{hyp} reduces to single event averaging of the $t(\Omega)$ and $t^2(\Omega)$:

(V.2.c-3) $$< t(\Omega) >_{J_{hyp}} = \int d\Omega\, \tilde{W}_{J_{hyp}}(\Omega)\, t(\Omega)$$
$$< t^2(\Omega) >_{J_{hyp}} = \int d\Omega\, \tilde{W}_{J_{hyp}}(\Omega)\, t^2(\Omega)$$

where $\tilde{W}_{J_{hyp}}(\Omega)$ is the theoretical angular correlation function V.1-9 with the detector acceptance and resolution effects folded in.

An analytical form of the $\tilde{W}_{J_{hyp}}(\Omega)$ is not known, but the integrals in V.2.c-3 can be calculated numerically by the Monte Carlo method. The Monte Carlo sample described in section IV.4, was used for that purpose. The Monte Carlo events were generated with uniform distributions of all angles. After the detector response was simulated, the Monte Carlo events were selected by the same programs as used for the real data. Finally the integrals in V.2.c-3 were calculated by the method of weights :

(V.2.c-4) $$< t(\Omega) >_{J_{hyp},\beta',\beta P} = \frac{\sum_{i=1}^{M} W(\Omega_i^0|J_{hyp}\,\beta'\,\beta\,P)\cdot t(\Omega_i)}{\sum_{i=1}^{M} W(\Omega_i^0\,J_{hyp}\,\beta'\,\beta\,P)}$$

where :

[1]This is exactly valid in the limit of $N \to \infty$, however the asymptotic features are approached very rapidly and $N \sim 70$ seems sufficient. Deviations from the Gaussian approximations were studied by the explicit MC simulation of the large number of experiments with N like in the data (see Appendix H). They are included as part of the systematic errors.

M – *number of MC events, which survived all cuts,*

$W(\Omega^0\ J_{hyp}\beta'\beta P)$ – *angular correlation function defined by V.1-9,*

Ω_i^0 – *true angles in the i^{th} MC events, which correspond to the measured ones* Ω_i.

The Monte Carlo sample with uniform angular distributions, allowed varying the spin (J_{hyp}), multipole structure of the photon transitions (β', β) and the beam polarization (P), while using still the same Monte Carlo events. This saved a huge amount of the computer time necessary to simulate the detector response.

For simplicity, we have implicitly assumed that we deal with only one type of events in formulae V.2.c-4. Extention to the real case of the two experimental channels, $\gamma\gamma\mu^+\mu^-$ and $\gamma\gamma e^+e^-$, is straightforward :

$$< T(\Omega_1,\ldots,\Omega_N) > = \frac{N_\mu < t(\Omega) >_\mu - N_e < t(\Omega) >_e}{N_\mu - N_e} \qquad \text{(V.2.c-5)}$$

$$\sigma^2(T(\Omega_1,\ldots,\Omega_N)) = \frac{N_\mu\,\sigma_\mu^2(t(\Omega)) - N_e\,\sigma_e^2(t(\Omega))}{(N_\mu - N_e)^2}$$

Applying Gaussian approximation to the distributions of the test functions, one can express the test results in standard deviations,

$$\mathrm{SD} = \frac{|T_{data} - < T >_{J_{hyp}}|}{\sigma(T)_{J_{hyp}}}. \qquad \text{(V.2.c-6)}$$

V.2.d. Sensitivity of Spin Tests

Being able to find the probability density distribution of the test function under each spin hypothesis, we may check what kind of sensitivity for different spins one can get given the observed number of events.

From V.2.c-3 one can get a general idea about the dependence of a separation between spin hypotheses on the experimental statistics. The normalization factor $\frac{1}{N}$ ensures that mean values of the test function under every spin hypothesis remain constant, while the width of the probability density distribution decreases like $\sim \frac{1}{\sqrt{N}}$. To get precise figures one must carry out an explicit calculation.

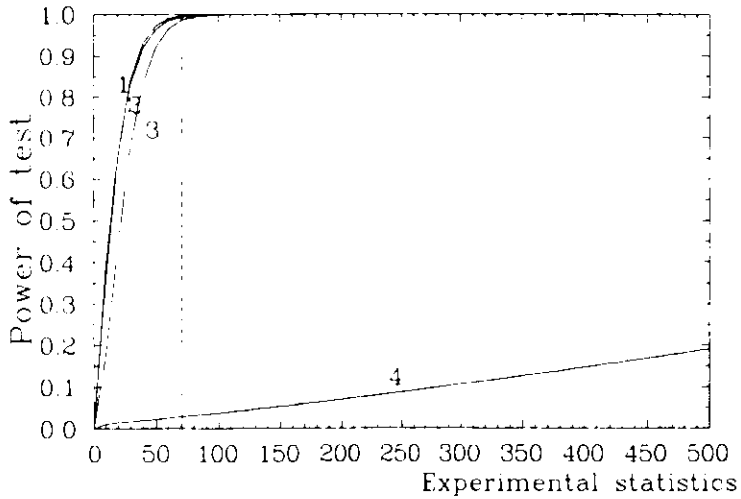

Figure 36.
The power of tests at 1 % significance level of the the spin 0 hypothesis for the spin 1 data as a function of the number of observed events. The dashed line indicates statistics available in our analysis.
The curves correspond to the following test functions :
$1 - \frac{1}{N}\sum ln(W_{J=1}/W_{J=0})$, $2 - \frac{1}{N}\sum ln(W_{J=0})$, $3 - \frac{1}{N}\sum ln(W_{J=1})$, $4 - \frac{1}{N}\sum ln(W_{J=2})$.

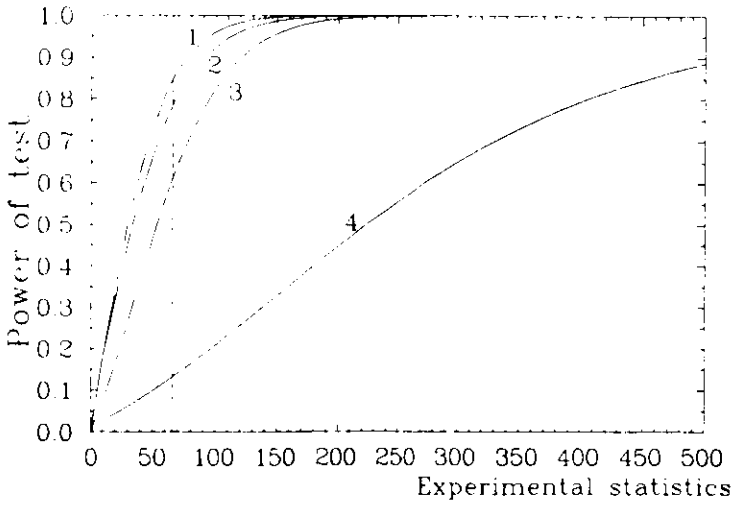

Figure 37.
The power of tests at 1 % significance level of the the spin 0 hypothesis for the spin 2 data as a function of the number of observed events. The dashed line indicates statistics available in our analysis.
The curves correspond to the following test functions :
$1 - \frac{1}{N}\sum ln(W_{J=2}/W_{J=0})$, $2 - \frac{1}{N}\sum ln(W_{J=0})$, $3 - \frac{1}{N}\sum ln(W_{J=1})$, $4 - \frac{1}{N}\sum ln(W_{J=2})$.

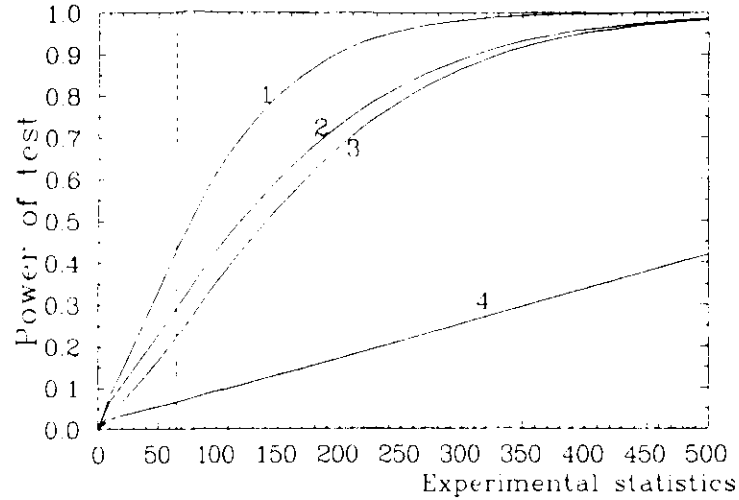

Figure 38.
The power of tests at 1 % significance level of the the spin 1 hypothesis for the spin 2 data as a function of the number of observed events. The dashed line indicates statistics available in our analysis.
The curves correspond to the following test functions :
1 $-\frac{1}{N}\sum ln(W_{J=2}/W_{J=1})$, **2** $-\frac{1}{N}\sum ln(W_{J=1})$, **3** $-\frac{1}{N}\sum ln(W_{J=0})$, **4** $-\frac{1}{N}\sum ln(W_{J=2})$.

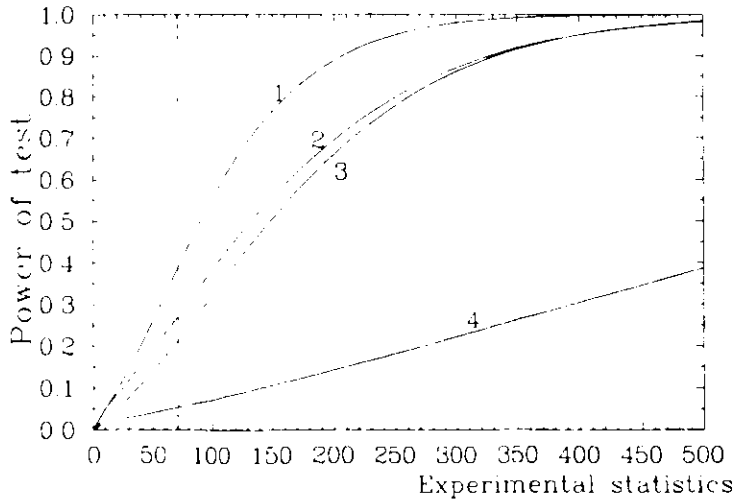

Figure 39.
The power of tests at 1 % significance level of the the spin 2 hypothesis for the spin 1 data as a function of the number of observed events. The dashed line indicates statistics available in our analysis.
The curves correspond to the following test functions :
1 $-\frac{1}{N}\sum ln(W_{J=2}/W_{J=1})$, **2** $-\frac{1}{N}\sum ln(W_{J=1})$, **3** $-\frac{1}{N}\sum ln(W_{J=0})$, **4** $-\frac{1}{N}\sum ln(W_{J=2})$.

If a spin hypothesis gets a low confidence level (we apply 1 % criterion) in the test, we will rule it out :

(V.2.d-1) $$\text{C.L.}(J_{hyp} = J_1) < 1\ \% \Longrightarrow J_{hyp} \neq J_1$$

One may calculate a probability of ruling out $J_{hyp} = J_1$ hypothesis, when the alternative hypothesis $J_{hyp}=J_2$ is true, (i.e. power of test [41]) by :

(V.2.d-2) $$\eta = \int_{-\infty}^{T_{1\%}^{J_{hyp}=J_1}} f(T,J_2)\,dT$$

where $T_{1\%}^{J_{hyp}=J_1}$ *is defined by*

$$\int_{-\infty}^{T_{1\%}^{J_{hyp}=J_1}} f(T\,J_1)\,dT = 0.01$$

(or integrating from $T_{1\%}^{J_{hyp}=J_1}$ *to* $-\infty$ *if* $f(T|J_2)$ *peaks on the right side of* $f(T\,J_1)$ *)*

Fig.36 – 37 show the power of spin 0 tests, based on different test functions, plotted as a function of the experimental statistics. As expected the likelihood ratio tests : $T = \frac{1}{N}\sum ln(W_{J=1}/W_{J=0})$ and $T = \frac{1}{N}\sum ln(W_{J=2}/W_{J=0})$, are the most powerful ones. However the logarithmic likelihood-0 test : $T = \frac{1}{N}\sum ln\,W_{J=0}$, is only mariginally worse. Tests based on likelihood-1 or likelihood-2 are less powerful. Given our statistics we should be able to rule out spin 0 for a spin 1 line (99.4 % probability), and we have a good chance to do so for a spin 2 line, too (78.6 % probability).

Fig.38 – 39 show the power of spin 1 and spin 2 tests. The likelihood ratio test : $T = \frac{1}{N}\sum ln(W_{J=2}/W_{J=1})$, is definitely the best one here, however our statistics may turn out to be too small to distinguish between spin 1 and 2.

The high transverse beam polarization considerably improved the sensitivity of our spin tests. We discuss this point in Appendix J.

V.2.e. Results of Spin Tests

In the first step of our spin analysis, we test the spin 0 hypothesis (J_{hyp}=0) for both observed states. As the alternative hypothesis is spin 1 or 2, we will use

(V.2.e-1) $$T(\Omega_1,\ldots,\Omega_N) = \frac{1}{N} ln \prod_{i=1}^{N} W_{J=0}(\Omega_i) = \frac{1}{N}\sum_{i=1}^{N} ln\,W_{J=0}(\Omega_i)$$

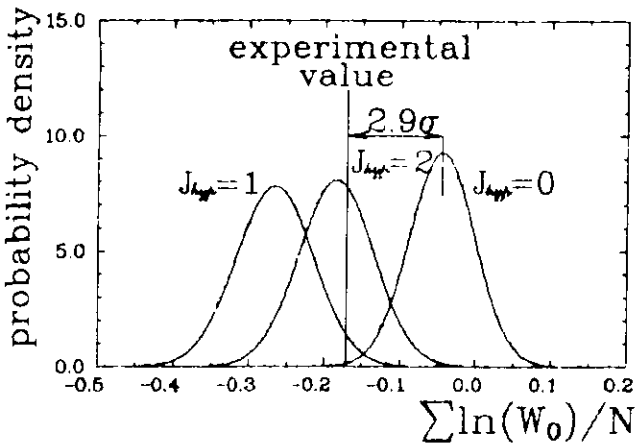

Figure 40.
The tests with use of the likelihood for spin 0 for the χ_b^α sample (expected spin 2). The gaussian curves represent the MC predictions of the test function distributions under the spin hypotheses J=0, 1, 2. The vertical line represents the value of the test function obtained from the real data. The units on both axes are arbitrary.

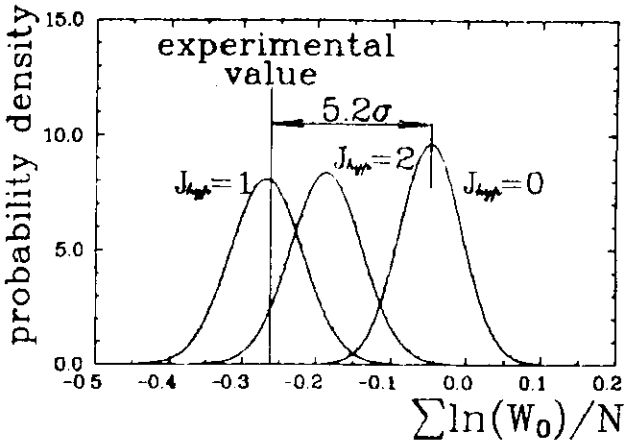

Figure 41.
The tests with use of the likelihood for spin 0 for the χ_b^β sample (expected spin 1).

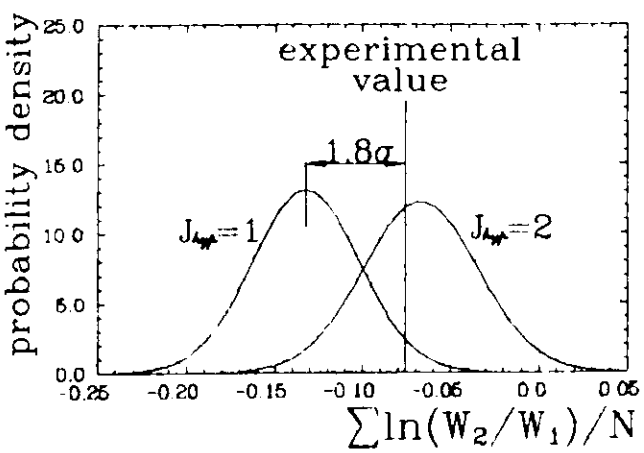

Figure 42.
The likelihood ratio tests for the χ_b^α sample (expected spin 2).

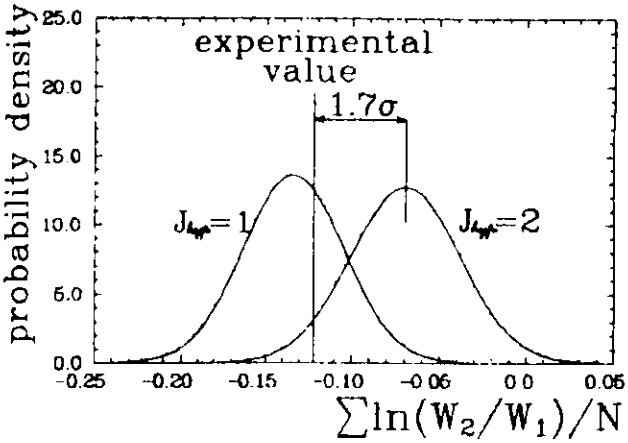

Figure 43.
The likelihood ratio tests for the χ_b^β sample (expected spin 1).

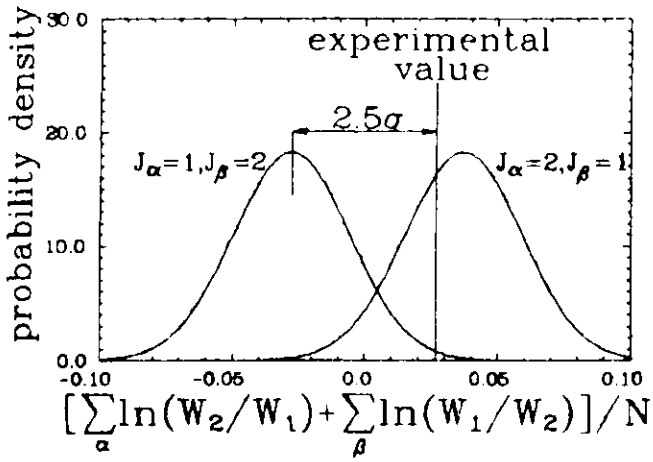

Figure 44.
The likelihood ratio tests for the combined data of χ_b^α and χ_b^β samples (expected spins $J_\alpha = 2$, $J_\beta = 1$).

as a test function, rather than performing two likelihood ratio tests. As shown in the previous section, the likelihood-0 test is almost as powerful as the likelihood ratio tests. Theoretical predictions, with detector effects folded in, for the probability density distribution of this test function under all three spin hypotheses are displayed for the χ_b^α sample in Fig.40, and for the χ_b^β sample in Fig.41. They are almost the same, since the number of observed events in both data samples is very similar. The value of the function applied to the χ_b^α sample is 2.9 standard deviations (σ) away from the spin 0 hypothesis (see also Table8.). This is equivalent to 0.2 % confidence level for this hypothesis being true (one side probability[1]). The disagreement with the spin 0 hypothesis is even greater for the χ_b^β sample (5.2σ), as expected from the spin 1 prediction for that state[2]. Therefore, spin 0 is ruled out for both observed χ_b states.

The data favour the expected spin 2 value for the χ_b^α sample, and spin 1 for the χ_b sample, however, the effect is not significant enough to draw a firm conclusion about the spin 1 and 2 assignment. The likelihood ratio tests :

$$\text{(V.2.e-2)} \qquad T(\Omega_1,\ldots,\Omega_N) = \frac{1}{N} ln \frac{\prod_{i=1}^{N} W_{J=2}(\Omega_i)}{\prod_{i=1}^{N} W_{J=1}(\Omega_i)} \quad \frac{1}{N}\sum_{i=1}^{N} ln\, W_{J=2}(\Omega_i)/W_{J=1}(\Omega_i)$$

displayed in Fig.42−43 show similar results. The data favour again the expected spins, but the confidence levels for the reverse spins, C.L.(J_α = 1) = 3.6 % and C.L.(J_β = 2) = 4.5 % , are not small enough to rule these hypotheses strictly out.

Once spin 0 has been ruled out for the both observed χ_b states, we can test global spin assignments : J_α = 1, J_β = 2 against J_α = 2, J_β = 1. The experimental statistics are doubled in this way. Of course, we assume here that the states cannot have the same spin, like in the quarkonium model. We use again the likelihood ratio test, with the test function :

$$\text{(V.1.e-3)} \qquad T(\Omega_1,\ldots,\Omega_N) = \frac{1}{N_\alpha + N_\beta} ln \frac{\prod_{i=1}^{N_\alpha} W_{J=2}(\Omega_i)\prod_{j=1}^{N_\beta} W_{J=1}(\Omega_j)}{\prod_{i=1}^{N_\alpha} W_{J=1}(\Omega_i)\prod_{j=1}^{N_\beta} W_{J=2}(\Omega_j)}$$

The data agree very well with the expected spin assignment : J_α = 2, J_β = 1 (Fig.44). The hypothesis J_α = 1, J_β = 2 has confidence level 0.6 %, and can be ruled out.

In principle, one may also test other spin hypotheses with the combined data, e.g. J_α=1, J_β=1. However, the results are not conclusive i.e. we cannot rule out this kind of the spin

[1]We calculate one side probability here, since the distributions of this test function under the alternative hypotheses, J_{hyp}= 1 and J_{hyp}=2, are on the same side (Fig.40) of the distribution for the tested J_{hyp}=0.
[2]The gaussian probability in only 0.00001 %, but it should be mentioned here, that we were not able to verify our systematic errors with precision greater than 0.00400 % (see Appendix H).

combinations. In fact, in every such test one combines a spin hypothesis favoured by one χ_b sample (high confidence level) with a spin hypothesis disfavoured by the other χ_b sample (low confidence level-see Table 8).

The result on spin 1 and 2 assignment is obtained under the assumption of pure electric dipole radiative transitions, as discussed in section V.2.a (the results for spin 0 are model independent). In fact, the data do not contradict this assumption, as the confidence levels for the expected spins are always high. In section V.3, we will show that a small admixture of M2 amplitude would strenghten our spin results for the χ_b^α sample.

Possible systematic effects in our spin analysis have been studied. The description of this study is presented in Appendix H. Table 8 summarizes all our spin results. The systematic uncertainties are indicated by quoting a range of confidence level. As can be seen from Table 8, the systematic errors are not large enough to alter our conclusions on the spin assignment of the observed χ_b states.

Table 8. Results of the spin tests with the systematic errors. The confidence levels are calculated assuming that an alternative hypothesis (J^{alt}_{hyp}) for J_{hyp}=0 is J^{alt}_{hyp} =1 or 2, for J_{hyp}=1 J^{alt}_{hyp}=2 and for J_{hyp}= 2 J^{alt}_{hyp} = 1.

State	Test Function	J_{hyp}	SD	CL in %
χ_b^α	$\sum ln W_0$	0	2.9	$0.2^{+0.3}_{-0.2}$
		1	1.9	3^{+5}_{-2}
		2	0.3	62^{+8}_{-4}
	$\sum ln (W_2/W_1)$	0	2.2	3^{+2}_{-2}
		1	1.8	4^{+6}_{-1}
		2	0.3	38^{+8}_{-4}
χ_b^β	$\sum ln W_0$	0	5.2	$0.00001^{+0.00400}_{-0.00001}$
		1	0.1	46^{+12}_{-4}
		2	1.6	6^{+1}_{-3}
	$\sum ln (W_2/W_1)$	0	3.6	$0.04^{+0.04}_{-0.02}$
		1	0.4	34^{+12}_{-4}
		2	1.7	4^{+1}_{-2}
χ_b^α-χ_b^β	$\sum_\alpha ln(W_2/W_1) + \sum_\beta ln(W_1/W_2)$	1,2	2.5	$0.6^{+1.2}_{-0.3}$
		2,1	0.5	31^{+11}_{-4}

V.3. Multipole Analysis

All radiative transitions in the cascade process were assumed to be of pure dipole character in our spin tests. The results of the tests showed full agreement with the expected χ_b spins, therefore with the dipole transitions as well. We can check, in addition, whether our data are consistent with some other multipole structure of the radiative transitions.

We assume for the moment that the χ_b^α is a spin 2 state, and that the spin of the χ_b^β is 1. Neglecting octupole transitions for spin 2 state, as justified in section V.2.a, we allow some admixture of the quadrupole amplitude (a_2), in addition to the dipole amplitude (a_1), in the first $\Upsilon' \to \gamma\chi_b$ or the second $\chi_b \to \gamma\Upsilon$ radiative decay. The multipole amplitudes are restricted by the relation V.1-15:

(V.3-1) $$a_1^2 + a_2^2 \propto \Gamma(\Upsilon' \to \gamma\chi_b) \quad or \quad \Gamma(\chi_b \to \gamma\Upsilon)$$

Therefore, the multipole structure of each transition can be described by one parameter, which we define by :

(V.3-2) $$\beta = arctan(a_2/a_1)$$

The case $\beta = 0°$ corresponds to pure dipole transition ("D"); $\beta = 90°$ to pure quadrupole transition ("Q"), and $\beta = 45°$ and $135°$ correspond to the equal contribution of both of them, with negative ("D-Q") or positive ("D+Q") relative sign, or equivalently to the pure χ_b helicity 1 or 0 amplitudes in the helicity frames of the decaying particle (see Fig.45).

The usual way to do the multipole analysis would be to use the normalized likelihood function to perform a maximum likelihood fit of the multipoles :

(V.3-3) $$ln\ L(\beta',\beta) = \sum_{i=1}^{N} ln(W_{J_{\chi_b},\beta'\beta}(\Omega_i)/C_{J_{\chi_b},\beta'\beta})$$

where :

β', β – *multipole parameters for the first* $\Upsilon' \to \gamma\chi_b$ *and the second* $\chi_b \to \gamma\Upsilon$ *transition, respectively,*

$C_{J_{\chi_b},\beta'\beta} = \int W_{J\beta'\beta}(\Omega)d\Omega$ – *normalization factor, the integration is performed over the acceptance region.*

a_1 - dipole amplitude
a_2 - quadrupole amplitude

$(a_1)^2 + (a_2)^2 \propto \Gamma(\Upsilon' \to \gamma\chi)$ or $\Gamma(\chi \to \gamma\Upsilon)$

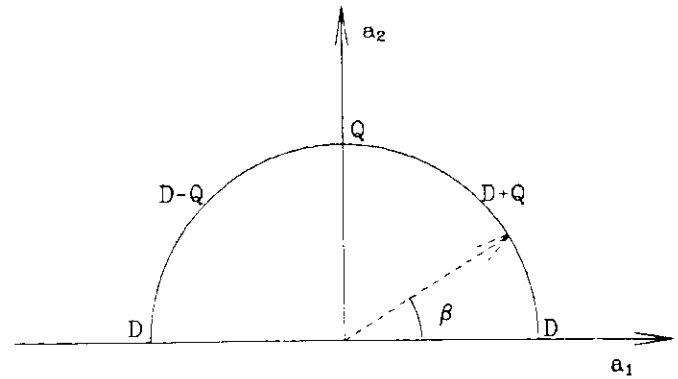

D - pure dipole transition
Q - pure quadrupole transition
D+Q - equal mixture with positive relative sign
(pure helicity 0 amplitude)
D-Q - equal mixture with negative relative sign
(pure helicity 1 amplitude)

Figure 45.
The definition of the parameter β which describes the multipole structure of the photon transition.

With our sample, however, this method does not lead to unambiguous results. Monte Carlo studies showed that the likelihood function always had more than one maximum, none of them being significantly higher than the others (Fig.46). In fact, our data exhibit the same behaviour. Probability statements deduced from this kind of fit are somewhat dubious. Therefore, we present instead, as multipole tests, an extention of the method applied for the spin tests, which yields unambigous results.

The spin tests under the assumption of dipole transitions implicitly meant testing the composite hypotheses about the spin and the dipole transition multipoles ($J_{hyp}, \beta' = 0, \beta = 0$). We can repeat the same testing procedure for any other combination of the multipoles. We test the hypotheses ($J_{hyp} = 2, \beta', \beta$) for the χ_b^α state and ($J_{hyp} = 1, \beta', \beta$) for the χ_b^β state. If the standard spin assignment is correct, a failure of the test means that the multipole combination (β', β) is wrong. The results of the likelihood ratio test, based on the test function :

$$\frac{1}{N}\sum_{i=1}^{N} ln\left[W_{J=2,\beta',\beta}(\Omega_i)/W_{J=1,\beta',\beta}(\Omega_i)\right] \qquad \text{(V.3-4)}$$

are plotted as a function of β' and β in Fig.47,48. Contours join hypotheses of the same confidence level in the test : $0\sigma, 1\sigma, 2\sigma \ldots$. Any combination of multipoles involving pure helicity 0 or 1 transitions can be excluded for the χ_b^β sample. Acceptable transitions occur in the regions, where transitions are either predominantly dipole or quadrupole. Pure quadrupole transitions are unlikely from the theoretical point of view, therefore at this assumption the χ_b^β data provides some indirect evidence for the dipole transitions. A precise measurement of a possible small admixture of quadrupole transitions needs higher statistics. The results for the χ_b^α sample are not conclusive, as the data agree with a wide range of transition multipole amplitudes.

We can also look at results of the multipole tests under the not expected spin assignment $J_\alpha = 1$, $J_\beta = 2$ (Fig.49,50) to see whether the failure of this spin hypothesis under the assumption of dipole transitions (section V.2) may be explained be the presence of quadrupole transitions. At least for the χ_b^α sample, any deviation from the dipole-dipole transitions[1] leads to even greater disagreement with the data.

Some multipole combinations may be excluded independently of the spin assumptions, namely, the common part of the multipole regions excluded under both spin 1 and 2 assignments. This is shown in Fig.51 for the χ_b' sample, and in Fig.52 for the χ_b^2 sample.

[1] But not involving pure quadrupole transitions.

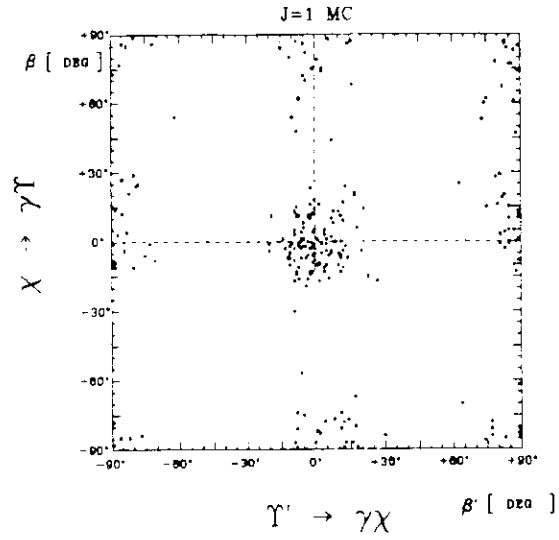

Figure 46.
The points represent the positions of the absolute maxima of the likelihood function V.3-3 found for the Monte Carlo generated experiments with pure electric dipole transitions ($\beta' = 0°, \beta = 0°$), spin 1 of the χ_b states and the statistics as observed in the real χ_b^β data sample. Not all the points cluster around the generated multipoles, showing that no reliable maximum likelihood fit of the multipoles can be obtained with our poor statistics.

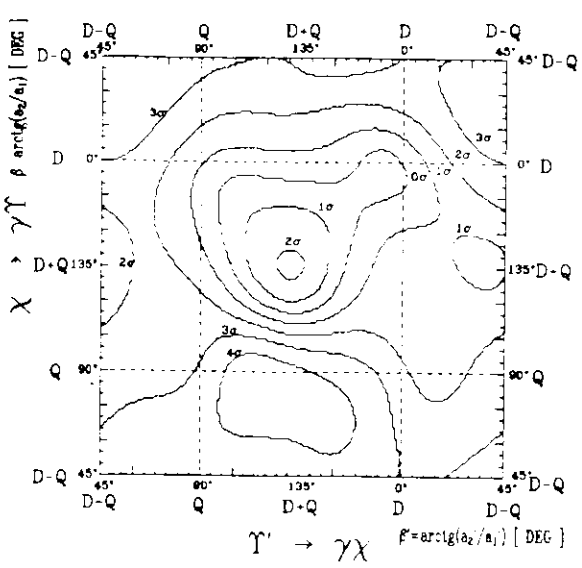

Figure 47.
The tests of the transition multipoles for the χ_b^α sample under the assumption of J_α=2 (expected spin). The confidence levels for rejection of the hypothesis (J= 2, β', β) using $\frac{1}{N}\sum ln(W_{J=2}/W_{J=1})$ as a test function are plotted.

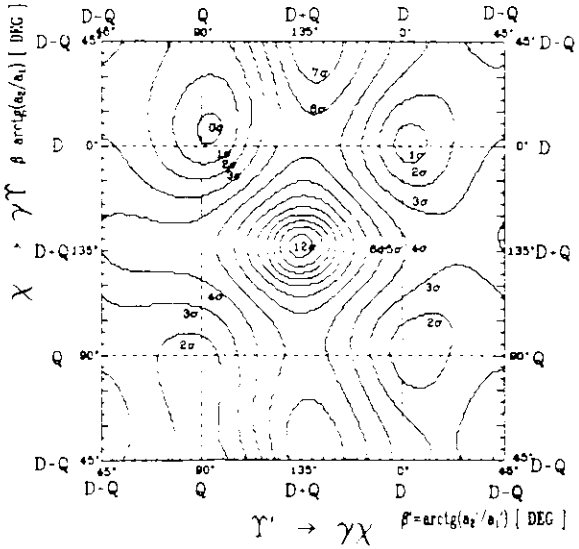

Figure 48.
The tests of the transition multipoles for the χ_b^β sample under the assumption of J_β=1 (expected spin). The confidence levels for rejection of the hypothesis (J= 1, β', β) using $\frac{1}{N}\sum ln(W_{J=2}/W_{J=1})$ as a test function are plotted.

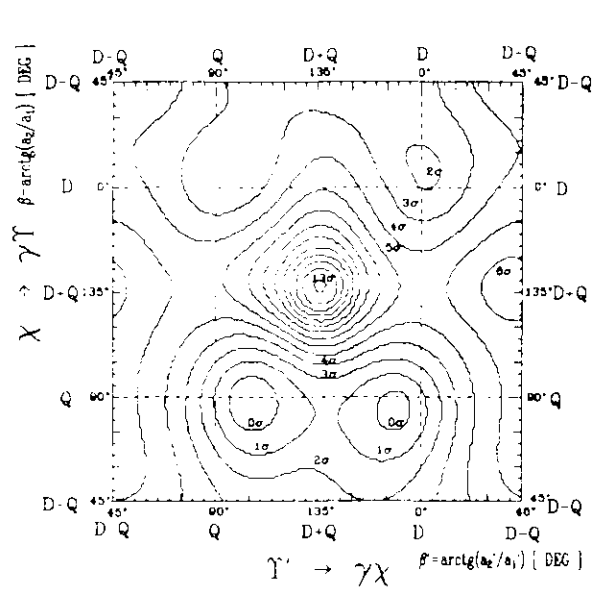

Figure 49.
The tests of the transition multipoles for the χ_b^α sample under the assumption of J_α=1 (not expected spin). The confidence levels for rejection of the hypothesis (J= 1, β', β) using $\frac{1}{N}\sum ln(W_{J=2}/W_{J=1})$ as a test function are plotted.

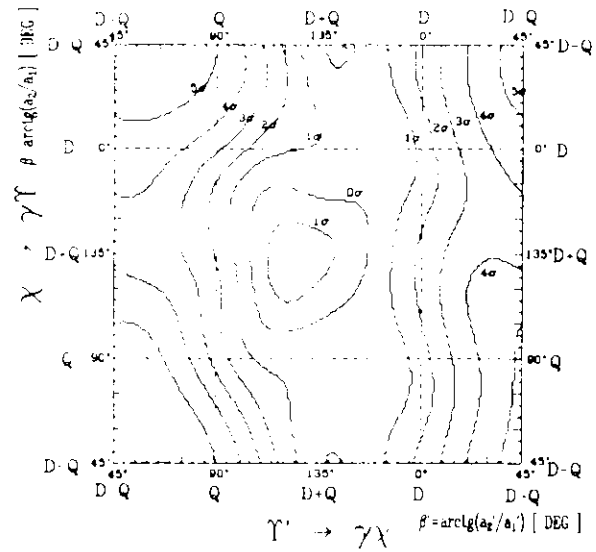

Figure 50.
Tests of the transition multipoles for the χ_b^β sample under the assumption of J_β=2 (not expected spin). The confidence levels for rejection of the hypothesis (J= 2, β', β) using $\frac{1}{N}\sum ln(W_{J=2}/W_{J=1})$ as a test function are plotted.

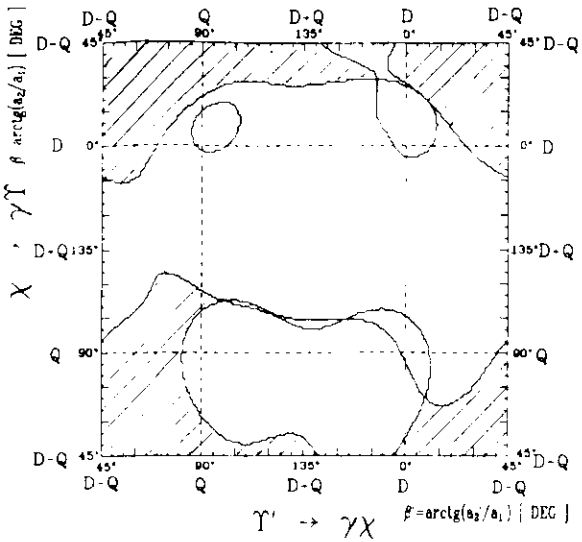

Figure 51.
The transition multipoles ruled out at 99 % *C.L.* confidence level (the shaded area) for the χ_b^a sample independently of a spin assumption.

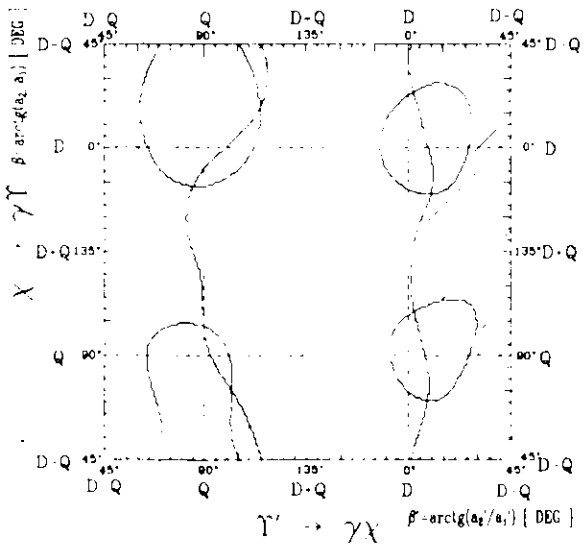

Figure 52.
The transition multipoles ruled out at 99 % *C.L.* confidence level (the shaded area) for the χ_b^b sample independently of a spin assumption.

VI. COMPARISON WITH THEORY

Bound heavy quark-antiquark systems, below the flavour thresholds, appear to be nonrelativistic (see section I.1). Nonrelativistic bound state spectroscopies, like the hydrogen atom or positronium, proved invaluable for the development of quantum mechanics and quantum electrodynamics (QED). As heavy quarkonia may play a similar role for quantum chromodynamics (QCD), an extensive theoretical investigation was devoted to them. We will discuss the results of our analysis in context of those efforts.

VI.1. Center-of-gravity Mass of χ_b States

In the nonrelativistic limit, a system of bound quark-antiquark ($Q\bar{Q}$) pairs should be well described by the Schrödinger equation with a static potential, accounting for the quark dynamics. The basic test of such a picture is how well it is able to reproduce masses of the observed $Q\bar{Q}$ excitations. Of course, in the strict nonrelativistic limit there is no room for spin forces. Therefore, fine and hyperfine level splittings cannot be reproduced. A comparison with the data is still possible by averaging over different spins of the same radial and orbital excitations ("center-of-gravity masses"). For the triplet-P states, the center-of-gravity is defined by :

$$M_{cog}(^3P) = \frac{\sum_{J=0}^{2}(2J+1)\cdot M_{^3P_J}}{\sum_{J=0}^{2}(2J+1)} = \frac{5M_{^3P_2} + 3M_{^3P_1} + M_{^3P_0}}{9} \qquad \text{(VI.1-1)}$$

Only $M_{^3P_2}$ and $M_{^3P_1}$ have been determined in our analysis. The complete mass measurement of all three 1P states has been obtained in our experiment by the inclusive analysis of photons from hadronic decays of the Υ'[31]. Combining results of these two independent studies, we improve errors on the masses of the spin 1 and 2 states, which are important for the calculation of center-of-gravity.

$$M_{1^3P_2}^{incl.+excl.} = (9914.3 \pm 1.3)\ \text{MeV} \qquad M_{1^3P_1}^{incl.+excl.} = (9890.5 \pm 1.3)\ \text{MeV}$$
$$M_{1^3P_0}^{incl.} = (9858.2 \pm 3.2)\ \text{MeV} \qquad \text{(VI.1-2)}$$
$$M_{cog}(1^3P_{J=0,1,2}) = (9900.1 \pm 0.9)\ \text{MeV}$$

We can obtain even better estimates by averaging over all experiments listed in Table.2 :

$M_{1^3P_2} = (9913.6 \pm 0.6)$ MeV $\quad M_{1^3P_1} = (9892.2 \pm 0.7)$ MeV $\quad M_{1^3P_0} = (9860.5 \pm 1.4)$ MeV

(VI.1-3) $$M_{cog}(1^3P_{J^{++}}) = (9900.6 \pm 0.4)\ \text{MeV}$$

Given this experimental result, we will discuss now its significance for tests of the potential models.

So far, the interquark potential has not been derived directly from the dynamics of the strong interaction. Exact QCD predictions are limited to the region of small interquark distances - R (or equivalently large momentum transfer - $\hat{Q}$), where perturbative calculations are valid. There is a hope that in the future, lattice methods will allow exact determination from QCD first principles of the $Q\bar{Q}$ static energy even in the nonperturbative region[43]. However, at the moment, one must fall back upon some phenomenological assumptions together with theoretical predictions.

There are two basic predictions of QCD which can be tested by a mass spectrum of heavy quarkonia : approximate flavour independence of the quark interaction, and the asymptotic freedom of quarks. The latter says that the strong coupling constant (α_s) tends to zero for small interquark distances. Self-coupling of gluons becomes, therefore, unimportant, and the colour interaction must resemble the electromagnetic forces ("one gluon exchange"). This leads to a simple Coulomb-like potential, predicted by QCD for the short range interaction :

(VI.1-4) $$V(R) = -\frac{4}{3}\frac{\alpha_s}{R}$$

The strong coupling constant depends on the interquark distance as well. This softens the Coulomb-like singularity at the origin by a logarithmic term. In the leading order of perturbative QCD :

(VI.1-5) $$V(R) \propto -\frac{1}{R\,ln(1/\Lambda R)} \qquad \Lambda = const$$

The Coulomb-like potential leads to approximate degeneracy of the 1P and 2S quarkonium levels. This prediction is clearly not supported by the data, since the χ_b masses are significantly lower than the Υ' mass. Consequently, there must be a nonperturbative contribution to the interquark potential.

At large distances QCD calculations on a lattice predict[44] a nearly linear potential. This is also indicated by linearity of the Regge trajectory in light meson spectroscopy.

(VI.1-6) $$V(R) \propto R$$

At intermediate distances, there is no theoretical hint for the shape of the interquark potential. A number of phenomenological interpolations between these two asymptotic behaviours have been proposed. Some other models do not use any theoretical arguments. They check whether the success of QCD-like models really provides evidence in favour of QCD or just demonstrates their consistency with the experimental data.

The potentials involve one or more free parameters, which are adjusted to the data. In addition, quark masses are not known, since quarks are permamently confined. A quark mass is also fitted to the data.

A long, but probably still incomplete, list of the potential model predictions for the χ_b center-of-gravity mass is presented in Table 9 . As the overall fit to all measured $b\bar{b}$ levels is more meaningful than just a prediction for the χ_b mass, we also list predictions for the 2P, 2S, 3S and 4S levels. The data are taken from the Particle Data Group[19]. The experimental errors are below 1 MeV except for the 2P c.o.g. mass ($\pm$2 MeV) and 4S mass ($\pm$4 MeV). As the $\Upsilon(1S)$ mass is commonly used to set the energy scale of the theoretical predictions (via b-quark mass), we shifted all theoretical masses to get the $\Upsilon(1S)$ mass exactly at the measured value [1]. Of course, accuracy of the predictions may still be affected by the quality of the other input data used. We supply the date of the publication on account of this issue. The smaller the number of parameters tuned to the data, the stronger the theoretical implications. Thus, the number of free parameters in the model is also put into the table. The type of the potential is characterized by its behaviour at short ($R \leq 0.1$ fm), intermediate ($0.1 \leq R \leq 1.0$ fm), and long (1.0 fm$\leq R$) range of the interquark distance. Symbols to describe the short range potential have the following meaning :

C-0 : simple Coulomb potential (Eq.VI.1-4);

C-1 : Coulomb potential with logarithmic correction due to asymptotic freedom (Eq.VI.1-5);

C-2 : two loop perturbative expansion of α_s over the Coulomb term (Ref. 9);

C-3 : QCD potential to the fourth order in the perturbative theory (Ref.6).

The large distance form of the potential is indicated by its R dependence. An abbreviation for the intermediate potential says whether interpolation between the asymptotic behaviours was performed, or a simple sum of the short and long range potentials was assumed. As a figure of merit, we have calculated the mean deviation of theoretical predictions from the data for the levels below the flavour threshold (1P, 2P, 2S, 3S). Contribution of the experimental

No.	Author(s)	Date	Potential			Para-	Input	$M_{theory} - M_{data}$					
			short	interm.	long	meters	data	1P	2P	2S	3S	4S	mean*
21	Kang[63]	79/08	C-0	int.	R	5	$c\bar{c}$	−42	−2	−23	+24		23
22	Beavis et al.[64]	79/04	C-1	int.	R	5	$c\bar{c}$	−51	−21	−27	+8	+94	27
23	Celmaster et al.[65]	77/09	C-1	int.	R	4	$c\bar{c}$	+16	+32	+37	+35	+107	30
24	Heikkilä et al.[66]	83/02	C-0	sum	$\sqrt[3]{R^2}$	3	$c\bar{c}$,$b\bar{b}$	−23	−24	−23	−50	−48	30
25	Fogleman et al.[67]	79/08	C-1	int.	R	1	$c\bar{c}$	−32		−23	−36	+7	30
26	Beavis et al.[68]	78/12	C-0	sum	R	3	$c\bar{c}$	−51		−43	+3	+107	32
27	Lichtenberg et al.[69]	78/06	C-1	int.	R	2	$c\bar{c}$	−52		−33	−16	+37	34
28	Crater,Van Alstine[70]	84/01	C-1	int.	R	1	$b\bar{b}$	−28	−40	−35	−38	+6	36
29	Carlson et al.[71]	83/06	C-0	sum	R	3	$b\bar{b}$	−30	−37	−40	−36	+23	36
30	Grotch et al.[72]	84/04	C-2	int.	R	2	$b\bar{b}$	−31	−49	−36	−26		36
31	Stanley,Robson[73]	79/11	C-0	sum	R	4	$c\bar{c}$	−62		−12	−36		37
32	Eichten et al.[74]	79/06	C-0	sum	R	2	$c\bar{c}$	+57	+51	+28	+40	+100	44
33	Bhaduri et al.[75]	81/04	C-0	sum	R	3	$c\bar{c}$	+60		+32	+46	+108	46
34	Pignon,Piketty[76]	78/01	C-1	sum	R	3	$c\bar{c}$	+28		+48	+110	+210	62
35	Jena[77]	82/12	$A + B\,log(1 + R)$			2	$c\bar{c}$	−100	−80	−47	−45	−12	68
36	Barik,Jena[78]	80/10	C-0	sum	$R^{\dagger}$	3	$c\bar{c}$	−120		−47	−94		87
37	Lichtenberg et al.[79]	77/07	C-0	sum	R	3	$c\bar{c}$	−142	−142	−142	−105	−33	126
	Baacke et al.[80]	81/10	BAG			3	$c\bar{c}$,$b\bar{b}$	+70	+51	−3	+10	+105	34

*Excluding 4S, which is above the flavour threshold.
†With light quark pairs screening potential.
‡Gluon condensate. #With cut-off.

Table 9. Predictions of potential models for the spin averaged mass spectrum in the $b\bar{b}$ system.

No.	Author(s)	Date	Potential			Para-	Input	$M_{theory} - M_{data}$					
			short	interm.	long	meters	data	1P	2P	2S	3S	4S	mean*
1	Moxhay,Rosner[45]	83/04	C-1	int.	R	3	$c\bar{c}$,$b\bar{b}$	+6	−3	−3	−4	+34	4
2	Gupta et al.[6]	82/06	C-3	sum	R	3	$c\bar{c}$,$b\bar{b}$	−3	−5	−12	−3		6
3	Buchmüller et al.[9]	80/04	C-2	int.	R	2	$b\bar{b}$	−11	−11	−3	−6	+47	8
4	McClary,Byers[46]	83/06	C-0	sum	R	4	$c\bar{c}$,$b\bar{b}$	+22	+6	−3	0	+47	8
5	Richardson[47]	78/12	C-1	int.	R	1	$c\bar{c}$	−5	−12	−8	−9	+33	9
6	Bhanot, Rudaz[48]	78/04	C-0	int.	R	3	$c\bar{c}$	−12	−11	−2	−15	+28	10
7	Eichten,Feinberg[49]	80/12	C-0	sum	R	2	$c\bar{c}$,$b\bar{b}$	+24	+10	−3	+3		10
8	Bander et al.[50]	83/04	C-1	sum	$R^{\#}$	3	$c\bar{c}$,$b\bar{b}$	−10	−13	0	−22	+5	11
9	Quigg,Rosner[51]	79/05	$A\,log(R/B)$			2	$c\bar{c}$	−1	+9	+26	+14	+27	13
10	Ram,Leon[52]	82/11	$A + B \cdot R^{\alpha}$			3	$c\bar{c}$,$b\bar{b}$	−30		+7	−4	+5	14
11	Quigg,Rosner[53]	81/02	inverse scattering			—	$c\bar{c}$	+17		−5	+23	+23	15
12	Levine[54]	79/08	C-1	int.	R	1	—	−31	−11	−13	+5	+77	15
13	Krasemann,Ono[55]	79/02	C-1	int.	R	4	$c\bar{c}$,$b\bar{b}$	−13		−8	−28	+2	16
14	Soni,Tran[56]	81/11	C-0	$\langle 0\|GG\|0\rangle^{\ddagger,\dagger}$		3	$c\bar{c}$	−21		−23	+5		16
15	Martin[57]	80/11	$A + B \cdot R^{\alpha}$			3	$c\bar{c}$,$b\bar{b}$	−40	−19	+2	+5	+27	17
16	Khare[58]	80/10	$A + B \cdot R^{\alpha}$			3	$c\bar{c}$,$b\bar{b}$	−30					
17	Abe et al.[59]	82/09	C-2	int.	R	3	$b\bar{b}$	−31	−21	−13	−6	+37	18
18	Ono[60]	80/06	C-1	int.	R	4	$c\bar{c}$,$b\bar{b}$	−47	−24	0	−6	+27	19
19	DeCarvalho et al.[61]	81/11	C-0	sum	$\sqrt{R}$	3	$c\bar{c}$,$b\bar{b}$	−33	−22	−17	−10	+34	21
20	Hiller[62]	84/03	C-0	bag	R	3	$c\bar{c}$,$b\bar{b}$	+41	+28	0	+14	+78	21

errors to this mean deviation is small compared to theoretical uncertainties. The potential models are listed in sequence of increasing mean deviation from the data.

We will discuss now what can be seen from Table 9. The interquark potentials were originally developed to describe the charmonium system. As soon as the Υ resonance was discovered, they were applied to predict $b\bar{b}$ levels (see e.g. model No.37 in Table 9). Many potentials constrained to the ψ data describe the Υ system reasonably well, without any retuning of the parameters[1] (models No. 5,6,9,11). This proves the flavour independence of the quark dynamics[2], giving strong support to QCD. The flavour independence was demonstrated in a model independent way by Quigg and Rosner[53] (model No.11). They used the inverse scattering method to construct the interquark potential with no a priori assumptions according to its shape.

A QCD motivated potential, in its simplest form, was proposed by Eichten et al.[81] :

$$V(R) = -\frac{4}{3}\frac{\alpha_s}{R} + \frac{R}{a^2} \qquad \alpha_s, a = const \tag{VI.1-7}$$

It was successfully applied to the ψ family, and later on to the $b\bar{b}$ system (model No.7). More sophisticated models implement logarithmic softening of the Coulomb part by the "running" coupling constant. The model proposed by Richardson [47] was especially simple and successful (model No.5). He modified the lowest order QCD formula for the running coupling constant :

$$\alpha_s(Q^2) = \frac{12\pi}{33-2n_f}\frac{1}{ln(Q^2/\Lambda^2)} \quad \rightarrow \quad \frac{12\pi}{33-2n_f}\frac{1}{ln(1+Q^2/\Lambda^2)} \tag{VI.1-8}$$

$$V(R) = \int d^3\vec{Q}\, e^{i\vec{Q}\vec{R}}\,\frac{\alpha_s(Q^2)}{Q^2}$$

where :

n_f – *number of the light flavours (=3),*

Λ – *QCD scale parameter.*

to get a linear potential in the limit of large R (small Q^2), and still the correct form at small R (large Q^2) given by Eq. VI.1-5. His model involves only one free parameter (Λ) and gives a very good fit to the $b\bar{b}$ levels, even while using $c\bar{c}$ data to fix the value of Λ. The next-to-leading order QCD calculation must be performed to relate Λ to the true QCD scale

[1] except, of course, for the quark mass.

[2] at the interquark distances $0.1 \leq R \leq 1.0$ fm, probed by the $c\bar{c}$ and $b\bar{b}$ quarkonia levels (as we will discuss later).

parameter (e.g. $\Lambda_{\overline{MS}}$) correctly. This was done by Buchmüller et al. [9] (model No.3). Models of Richardson and Buchmüller et al. were studied also by other authors (models No. 1, 17, 28, 30). Gupta et al. [6] went even further, calculating the potential to fourth order in perturbative QCD (model No.2). Supplemented with linear confinement, their model predicted exactly the χ_t center-of-gravity mass and reproduced other $b\bar{b}$ and $c\bar{c}$ levels, with mean deviation from the data of only 6 MeV (~0.06 % of a mass, ~1 % of an excitation energy !). As we will discuss in the next section, this model also predicts correctly spin dependent mass shifts in the heavy quarkonia.

Although success of the QCD-like models is apparent, the question remains whether it really proves validity of the QCD expectations or just shows their consistency with the presently available experimental data. This question was explicitly brought up by Martin, who described very successfully the level spacings in charmonium and vector states of the Υ system, by a simple power law potential :

$$V(R) = A + B \cdot R^{\alpha} \qquad \alpha \simeq 0.1 \tag{VI.1-9}$$

Our measurement of the χ_b masses, together with the other recent experiments, shows, however, that this kind of potential gives center-of-gravity mass for the χ_b states which is off by 30-40 MeV (models No.10, 15, 16). This was foreseen by Khare (model No. 16) a long time ago [58] . One may explain this by small sizes[1] of the 1P $b\bar{b}$ states, which are the second smallest among known quarkonia states (see section I.2 and Fig.53), thus $M_{\chi_b} - M_{\Upsilon}$ probes interquark forces at smaller distances than the other levels. This is actually the first hint from the level spacings of quarkonia that the Coulomb-like singularity is indeed necessary for an exact description of the data. The power law potential is reduced to the logarithmic potential in the limit of small power $\alpha \rightarrow 0$. The logarithmic potential was studied by Quigg and Rosner[51], who noticed that it gave level spacings independent of the quark mass, which was quite close to the experimental values : $M_{\psi'} - M_{\psi} \simeq 590$ MeV, $M_{\Upsilon'} - M_{\Upsilon} \simeq 563$ MeV. They predicted (model No.9) the χ_b mass exactly , however at the expense of a worse fit to the $\Upsilon(2S)$ and $\Upsilon(3S)$ masses. The modified logarithmic potential of Jena[77] (model No. 35) fits the data even worse, again with large underestimation of the χ_b mass.

There is another observable which is sensitive to the short range potential predicted by the potential models. We mean here the leptonic widths of the n^3S_1-- states, which is

[1] In the potential models, one calculates a mean square radius for the energy level as a measure of the size of the corresponding bound state.

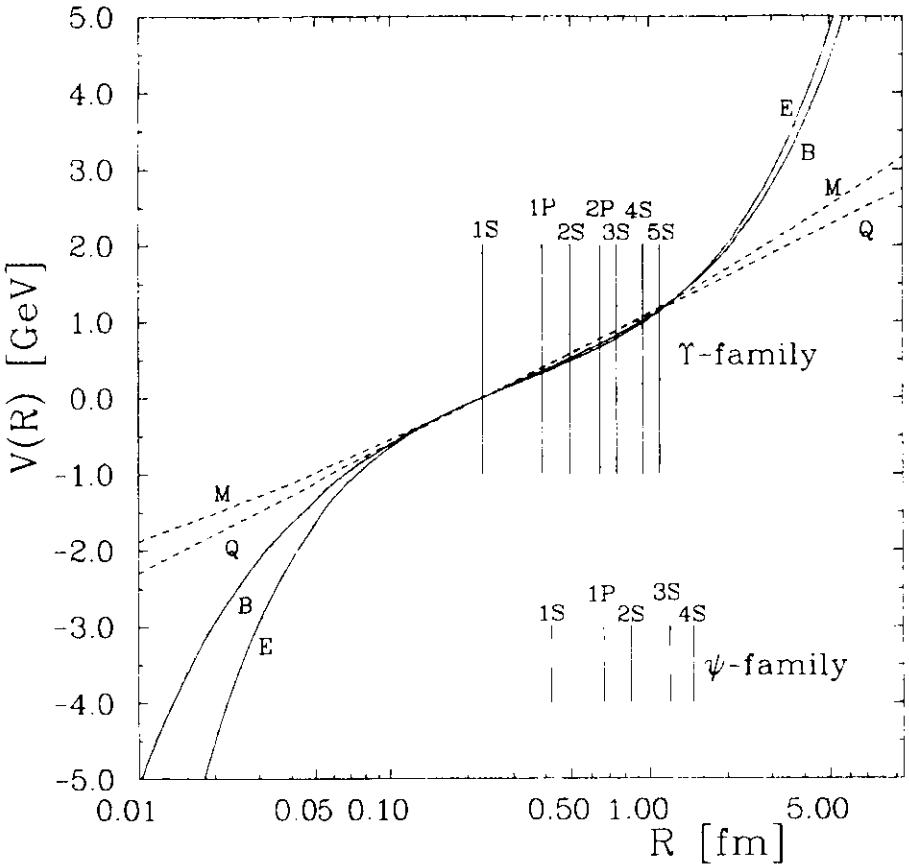

Figure 53.
The comparison of few $b\bar{b}$ potentials.
The solid lines show the QCD motivated potentials by Eichten et al.[49] (E) and Buchmüller et al.[9] (B). Purely phenomenological potentials by Martin[57] (M) and Quigg, Rosner[51] (Q) are represented by the dashed lines. The calculated[9] sizes of the $b\bar{b}$ and $c\bar{c}$ quarkonia are indicated. All potentials have been shifted to cross the zero at the radius of Υ (0.23 fm). Note logarithmic scaling of the x-axis.

sensitive to the wave function at the origin :

$$\Gamma_{ee}(n^3S_{1^-}) = \frac{4\pi e_Q^2 \alpha_{QED}^2}{m_Q^2} \phi(0)^2 \qquad \text{(VI.1-10)}$$

Usually one uses ratios of the leptonic widths of the different radial excitations, which are more reliable theoretically. Most of the QCD motivated models reproduce the experimental results very well. Martin's potential again seems to be in some trouble here[82].

Experimental evidence for the linear confining potential is even weaker than for the Coulombic part. Differences between the linear and logarithmic confinement models appear only at distances larger then 1.0 fm (see picture 53), which can be probed only by quarkonia levels above the flavour threshold. A single-channel analysis with static potential cannot be correct for those short-lived states. An effect of direct $\Upsilon(4S)$ decays into $B\bar{B}$ pairs on the potential model predictions can be seen from Table 9. Predictions of a typical model perfectly fitting masses of the states below the flavour threshold overestimate the mass of the Υ''' by 30-50 MeV.

Generally speaking, the purely phenomenological power law and logarithmic potentials are not much worse than the QCD motivated models. In addition, many different implementations of the QCD asymptotic behaviours do not differ much in the mass predictions. One may understand this by comparison of the sizes of the $c\bar{c}$ and $b\bar{b}$ states, with the different potentials. Although different analytically, all potentials are almost the same numerically in the region of interquark distance $0.1 \leq R \leq 1.0$ fm, which is actually probed by known quarkonia states (Fig.53). Masses of the lowest excitations of the heavier $t\bar{t}$ quarkonia will probe the region below 0.1 fm, thus distinguishing between QCD and non-QCD potential models.

Accuracy of the mass predictions by the nonrelativistic potential models for the heavy quarkonia up to few MeV is really amazing. It finally proves a quark structure of mesons, which was not that clear in the spectroscopy of light mesons.

The great success of phenomenological potential models has not been fully understood theoretically. The relativistic corrections[1] to the nonrelativistic predictions for the level spacings should be of order $< \frac{v}{c} >^2$, i.e. ~8 % in the $b\bar{b}$ system and ~30 % in the $c\bar{c}$ system[9]. This would give ~ 30 MeV correction to the $M_{\chi_b} - M_\Upsilon$ splitting, which is much larger than

[1] We mean here spin independent corrections, which might shift, for example, c.o.g. mass of the χ_b states. The spin dependent relativistic corrections, which generate fine splitting of the χ_b states will be discussed in the next section.

precision of the potential models. Most likely, the leading spin independent corrections are absorbed into the nonrelativistic potential via adjusting parameters to the data. Indeed, nonrelativistic models sometimes give reasonable predictions for even lighter mesons than the J/ψ[57,75]. Recently some authors[45,46,72] attempted to implement perturbatively the first order spin-independent corrections to the mass predictions in a consistent way (models No.1, 4, 30). Actually, one of them gives the best fit to the present experimental data (model No.1). Some other authors [50,52,70] tried to apply relativistic schemes different from the perturbed-Schrödinger calculations (models No. 8, 10, 28). They seem not to improve agreement with the data for the heavy quarkonia, but thanks to the nonperturbative relativistic calculations, these potential models (models No 10, 28) were successfully applied to the mesons build up from the light quarks : u, d and s.

In addition, quantum effects of coupling bound $Q\bar{Q}$ states below the flavour threshold to virtual light quark loops must shift masses of the quarkonium states [74]. The recent calculations of Heikkilä, Törnqvist and Ono[60] give mass shifts of 80-190 MeV for $c\bar{c}$ states and 30-60 MeV for the $b\bar{b}$ states, below the flavour thresholds. However, their attempt (model No. 24) to fit the mass spectrum corrected for coupled channel effects does not really improve agreement with the data. Again, dominant coupled channel effects can be absorbed into a redefinition of the potential parameters and quark masses.

In view of the evidence from QCD sum rules for existence of the nonvanishing nonperturbative gluon condensate in the QCD vacuum, the potential description of the static limit of QCD might be questionable[83]. If those arguments are right, the $Q\bar{Q}$ potential will have only pure phenomenological meaning.

We are at a good point to discuss another, quite different from the potential approach, method of predicting quarkonia features. It was proposed by Shifman, Vainshtain and Zakharov[84] and called : "QCD sum rules." It combines experimental information on the quarkonium vector states (masses, and leptonic widths), with theoretical calculations under the framework of perturbative QCD, and phenomenological corrections for the nonperturbative effects due to a possible gluon condensate in the QCD vacuum. A four parameter fit[1] of the QCD sum rules predictions gives excellent agreement with the masses of the $1^1S_{0^{-+}}$, $1^3S_{1^{--}}$, $1^3P_{2^{++}}$, $1^3P_{1^{++}}$, $1^3P_{0^{++}}$ charmonium levels and correctly reproduces the

[1] Quark mass, strong coupling constant , gluon condensate and threshold energy for continuum production of the heavy quarks are free parameters in QCD sum rule calculations.

leptonic width of the J/ψ[85]. The QCD sum rules were also applied to the spectroscopy of light mesons and bayrons[85]. However, there is a serious disadvantage of the QCD sum rules. Their predictions are limited to the lowest lying levels in each partial wave. The method also encounters severe problems in predicting correctly the χ_b masses. Voloshin predicted [86] $M_{ccg}(\chi_b) = (9830 \pm 30)$ MeV and Bertlman [87] obtained $M_{ccg}(\chi_b) = 9803$ MeV, using a different approach in calculation. These predictions are much worse than even bad fits of the potential models. Although one may argue [85] that those failures should be attributed to the specific calculations, rather than to the QCD sum rules in general, they demonstrate a level of theoretical uncertainty in some of the applications of QCD sum rules.

Finally, there were attempts to apply the bag models to predict masses in the $b\bar{b}$ system. In adiabatic approximation, the bag model predicts just a static potential. For an example see Ref.62 (model No. 20). The bag model was used in a self-consistent way to predict $b\bar{b}$ levels by J. Baacke et al. [8] . Their predictions fit the S-wave masses very well, but differ from the potential models by significant overestimation of the P-wave masses, especially of the $\chi_{b'}$ mass (see the last model in Table 9).

VI.2. Fine Structure of χ_b States

The χ_b states are split into three different mass levels by spin-dependent interquark forces. Spin-dependent effects are genuinely relativistic. In fact, the 1^3P_2-1^3P_1 mass splitting is ~46 MeV in the $c\bar{c}$ system, whereas we have observed in our analysis only ~24 MeV in the Υ family. This demonstrates the relativistic nature of this mass splitting, which must decrease with heavier quark mass. As we have seen in the previous section, the nonrelativistic description with static interquark potential works very well for spin-averaged mass spectra. Therefore, one hopes that spin-dependent effects can be calculated as a weak perturbation of the nonrelativistic results.

Although a static potential has not yet been derived directly from QCD, a general structure of the spin-dependent relativistic corrections to the nonrelativistic potential can be deduced from QCD itself. Calculations done by Eichten and Feinberg [49], and further studies by Gromes[88] show that spin-dependent corrections to the potential, up to order $1/m_Q^2$, can

be written in the form :

$$V_{spin}(R) = \underbrace{\frac{\vec{L}\cdot\vec{S}}{2m_Q{}^2}\,\frac{1}{R}\frac{d}{dR}\,(3V_{NR}(R) + 4V_{LS}(R))}_{\text{spin-orbit interaction}}$$

(VI.2-1)

$$+\underbrace{\frac{3(\vec{S}_1\cdot\hat{R})(\vec{S}_2\cdot\hat{R}) - \vec{S}_1\cdot\vec{S}_2}{12m_Q{}^2}\,V_T(R)}_{\text{tensor interaction}}$$

$$+\underbrace{\frac{\vec{S}_1\cdot\vec{S}_2}{3m_Q{}^2}\,V_{SS}(R)}_{\text{spin-spin interaction}}$$

Here V_{NR} denotes static potential, and V_{LS}, V_T, V_{SS} are additional potentials describing spin-dependent forces. In the future, all these potentials should be derived directly from QCD by Monte Carlo methods on lattice[89]. At the moment, they are products of various phenomenological models.

Usually one wants, by analogy with QED, to relate the unknown potentials V_{LS}, V_T, V_{SS} to the static potential V_{NR}. To do that, one must specify what kind of interaction in the relativistic case has led in the static limit to V_{NR}. Namely, a Lorentz structure of the exchange operator has to be specified. In QCD-like models, the short range potential is believed to come from the exchange of a vector gluon. Therefore[86], like in QED :

(VI.2-2) $$V_{LS}^{vect} = 0 \quad V_T^{vect} = -\left(\frac{d^2}{dR^2} - \frac{1}{R}\frac{d}{dR}\right)V_{NR}^{short} \quad V_{SS}^{vect} = 2\,\nabla^2 V_{NR}^{short}$$

The nature of the long range confining interaction is not known a priori. We hope to learn something about that from the data themselves. Some early models[69] assumed that the long range potential is of the vector type, too. This was also investigated as an option in more recent works[50,72]. In this case, structure of the confining spin forces is also given by Eq.VI.2-2. As confinement in QCD corresponds to exchange of large numbers of self-coupling gluons, it is rather unconvincing that the vector exchange is preserved at large interquark distances. Thus, most of the model builders assume scalar exchange[46,71,6,50,67,72,76,90], or some mixture of those two[68,58,78,64]. The scalar interaction gives :

(VI.2-3) $$V_{LS}^{scal} = -V_{NR}^{long} \qquad V_T^{scal} = 0 \qquad V_{SS}^{scal} = 0$$

Generally, for $V_{NR} = V^{vect} + V^{scal}$ one obtains :

$$V_{spin} = \frac{\vec{L}\cdot\vec{S}}{2m_Q{}^2}\,\frac{1}{R}\frac{d}{dR}(3V^{vect} - V^{scal})$$

$$-\frac{3(\vec{S}_1\cdot\hat{R})(\vec{S}_2\cdot\hat{R}) - \vec{S}_1\cdot\vec{S}_2}{12m_Q{}^2}\left(\frac{d^2}{dR^2} - \frac{1}{R}\frac{d}{dR}\right)V^{vect}$$

(VI.2-4)

$$+\frac{2\vec{S}_1\cdot\vec{S}_2}{3m_Q{}^2}\,\nabla^2 V^{vect}$$

If the confining interaction is of the effective scalar type, tensor and spin-spin forces are purely short-range, and confinement shows up only in the spin-orbit term. On the other hand, vector confinement would contribute long range components to all three spin dependent corrections.

Spin-spin forces cause a hyperfine splitting (i.e. between the singlet and triplet levels). It was measured experimentally in the $c\bar{c}$ system for the 1S and 2S levels. The observed splitting can be well reproduced by a short range potential derived from QCD [91]. Hence there is no evidence for any long range contribution in the spin-spin force.

Spin-orbit and tensor forces can be studied by fine structure of quarkonium orbital excitations. Spin dependent corrections to the mass of the $^3P_{J=}$ states, can be obtained from :

(VI.2-5) $$\Delta M = a_{LS} <\vec{L}\cdot\vec{S}>_J + a_T <3(\vec{S}_1\cdot\hat{R})(\vec{S}_2\cdot\hat{R}) - \vec{S}_1\cdot\vec{S}_2>_J + a_{SS} <\vec{S}_1\cdot\vec{S}_2>_J$$

where :

$$a_{LS} = \frac{1}{2m_Q{}^2} <1P|\frac{1}{R}\frac{d}{dR}(3V^{vect} - V^{scal})|1P>$$

(VI.2-6)

$$a_T = \frac{1}{12m_Q{}^2} <1P|\left(\frac{d^2}{dR^2} - \frac{1}{R}\frac{d}{dR}\right)V^{vect}|1P>$$

$$a_{SS} = \frac{2}{3m_Q{}^2} <1P|\nabla^2 V^{vect}|1P>$$

Since all triplet 1P states have the quark spins in the same configuration, the spin-spin force does not contribute to the relative splitting and can be absorbed into the center-of-gravity mass[1].

(VI.2-7) $$<\vec{L}\cdot\vec{S}>_J = \begin{pmatrix} +1 \\ -1 \\ -2 \end{pmatrix} \quad <3(\vec{S}_1\cdot\hat{R})(\vec{S}_2\cdot\hat{R}) - \vec{S}_1\cdot\vec{S}_2>_J = \begin{pmatrix} -\frac{2}{5} \\ +2 \\ -4 \end{pmatrix} \quad for\ J = \begin{pmatrix} 2 \\ 1 \\ 0 \end{pmatrix}$$

[1] Spin-spin forces would cause a shift between the center-of-gravity mass of the triplet $^3P_{J=}$ and the singlet $^1P_{1=}$, however the singlet-P states will be very difficult to observe experimentally for the $b\bar{b}$ quarkonia.

thus :

$$
\begin{aligned}
M_{^3P_2} &= M_{cog} - a_{LS} - \frac{2}{5} a_T \\
M_{^3P_1} &= M_{cog} - a_{LS} + 2 a_T \\
M_{^3P_0} &= M_{cog} - 2 a_{LS} + 4 a_T
\end{aligned}
\qquad \text{(VI.2-8)}
$$

In the framework of all proposed potential models which successfully describe the spin ordering of the χ_c states $a_{LS} > 1.2 a_T > 0$, leading to the rule : the higher the spin the higher the mass of the P-states[1].

We can determine spin-orbit (a_{LS}) and tensor (a_T) coefficients from the data :

$$
\begin{aligned}
a_{LS} &= \frac{1}{12}(5 M_{^3P_2} - 3 M_{^3P_1} - 2 M_{^3P_0}) \\
a_T &= \frac{5}{72}(- M_{^3P_2} + 3 M_{^3P_1} - 2 M_{^3P_0})
\end{aligned}
\qquad \text{(VI.2-9)}
$$

Using results from our analysis averaged with results from parallel analysis of the inclusive photon spectrum, given by VI.1-2, and assuming the standard spin assignment, we obtain :

$$
a_{LS}(1P) = (15.3 \pm 0.6)\ \text{MeV} \qquad a_T(1P) = (2.8 \pm 0.4)\ \text{MeV}
\qquad \text{(VI.2-10)}
$$

Any energy scale error does not contribute to those quantities, thus we did not include it here. Contributions to the observed splitting of the 1P $b\bar{b}$ states are illustrated in Fig.54.

We can compare these experimental values with theoretical predictions given by Eq.VI.2-6, and calculated within the framework of the potential models. Since theoretical predictions of the magnitudes of the spin-orbit and tensor splittings are as sensitive to details of the potential model as to the underlying physics of the spin dependent forces, the relative ratio of the P-wave splittings is often used, since it is less model dependent.

$$
R_P = \frac{M_{^3P_2} - M_{^3P_1}}{M_{^3P_1} - M_{^3P_0}} = \frac{2 a_{LS} - \frac{12}{5} a_T}{a_{LS} + 6 a_T}
\qquad \text{(VI.2-11)}
$$

The result of our experiment yields : $R_P = 0.74 \pm 0.08$. The earlier CUSB experiment[15] indicated different R_P value, which was close to unity; however, the experimental uncertainty was large.

A comparison of our experimental a_{LS}, a_T, R_P values with theoretical predictions is shown in Fig.55. Clearly, models with vector confinement tend to overestimate the spin-orbit

[1] It is easy to show using VI.2-8, that $a_{LS}, a_T > 0$ implies $M_{^3P_1} > M_{^3P_0}$, and in addition $a_{LS} > 1.2 a_T$ ensures $M_{^3P_2} > M_{^3P_1}$.

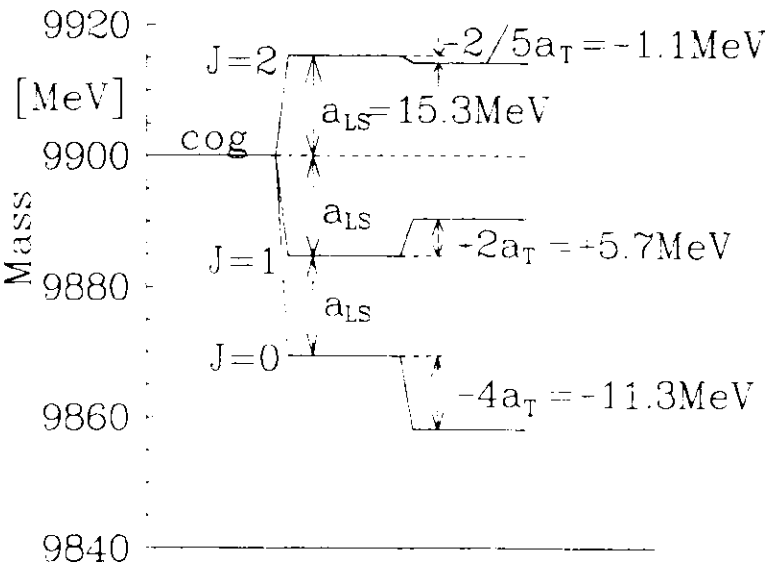

Figure 54.
The observed splitting of the $b\bar{b}$ 1P levels. The contributions from the spin-orbit and tensor forces are indicated.

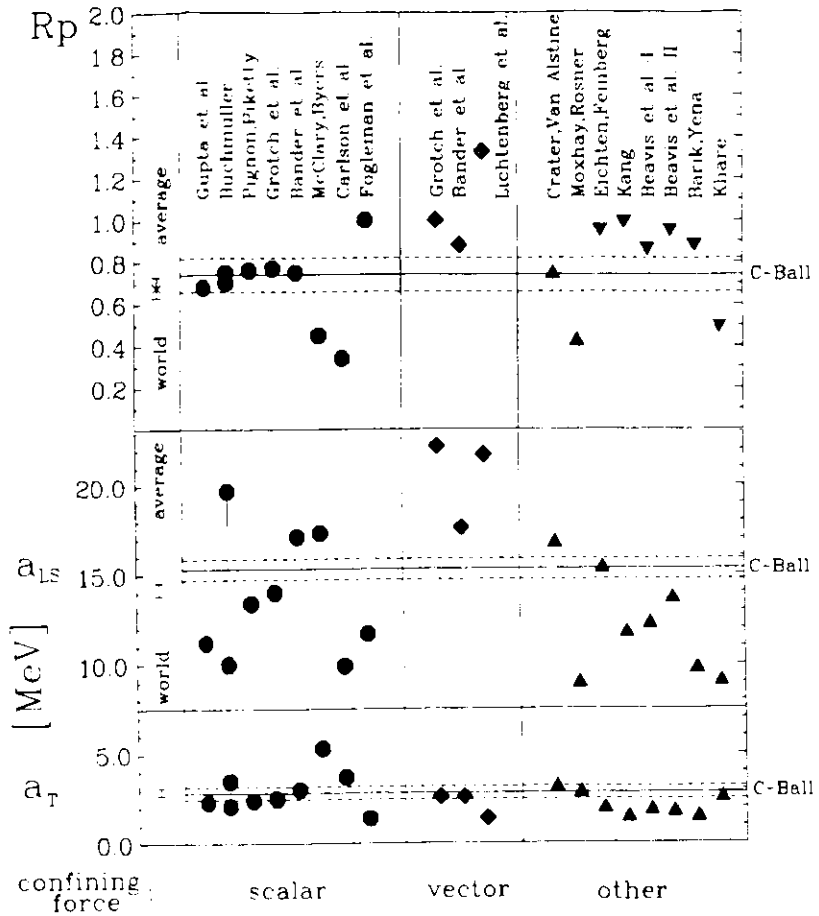

Figure 55.
The comparison between the observed fine structure of the χ_b states and the theoretical predictions by : Gupta et al. - Ref.6, Buchmüller - Ref.90, Pignon, Piketty - Ref.76, Grotch et al. - Ref.72, Bander et al. - Ref.50, McClary, Byers - Ref.46, Carlson et al. - Ref.71, Fogleman et al. - Ref.67, Lichtenberg et al. - Ref.69, Crater, Van Aletine - Ref.70, Moxhay, Rosner - Ref.45, Eichten, Feinberg - Ref.49, Kang - Ref.63, Beavis et al. I - Ref.68, II - Ref.64, Barik, Yena - Ref.78, and Khare - Ref.58. The horizontal solid lines show the Crystal Ball measurements, with errors indicated by the dashed lines. The world averaged results are also shown.

force because of the missing long range component, which is of the opposite sign as the short range contribution. This leads to too high values of R_P. Most of the models with scalar confinement predict fairly accurately the value of the ratio R_P. However, magnitudes of the absolute splittings are very much potential dependent and thus only roughly reproduced. Almost all models with other than pure scalar confinement forces do not fit to our measurement. The model of Crater and Van Alstine [70], which is the only one in this class which agrees well with the data, is very close to the scalar confinement model. It takes half of the scalar exchange and half of the exchange of time-like four-vectors.

Concluding, our measurement of the fine structure of the lowest triplet-P $b\bar{b}$ states points to the scalar nature of the confining forces. The same indication was earlier obtained from the fine splitting of the $c\bar{c}$ 1P states [92].

The confining force which is of the effective scalar type is also the most attractive theoretically. Buchmüller has drawn a simple intuitive connection between scalar potential and a string picture, which suggests that quarks are confined by purely electric color field in the rotating rest frame of quarks [90]. This was supported by more rigorous calculations of Gromes [88]. Effective scalar confinement was also suggested [93], and successfully applied [81] in numerical predictions for the χ_b fine structure, by the bag model.

VI.3. Hadronic Widths of χ_b States

Hadronic widths of the quarkonia states were one of the earliest QCD predictions. QCD describes OZI-forbidden hadronic decays of quarkonia by $Q\bar{Q}$ annihilation into the minimum allowed number of gluons. As gluons are not observable particles, the usual assumption is made that hadronization process does not affect the inclusive decay rate. It is also assumed that the decay amplitude factors into a perturbative part from the quark-antiquark annihilation process, and a nonperturbative part describing the structure of the $Q\bar{Q}$ bound state before annihilation. The latter is represented by a wave function of the quarkonium state, which is known phenomenologically from the potential models.

In the lowest order QCD calculations, self-coupling of gluons is not important, and therefore formulae for the decay widths can be obtained by analogy with the QED formulae describing positronium annihilation into photons [94]. Spin 0 and 2 P-wave states can

annihilate into two gluons (Fig.56) :

(VI.3-1)
$$\Gamma_{had}^{(0)}(^3P_{0^{++}}) = 96\,\alpha_s^2\,\frac{|\phi'_P(0)|^2}{M^4}$$
$$\Gamma_{had}^{(0)}(^3P_{2^{++}}) = \frac{128}{5}\,\alpha_s^2\,\frac{|\phi'_P(0)|^2}{M^4}$$

where :

M – *mass of the bound state,*

$\phi'_P(R)$ – *derivative of the radial wave function.*

Spin-1 particles cannot decay into two massless on-shell vector gluons. Therefore, the leading QCD graphs are third order in α_s (see Fig.57). It turns out that the $Q\bar{Q} \to gg\bar{q}$ graph dominates over ggg, because of the zero-binding-energy singularity[95]. It gives :

(VI.3-2)
$$\Gamma_{had}^{(1)}(^3P_{1^{++}}) = \frac{512}{9}\,\alpha_s^3\,\frac{|\phi'_P(0)|^2}{M^4} \times ln\frac{(2m_c)^2}{(2m_b)^2 - M^2}$$

Although such a singularity is somewhat worrisome, since it may signal the breakdown of perturbation theory[96], one may still hope to get a very rough estimate of the magnitude of $\Gamma_{had}(^3P_{1^{++}})$. The logarithm due to this infrared divergence can be parametrized[94] for numerical calculations by $ln(m_b R_c)$, where the quark mass : $m_b \simeq 4.9$ GeV, and the confining radius : $R_c \simeq \frac{1}{0.4}$ GeV^{-1}.

The first order QCD corrections to the lowest order formulae were calculated for the spin 0 and 2 χ_b states[97,94] :

(VI.3-3)
$$\Gamma_{had}^{(1)}(^3P_{2^{++}}) = \Gamma_{had}^{(0)}(^3P_{2^{++}})\left(1 - 0.3\frac{\alpha_s}{\pi}\right)$$
$$\Gamma_{had}^{(1)}(^3P_{0^{++}}) = \Gamma_{had}^{(0)}(^3P_{0^{++}})\left(1 - 9.8\frac{\alpha_s}{\pi}\right)$$

Theoretically, a ratio of the hadronic widths is more reliable, since the nonperturbative term cancels out :

$$\frac{\Gamma_{had}^{(1)}(^3P_{0^{++}})}{\Gamma_{had}^{(1)}(^3P_{2^{++}})} = \frac{15}{4}\left(1 + 0.3\frac{\alpha_s}{\pi}\right) \approx 5.6 \quad (3.75\ \textit{in the first order})$$

(VI.3-4)
$$\frac{\Gamma_{had}^{(0)}(^3P_{1^{++}})}{\Gamma_{had}^{(0)}(^3P_{2^{++}})} = \frac{20}{9\pi}\,\alpha_s\,ln(m_b R_c) \approx 0.3$$

The first ratio is renormalization scheme independent. We used here $\alpha_s = 0.165 \pm 0.005$ determined by the Mackenzie-Lepage method[98], with the latest value of $BR_{\mu\mu}(\Upsilon) = 2.8 \pm 0.3$ %[19]. Higher order corrections for the spin 0 and 2 states, and the first order correction for spin 1 state are practically impossible to calculate.

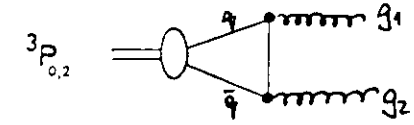

Figure 56.
The QCD graph of the spin 0 and 2 χ_b states annihilating into two gluons.

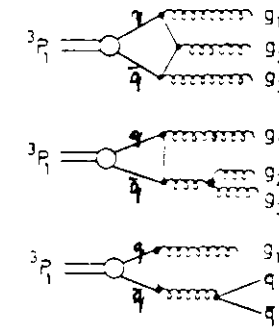

Figure 57.
The QCD graphs of the spin 1 χ_b state annihilating into gluons and quarks.

To predict absolute magnitudes of the hadronic widths, one must use potential model results for $|\phi'_P(0)|^2$. Fortunately, the value of $|\phi'_P(0)|^2$ seems rather insensitive to the details of the potential model. Krammer and Krasemann calculated [7] $|\phi'_P(0)|^2 m_b^{-3} = 0.012$ GeV^{-2}, not very much dependent on the quark mass. In fact, results from three quite different potentials given in Ref.99 are $\phi'_P(0)|^2 m_b^{-3} = 0.012, 0.013, 0.010$ GeV^{-2}. Taking the average of these and $m_b \sim 4900$ MeV, we find :

$$\Gamma^{(C)}_{had}({}^3P_{2^{++}}) \approx 102 \text{ keV} \qquad \Gamma^{(1)}_{had}({}^3P_{2^{++}}) \approx 104 \text{ keV}$$

(VI.3-5)
$$\Gamma^{(0)}_{had}({}^3P_{1^{++}}) \approx 30 \text{ keV}$$

$$\Gamma^{(0)}_{had}({}^3P_{0^{++}}) \approx 384 \text{ keV} \qquad \Gamma^{(1)}_{had}({}^3P_{0^{++}}) \approx 582 \text{ keV}$$

Uncertainties due to the assumed values of m_b, $|\phi'_P(0)|^2$ and α_s are about 20 %. The strong radiative correction to $\Gamma^{(0)}_{had}({}^3P_{0^{++}})$ is 52 % in the first order, thus the next order corrections may be large, too. The prediction for $\Gamma_{had}({}^3P_{2^{++}})$ is more reliable, since the first order QCD correction is only 2 %.

The predicted hadronic width of the spin-0 χ_b state is substantially larger than for the spin-1 and spin-2 states. Hence, the radiative decays of the spin-0 χ_b state should be relatively suppressed. This is indeed observed in our analysis.

We can obtain experimental information on the χ_b hadronic widths from the branching ratios for the radiative decays $\chi_b \to \gamma\Upsilon$. As these branching ratios cannot be directly measured in e^+e^- annihilation, one combines results on the product of the branching ratios $BR(\Upsilon' \to \gamma\chi_b) \cdot BR(\chi_b \to \gamma\Upsilon)$ measured in our exclusive analysis with branching ratios $BR(\Upsilon' \to \gamma\chi_b)$ obtained by the inclusive photon study. Note that only the exclusive cascade channel allows measurement of the product branching ratio for the individual χ_b states, since the secondary lines in the inclusive photon spectrum due to χ_b decays cannot be resolved with the presently available spectrometers. We obtain :

$$BR(\chi_b^{J=2} \to \gamma\Upsilon) = (28 \pm 6 \pm 6) \%$$

(VI.3-6)
$$BR(\chi_b^{J=1} \to \gamma\Upsilon) = (33 \pm 5 \pm 7) \%$$

$$BR(\chi_b^{J=0} \to \gamma\Upsilon) < 4.2 \% \quad (90 \% \ C.L.)$$

From our upper limits on $\Gamma_{tot}(\chi_b)$ presented in section IV.3 and values for the radiative decays of the χ_b states (BR_γ) given above, we can calculate :

(VI.3-7)
$$\Gamma_{had} = \Gamma_{tot}(1 - BR_\gamma)$$

$$\Gamma_{had}({}^3P_{2^{++}}) < 4.5 \text{ MeV} \quad (90 \% \ C.L.)$$

$$\Gamma_{had}({}^3P_{1^{++}}) < 4.6 \text{ MeV} \quad (90 \% \ C.L.)$$

Even using better upper limits on $\Gamma_{tot}(\chi_b)$ obtained by ARGUS collaboration[18], the upper limits on $\Gamma_{had}(\chi_b)$ are still much higher than the values predicted by QCD.

To get a further insight into hadronic widths of the χ_b states one must use the potential models.

The ratios of the hadronic widths can be derived in a way practically free of theoretical uncertainties :

(VI.3-8)
$$\Gamma_{had} = \Gamma_\gamma \left(\frac{1}{BR_\gamma} - 1\right)$$

$$\frac{\Gamma^a_{had}}{\Gamma^b_{had}} = \frac{\Gamma^a_\gamma}{\Gamma^b_\gamma} \frac{\left(\frac{1}{BR^a_\gamma} - 1\right)}{\left(\frac{1}{BR^b_\gamma} - 1\right)}$$

The nonrelativistic model predicts the rate of ${}^3P_{J^{++}} \to {}^3S_{1^{--}}$ transitions on the basis of the electric dipole matrix elements :

(VI.3-9)
$$\Gamma_{E1}({}^3P_J \to {}^3S_1) = \frac{4}{9} \alpha_{QED} e_Q^2 E_\gamma^3 \langle 1S | R | 1P \rangle^2$$

Differences between different spin χ_b states are only due to the different phase space factors E_γ^3. The relativistic corrections[46,45,72] to the formula VI.3-9 effect only the absolute rate of the transitions, leaving their ratio constant within 3 %. Substituting :

(VI.3-10)
$$\frac{\Gamma^a_\gamma}{\Gamma^b_\gamma} = \left(\frac{E^a_\gamma}{E^b_\gamma}\right)^3$$

we obtain, while using branching ratios given by VI.3-6 :

$$\frac{\Gamma_{had}({}^3P_{0^{++}})}{\Gamma_{had}({}^3P_{2^{++}})} > 6.1 \quad (90 \% \ C.L.)$$

(VI.3-11)
$$\frac{\Gamma_{had}({}^3P_{1^{++}})}{\Gamma_{had}({}^3P_{2^{++}})} = 0.7 \pm 0.2$$

The first result is much above the lowest order QCD prediction (see Eq.VI.3-4), so the large first order QCD correction, which goes in the right direction, is reasonable. As the experimental lower limit is slightly larger than even the first order corrected ratio, the higher order corrections are needed. The ratio of hadronic widths of the spin 1 and 2 states is twice as large as the lowest order QCD prediction, but we have not hoped for more than just qualitative agreement with the data.

Eq.VI.3-8 can be used also to get semi-experimental estimates of the absolute values of the χ_b hadronic widths, when using the potential model predictions for the radiative transition rates (Γ_γ) given by Eq.VI.3-9. Although the nonrelativistic predictions for the electric dipole transition rates failed to describe the $c\bar{c}$ data, they compare reasonably well with the experimental results for the $\Upsilon' \to \gamma\chi_b$ transitions (see Table 10). This can be understood on the basis of large relativistic corrections to the radiative transition widths in the $c\bar{c}$ system[46,45]. Theoretical predictions of the nonrelativistic potential models for the radiative transition rates $\chi_b \to \gamma\Upsilon$ are listed in Table 10. The predicted rates of the $\Upsilon' \to \gamma\chi_b$ transitions are also compared there to the data. Average values of the predicted transition rates are calculated. The spread of the theoretical values is at about 25 %. Further uncertainity is introduced by relativistic corrections. There is no quantitative agreement between different authors[45,46,72] in the magnitude of those corrections. Relativistic corrections by Grotch et al.[72] seem to be overestimated ($\sim$ 20 %). The $1P \xrightarrow{\gamma} 1S$ transitions are free of the "node" problem discussed by McClary and Byers[46] , therefore large relativistic corrections are not expected. We add in quadrature an additional 10 % uncertainty in the mean value of the nonrelativistic predictions for $\Gamma_{E1}(\chi_b \to \gamma\Upsilon)$ due to the relativistic effects in accord with Ref.46,45 :

$$\begin{aligned} \Gamma_\gamma^{theor.}(\chi_b^{J=2} \to \gamma\Upsilon) &= (40 \pm 12)\ \text{keV} \\ \Gamma_\gamma^{theor.}(\chi_b^{J=1} \to \gamma\Upsilon) &= (34 \pm 10)\ \text{keV} \\ \Gamma_\gamma^{theor.}(\chi_b^{J=0} \to \gamma\Upsilon) &= (27 \pm 9)\ \text{keV} \end{aligned} \qquad \text{(VI.3-12)}$$

Other theoretical systematic uncertainties are small. Coupled channel effects do not alter these predictions[66] by more than 1.5 %. Unless the anomalous magnetic moment of quarks is very large, it does not effect these transition rates, either[72]. Using average values of the theoretical predictions for Γ_γ given by VI.3-12, and experimental branching ratios

$BR(\chi_b \to \gamma\Upsilon)$ given by VI.3-6, we derive :

$$\begin{aligned} \Gamma_{had}(^3P_{2^{++}}) &\quad (101 \pm 41)\ \text{keV} \\ \Gamma_{had}(^3P_{1^{++}}) &= (\ 69 \pm 28)\ \text{keV} \\ \Gamma_{had}(^3P_{0^{++}}) &> 616\ \text{keV} \quad (90\ \%\ C.L.) \end{aligned} \qquad \text{(VI.3-13)}$$

The errors include experimental and thoeretical uncertainties, as discussed above, added in quadrature.

Although the error is large, the value of $\Gamma_{had}(^3P_{2^{++}})$ agrees surprisingly well with the QCD prediction (VI.3-5). The QCD prediction for $\Gamma_{had}(^3P_{1^{++}})$ is twice as small as the experimentally derived one. They agree, however, within large errors. The derived lower limit on the hadronic width of the spin-0 χ_b state is slightly larger than the QCD predicted one. It supports the large first order QCD correction to this width.

The approximate agreement between the hadronic widths of the χ_b states derived from the data with help of the potential models, and the QCD predictions is remarkable. For the $c\bar{c}$ system, only the ratios of the hadronic widths of the χ_c states agreed with the QCD expectations. Absolute values of the QCD predictions for $\Gamma_{had}(\chi_c)$ were an order of magnitude too small[99]. The Υ system again proved more suitable for tests of theory.

Table 10. Predictions of nonrelativistic potential models for the radiative transition rates $\Upsilon' \to \gamma\chi_b$ and $\chi_b \to \gamma\Upsilon$. All values were corrected to the line energies measured in our experiment.

Author(s)	$\Gamma_{E1}(2^3S_1 \to 1^3P_J)$ [keV]			$\Gamma_{E1}(1^3P_J \to 1^3S_1)$ [keV]		
	J= 2	J= 1	J= 0	J= 2	J= 1	J= 0
Pignon,Piketty[76]	1.7	1.9	1.2	40.9	34.8	27.5
Eichten et al.[74]	2.1	2.3	1.5	29.4	25.0	19.8
Celmaster et al.[65]	1.8	2.0	1.3	33.8	28.8	22.8
Kang[63]	2.5	2.3	1.4	46.2	41.7	32.4
Ono,Törnqvist[66]	2.5	2.7	1.7	30.2	25.8	20.5
Quigg,Rosner-$c\bar{c}$[53]	2.4	2.6	1.6	38.5	32.8	26.0
Quigg,Rosner-$b\bar{b}$[53]	2.0	2.2	1.4	44.6	38.0	30.0
Buchmüller,Tye[9]	2.2	2.4	1.6	43.3	36.8	29.1
Gupta et al.[100]	2.2	2.4	1.5	46.8	40.0	31.6
†McClary,Byers[46]	2.2	2.3	1.5	31.4	26.7	21.2
†Moxhay,Rosner[45]	2.1	2.2	1.4	39.5	33.6	27.4
†Grotch et al.[72]	2.1	2.3	1.4	44.8	38.1	30.1
Martin [57,99]				46.3	39.4	31.2
Olsson et al.[99]				38.5	32.8	25.9
Hagiwara et al.[101,99]				46.3	39.4	31.2
‡AVERAGE	2.1 ± 0.4	2.3 ± 0.4	1.4 ± 0.2	40.0^{+6}_{-10}	34.0^{+8}_{-9}	27.0^{+5}_{-7}
*Crystal Ball[31]	1.7 ± 0.5	2.0 ± 0.5	1.1 ± 0.4			

†nonrelativistic values are taken from the work, which also develops radiative corrections.
‡errors cover the minimal and the maximal theoretical predictions.
*We used $\Gamma_{tot}(\Upsilon') = (30 \pm 5)$ keV[19] to derive Γ_γ from BR_γ.

VII. CONCLUSIONS

We have observed the radiative cascade transitions $\Upsilon' \to \gamma\chi_b \to \gamma\gamma\Upsilon$ in the exclusive sample of $\gamma\gamma\mu^+\mu^-$ and $\gamma\gamma e^+e^-$ events recorded with the Crystal Ball detector at the e^+e^- storage ring DORIS-II. Two χ_b states are observed, with masses (9915.1 ± 1.5) MeV and (9890.1 ± 1.4) MeV. The cascade branching ratios, $BR(\Upsilon' \to \gamma\chi_b \to \gamma\gamma\Upsilon)$, are measured to be $(1.6 \pm 0.3 \pm 0.2)$ % and $(2.1 \pm 0.3 \pm 0.3)$ % correspondingly. The masses and transition rates are in good agreement with the earlier CUSB[16] results, however the experimental errors have been improved, mainly due to the higher statistics. The χ_b masses also agree well with those measured in inclusive photon analysis by our experiment[31] and other detectors[15,17,18]. As expected, cascade transitions via the lowest mass χ_b state, which was detected in the inclusive analyses, are not observed. An upper limit of $BR(\Upsilon' \to \gamma\chi_b \to \gamma\gamma\Upsilon) < 0.15$ at 90 % *C.L.* is obtained.

We have investigated, for the first time, spins of the two observed χ_b states by analysis of the angular correlations among the final state particles in the cascade reaction. Spin 0 assignment is ruled out with high confidence for both states. Assuming pure dipole photon transitions we can also exclude at 99.4 % *C.L.* the global spin assignment : J=1 for the highest mass χ_b state and J=2 for the next highest one. Thus, the results strongly support the χ_b spins predicted by the potential models of $b\bar{b}$ quarkonia. The angular distributions are consistent with photon transitions of pure dipole character. Some multipole combinations can be excluded; however, stringent limits on possible admixture of quadrupole transitions have not been obtained because of the limited statistics.

Combining our results on the χ_b masses with results from the inclusive photon analysis, we improve the accuracy of the Crystal Ball determination of the center-of-gravity mass and of the fine structure of the χ_b states. One obtains $M_{cog}(\chi_b) = (9900.1 \pm 0.9)$ MeV and $R_P = (M_{J=2} - M_{J=1})/(M_{J=1} - M_{J=0}) = 0.74 \pm 0.08$.

The center-of-gravity mass of the χ_b states imposes new constraints on the potential models. It is in good agreement with most of the predictions of the QCD motivated models, and it disagrees with the prediction of Martin's potential. The QCD sum rules significantly underestimate the χ_b masses whereas, the bag model overestimates them.

The splitting of the χ_b states seems to indicate that the confining forces between quarks are of the effective scalar nature.

The branching ratios of $\chi_b \to \gamma\Upsilon$, $(28 \pm 6 \pm 6)$ % for the spin 2 state, $(33 \pm 5 \pm 7)$ % for the spin 1 state and < 4.2 % at 90 % *C.L.* for the spin 0 χ_b state, have been obtained by combining our exclusive results for $BR(\Upsilon' \to \gamma\chi_b) \cdot BR(\chi_b \to \gamma\Upsilon)$ with the inclusive results for $BR(\Upsilon' \to \gamma\chi_b)$. They are used to derive the hadronic widths of the χ_b states, with help of the predictions of the potential models for $\Gamma(\chi_b \to \gamma\Upsilon)$, yielding $\Gamma_{had}(\chi_b^{J=2}) \simeq 100$ keV, $\Gamma_{had}(\chi_b^{J=1}) \simeq 70$ keV and $\Gamma_{had}(\chi_b^{J=0}) \gtrsim 620$ keV at 90 % *C.L.* The derived hadronic widths of the χ_b states agree with the QCD predictions within experimental and theoretical uncertainties.

APPENDIX A. Bump Algorithm

We developed a new bump algorithm to improve sensitivity for particles overlapping within one connected region. Following the idea of the local energy maxima, our algorithm looks for crystals which have no neighbour in the next two layers of the crystals ("the group of 13"- see Fig.12) , with energy greater than the bump candidate itself. The crystal with the maximum energy in the connected region satisfies, of course, this condition. It becomes the primary bump module. All other crystals in the same connected region are inspected as a candidate for a secondary bump. Shower fluctuations may sometimes create two local energy maxima. In this case, the maximum corresponding to the particle direction is much stronger than the other one. Monte Carlo studies based on the Electron-Gamma Simulation program[33] show that, if we had applied only the criterion of energy maximum, we would have found two bumps from a single incident photon with a frequency of 0.15-1.5 % for photons in the energy range 50-5000 MeV. To suppress this effect, we require that a secondary bump ("i") cannot be both (at the same time) :

- close to the other, already recognized bump ("j"), in the same connected region :

(A-1) $$\cos\psi_{ij} > a_0 - a_1\,(E13_j - 100\ \text{MeV})$$
$$a_0 = 0.91 \qquad a_1 = 0.000175$$

- low energy in comparison with the nearby bump :

(A-2) $$E1_i < b_0 + b_1\,[ln(E13_j) \quad ln(25\ \text{MeV})]$$
$$b_0 = 25\ \text{MeV} \quad b_1 = 3.77$$

where :

ψ_{ij} – *angle between the crystal centers,*

$E13_j$ – *energy sum of 13 crystals around the bump module "j",*

$E1_i$ – *energy in the module "i".*

The discrimination conditions were developed by the Monte Carlo studies, as demonstrated in Fig.58,59. Using this bump discrimination, shower fluctuations can create more than one bump in the same connected region in less than 0.1 % of all electromagnetic showers. Actually, an effect of two separate connected regions from a single showering particle (electromagnetic "split-off") will be more often[1] , ~1-4 %.

[1] We did not attempt to remove electromagnetic split-off's in our analysis. The bump discrimination algorithm was not applied to bumps in two different connected regions.

Of course, overlapping particles may sometimes leave only one energy maximum. The critical overlap angle will depend on the types and energies of the involved particles. In this case, elimination of the multiparticle connected regions is a matter of the pattern cuts on the lateral energy distribution.

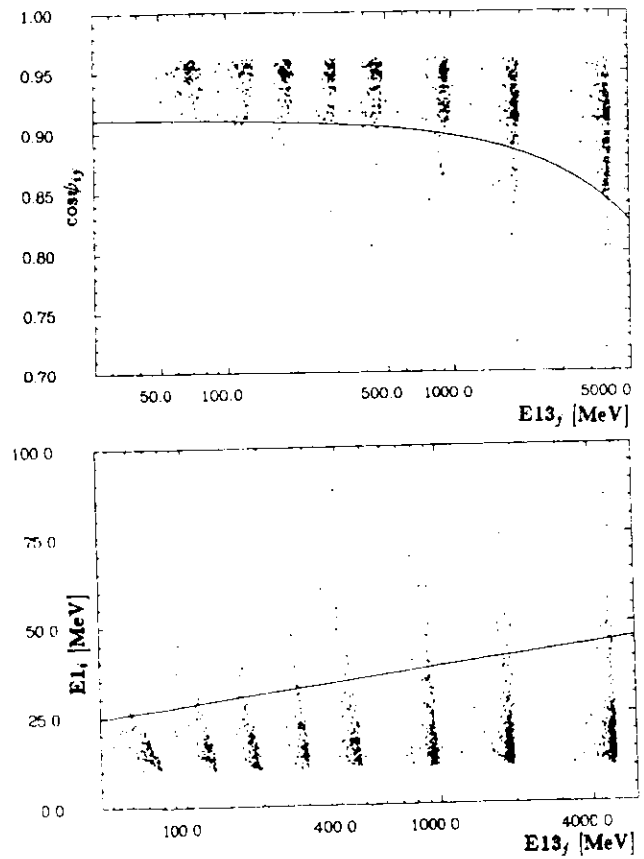

Figure 58,59.
The cuts to suppress a secondary bump due to the shower fluctuation. The points represent Monte Carlo generated electromagnetic showers, with different energies, which had the secondary energy maximum in one connected region. The solid lines show the discrimination conditions, as described in the text.

APPENDIX B. Crystal Ball Energy Algorithm

We will describe here the standard Crystal Ball energy algorithm. The group of 13 crystals with the bump module in the central position (Fig.12) serves for an energy measurement of the incident photon or electron. On average, ϵ=97.8 % of the electromagnetic shower is enclosed in it, independent of the particle energy. In addition, some energy may be lost in small gaps between the crystals. This kind of energy loss is larger for showers developing near the crystal vertex, compared to those near the crystal center. Thus it must be associated with a smaller fraction of the energy deposited in the bump module. An empirical correction function was developed to account for this energy leakage, using the ratio E1/E13 as a measure of the shower position. Electron showers from Bhabha scattering events showed that, to a good approximation, the correction function should be linear :

$$\frac{E13}{E_{beam}} = \epsilon \cdot \left(a + b \cdot \frac{E1}{E13} \right) \qquad \text{(B-1)}$$

$$a = 0.898 \qquad b = 0.125$$

Applying this correction improves the resolution for Bhabha electrons by ~30 %. The improvement is smaller for less energetic showers, since increased shower fluctuations upset the shower position measurement by the E1/E13 ratio.

The absolute energy scale is initially set, over the whole energy range, by the calibration with ~5 GeV Bhabha electrons. Therefore, even small nonlinearities in the energy detection system may lead to measurable energy distortion at lower energies. In fact, studies of the $\Upsilon' \to \pi^0\pi^0\Upsilon$ transitions in the exclusive channel with $\gamma\gamma\gamma\gamma e^+e^-$ and $\gamma\gamma\gamma\gamma\mu^+\mu^-$ events showed that both the π^0 mass and the $M_{\Upsilon'} - M_\Upsilon$ mass difference came out too low in comparison with the PDG values[19]. The formula :

$$E_{corr} = \frac{E}{1 + \alpha \cdot ln(\frac{E}{E_{beam}})} \qquad \text{(B-2)}$$

was applied to remove this distortion[102]. The choice of the correction was motivated by the observation that most of the shower features scaled logarithmically with the energy, and the requirement that the correction had to vanish for the beam energy. A value of α = 0.0137 very well reproduced the mass difference $M_{\Upsilon'} - M_\Upsilon$ and the π^0 mass observed in the $\Upsilon' \to \pi^0\pi^0\Upsilon, \Upsilon \to l^+l^-$ channel.

Summarizing, the energy of the showering particle was calculated with the following formula :

$$E = \frac{E'}{1 + \alpha \cdot ln(\frac{E'}{E_{beam}})} \qquad E' = \frac{E13}{\epsilon \cdot (a + b \cdot \frac{E1}{E13})} \qquad E13 = \sum_{i=1}^{13} E_i \tag{B-3}$$

$$\alpha = 0.0137 \qquad \epsilon = 0.978 \qquad a = 0.898 \quad b = 0.125$$

APPENDIX C. Muon Identification

Some muon identification cuts have been used in the selection of $\gamma\gamma\mu^+\mu^-$ events (section III.4) and in the beam polarization measurement with $\mu^+\mu^-$ events (Appendix G). Here, we describe how those cuts have been worked out.

A high momentum muon is the only charged particle which can pass even a very thick layer of matter. Usually, iron shielding against the other particles is used to recognize a muon. The Crystal Ball experiment lacks this kind of muon identification system. Only if hadrons interact in the NaI crystals, they can possibly be distinguished from muons. Thus, patterns of muon energy deposition in the Crystal Ball detector must be studied. A good source of high momenta muons is provided by e^+e^- annihilation into $\mu^+\mu^-$ pairs. Each muon should carry out the beam energy (~5 GeV). Cosmic rays are another source of muons, however momenta of the cosmic muons vary over a wide range (with mean value of 2 GeV).

Selection of μ-pair events had to be done without any cuts on the energy patterns (as we just wanted to study them). Nevertheless, a clean sample of muons was obtained thanks to unique topological features of the $\mu^+\mu^-$ events and NaI-independent information from the ToF scintillation counters. We selected events with exactly two bumps in the central part of the detector. They had to be back-to-back within 9°. The energies of both energy clusters were selected in the 100-400 MeV range. The energy in the End Caps and excess energy (see section III.4) were not allowed to exceed 25 MeV. Exactly one ToF counter, matching the direction of the upper energy cluster, had to fire. The angle between the bump module direction and the edge of the counter had to be less than 11°. The hit position along the counter expected from the track direction had to agree within ±30 cm with the hit position measured by pulse height ratio and time difference at the two ends of the counter[1]. The pulse height in the ToF counters had to be consistent with a minimum ionizing particle (Fig.60).

The remaining events consisted of annihilation muon pairs and cosmic muons traversing the ball radially. They differed only in timing. Annihilation events were correlated to the beam crossing time, whereas cosmic ray events were not. Therefore, the time of the energy deposition in the NaI crystals peaked at certain value (zero in our convention) for the annihilation events. The cosmic ray events produced a flat time distribution. All "out of time"

[1] The software and calibration of the ToF counters developed by the author differ from the standard programs which use somewhat simplified algorithms.

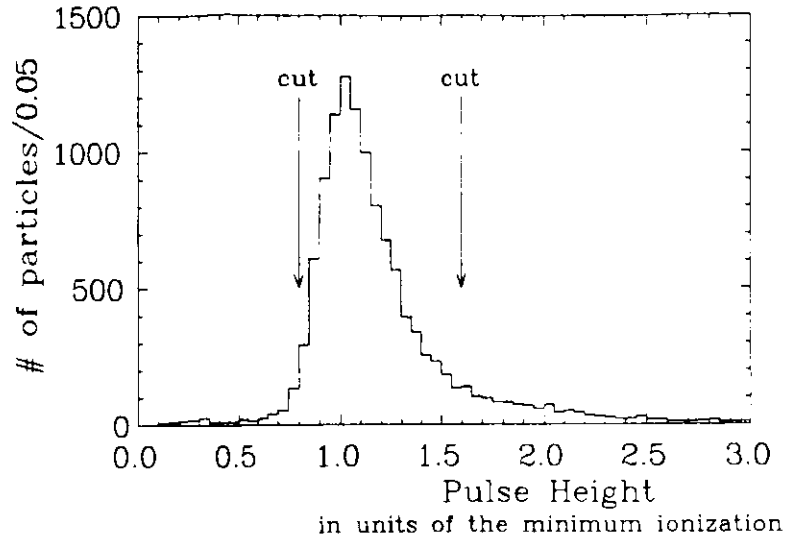

Figure 60.
The pulse height distribution in the ToF counters for the preselected $e^+e^- \to \mu^+\mu^-$ events. The cuts are indicated.

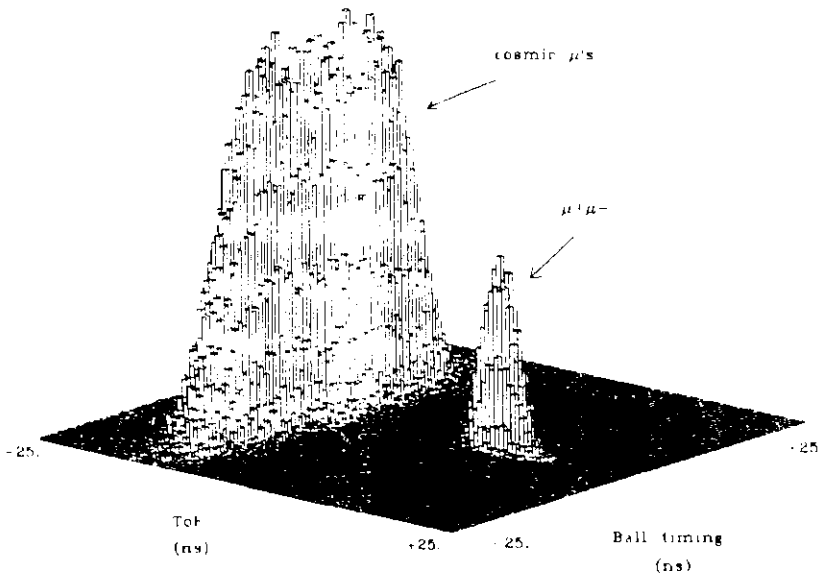

Figure 61.
The separation of cosmic rays from $e^+e^- \to \mu^+\mu^-$ events by the time analysis.
Time of the energy deposition in the NaI crystals ("ball timing") peaks for the annihilation events at the beam crossing time. Time difference between the signal in the ToF counters and the calorimeter ("ToF") measures the direction of flight of the muon, and allows complete separation of cosmic and annihilation muons.

cosmic muons could be eliminated. Furthermore, cosmic muons had opposite direction of flight in the upper hemisphere compared to the $\mu^+\mu^-$ events. Complete separation of the annihilation and cosmic signals was possible measuring the time of flight of the muon between the ToF counters and the NaI crystals. The timing separation between annihilation and cosmic muons is illustrated in Fig.61.

The distribution of energy left by annihilation muons in the group of 13 crystals around the bump module is shown in Fig.62. The cosmic muons exhibit almost the same energy distribution. The distributions peak at the expected value for minimum ionizing particles : ~206 MeV. They have an asymmetric tail towards the higher energies, due to the production of δ-rays. The solid line represents the fit to the data of the Landau distribution[103] smeared with the detector resolution. It turned out that an energy resolution twice as large as for showering particles was needed to obtain a satisfactory fit. From the fitted curve we estimated that the $150 \leq E13_\mu \leq 310$ MeV cut used in the selection of $\gamma\gamma\mu^+\mu^-$ events was (90.8 ± 0.8) % efficient (per muon).

Different ratios of the crystal energies are usually used to describe the shape of the lateral energy distribution in the Crystal Ball detector. Using our muon sample we could tune selection efficiency of the pattern cuts for muons. Four pattern ratios were investigated : E1/E4, E4/E13, E2/E4, E2/E13. E1 denotes energy in the bump module. E2 is the sum of E1 and the second energetic module in the group of 13. E4 and E13 are the energy sums in the group of 4 and in the group of 13, respectively. Muon selection efficiency for cuts on these pattern ratios at different values are displayed in Fig.63. Almost identical curves were obtained with the cosmic sample, except for E1/E4 ratio, which is the most sensitive for track displacement from the ball origin. This indicates that the lateral energy distribution is not crucially dependent on muon energy, as is expected in the minimum ionization regime.

The vast majority of the energy deposited in only two crystals is the most characteristic feature of energy patterns from muons. Thus, our pattern cuts used in the selection of $\gamma\gamma\mu^+\mu^-$ events and the beam polarization measurement were based on E2/E13 and E2/E4 ratios.

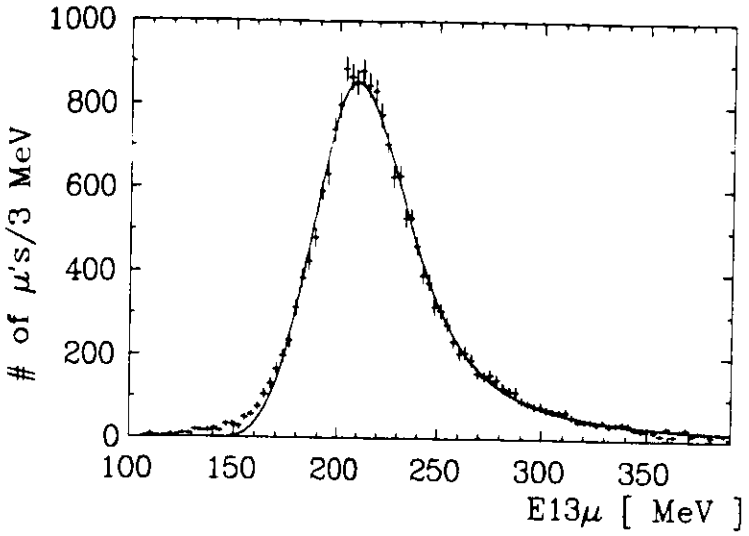

Figure 62.
The energy deposition by muons from $e^+e^- \to \mu^+\mu^-$ events. The fit of the Landau distribution smeared with the detector energy resolution is also shown.

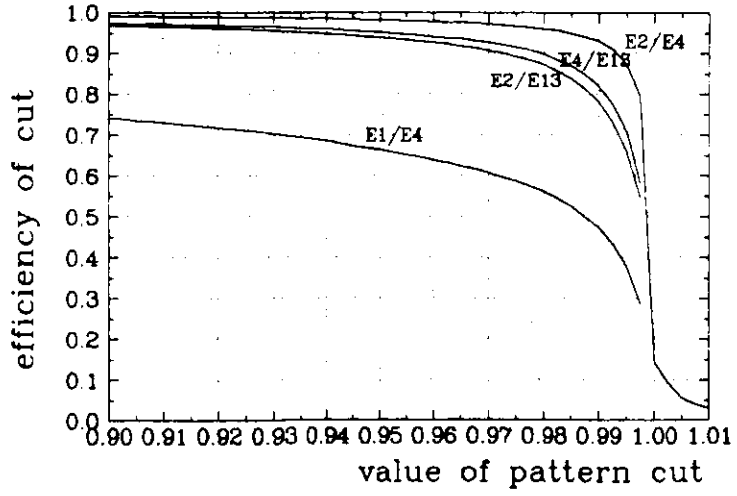

Figure 63.
The efficiencies of the pattern cuts on lateral energy distribution by muons, studied with $e^+e^- \to \mu^+\mu^-$ events.

APPENDIX D. Kinematic Fitting

In the kinematic fit, the particle four-momenta from $\gamma\gamma l^+l^-$ candidate events were varied around the measured values to satisfy the four-momentum conservation principle. If it was not possible to achieve an agreement with the conservation law, within known experimental errors, the event was rejected. This was checked by means of the chi-square of the fit. Each measured kinematic quantity Q contributed a term $\left(\frac{Q_f - Q_m}{\sigma_Q}\right)^2$ to the chi-square, where Q_m denotes the measured value, Q_f denotes the fitted value satisfying the conservation law and σ_Q is the experimental error. The particle masses being known, the full kinematic configuration of the $\gamma\gamma l^+l^-$ events was described by $4 \times 3 = 12$ quantities (e.g. energies of the particles : E, and their directions : θ, φ). The four-momentum conservation law imposed 4 constraints on them (4C fit). As the muon energies were not measured, the fit to $\gamma\gamma\mu^+\mu^-$ events was less constrained (2C fit).

Now, we will discuss the experimental errors (σ_Q) used in the fit. The Crystal Ball design relates the resolution in the azimuthal and polar angles of the particle :

$$\sigma_\varphi = \frac{\sigma_\theta}{\sin\theta} \tag{D-1}$$

The direction resolution was studied with the Monte Carlo simulation (see also Appendix C). It is energy dependent for the showering particles :

$$\sigma_\theta = \begin{cases} a_0 \cdot a_1 \cdot \ln(E_\gamma / 10\ \text{MeV}) & \text{for } E_\gamma < 1500\ \text{MeV} \\ a_2 & \text{for } E_\gamma \geq 1500\ \text{MeV} \end{cases} \tag{D-2}$$

$$(a_0 = 0.061\ \text{rad},\ a_1 = 0.0097,\ a_2 = 0.0124\ \text{rad})$$

For the bump module direction method used for muons, $\sigma_\theta \approx 0.060$ rad. Additional degradation of 0.033 rad (should be added in quadrature) was observed in θ, if the interaction point was assumed to coincide with the center of the ball. Unfortunately, this deterioration of the polar angles due to the shift of the interaction point from the ball origin was correlated among all final state particles. Such correlations were difficult to incorporate into the kinematic fitting procedure. To avoid this problem, a vertex position along the beam direction was fitted. The measured value of the vertex position was assumed to be at the ball center. The error was assumed to be 1.5 cm (see section II.1). Fitting of Monte Carlo events showed that the vertex fit worked well only in the $\gamma\gamma e^+e^-$ channel. Unmeasured muon energies plus

crude estimation of the muon directions made the fit to $\gamma\gamma\mu^+\mu^-$ events insensitive to the exact position of the interaction point. Thus, the vertex fit was abandoned in this channel. In addition, it turned out that the angular resolution of muons used in the fit had to be smaller than 0.060 rad. This was an effect of the ball granularity, introduced in the fit by the bump module direction estimate for muons. The acollinearity angle between the muons was the crucial quantity in the kinematic fit to the $\gamma\gamma\mu^+\mu^-$ events. The estimates of the muon directions did not fluctuate independently, because of the back-to-back muon topology and the back-to-back crystal geometry. This made the effective resolution in the acollinearity angle smaller than calculated under independent fluctuations assumption. In fact, for exactly back-to-back muons originating exactly from the ball center the measured acollinearity angle would be always exactly zero, resulting in "zero-resolution" effect. An effective value of 0.053 rad for the muon angular resolution was used in the fit to the $\gamma\gamma\mu^+\mu^-$ events.

The kinematic fitting was performed with the use of the iterative program SQUAW[104]. The standard Crystal Ball implementation of this program by Frank Porter was modified to fit the vertex position for $\gamma\gamma e^+e^-$ events and to include non-standard resolution settings. Special treatment of the electron/photon energies in the fit turned out to be necessary. The basic concept of the kinematic fitting by SQUAW, or any other library program, assumes normally distributed experimental errors. As discussed in Appendix E, the NaI energy response function has a non-gaussian asymmetric tail towards low energies. If we had assumed gaussian energy errors we would have lost many good events in the highly constrained $\gamma\gamma e^+e^-$ channel. The problem could be avoided by reducing number of constraints; for example, by ignoring measured electron energies. However, a more elegant solution was developed. After every iterative step of the kinematic fit, the effective energy resolution was calculated and used in the next step. For given $E_f - E_m > 0$, a value σ_E was calculated from the equation :

$$2\int_{-\infty}^{E_m}\frac{1}{\sqrt{2\pi}\sigma_E}\exp\left[-\frac{1}{2}\left(\frac{E-E_f}{\sigma_E}\right)^2\right]dE = \frac{\int_{-\infty}^{E_m} f(E|E_f)\,dE}{\int_{-\infty}^{E_f} f(E|E_f)\,dE} \qquad \text{(D-3)}$$

where $f(E|E_f)$ represents the NaI line shape function (Eq.E-1). For $E_f - E_m < 0$ the experimental errors were gaussian. In this way the confidence level of the fit was calculated properly. However, it was not known a priori that the iterative fitting procedure designed for gaussian errors would converge to the right solution while using varying effective energy resolution. This was tested on $\gamma\gamma e^+e^-$ Monte Carlo events and worked well.

APPENDIX E. Fit of Photon Transitions

Two monoenergetic photon lines and a flat background were fitted to the energy spectrum of the lower energy photons from the selected $\gamma\gamma l^+l^-$ events (see Fig.29) to obtain amplitudes and energies of the observed cascade transitions.

The detector response function for a monoenergetic source of photons is not gaussian, and it was investigated in detail in the past [10,105]. It is well described by the formula :

(E-1)

$$f(E|E^*,\sigma_{E^*},\alpha,n) = \begin{cases} A\cdot\exp\left[-\frac{1}{2}\left(\frac{E^*-E}{\sigma_{E^*}}\right)^2\right] & \text{for } E > E^* - \alpha\cdot\sigma_{E^*} \\ A\cdot\frac{\left(\frac{n}{\alpha}\right)^n e^{-\frac{1}{2}\alpha^2}}{\left(\frac{E^*-E}{\sigma_{E^*}} + \frac{n}{\alpha} - \alpha\right)^n} & \text{for } E \le E^* - \alpha\cdot\sigma_{E^*} \\ \text{where } A^{-1} = \sigma_{E^*}\cdot\left[\frac{n}{\alpha}\cdot\frac{1}{n-1}e^{-\frac{1}{2}\alpha^2} + \sqrt{\frac{\pi}{2}}\left(1+\operatorname{erf}\left(\frac{\alpha}{\sqrt{2}}\right)\right)\right] \end{cases}$$

where :

E – *measured energy,*

E^* – *true photon energy,*

σ_{E^*} – *energy resolution.*

The parameters α and n were most precisely determined by the study of the distribution of the η mass in the reaction $\psi' \to \eta\psi, \psi \to l^+l^-$ (Ref.105) :

$$\alpha = 1.07 \pm 0.04$$

$$n = 3.7 \pm 0.7 \ .$$

The energy resolution was assumed to vary with energy like :

$$\sigma_{E^*} = \sigma_c\cdot\sqrt[4]{(E^*)^3} \qquad E^* \text{ in GeV}$$

$$\sigma_c = 0.0279 \pm 0.0028 \quad .$$

The problem of energy resolution is discussed in Appendix F. It was determined with the inclusive π° signal in hadronic events. The results for Bhabha electrons give a similar value.

To use most efficiently the information from our data sample, a maximum likelihood fit to the unbinned data was applied. To get correct statistical errors from the fit procedure, the

overall normalization of the fitted energy distribution was left free (the extended likelihood method) :

$$\mathcal{L}(A_\alpha, E_\alpha, A_\beta, E_\beta, B) = \underbrace{\frac{(A_\alpha + A_\beta + B)^N}{N!} \cdot \exp|-(A_\alpha + A_\beta + B)|}_{\text{Probability of observing } N \text{ events, when } A_\alpha + A_\beta + B \text{ are expected.}} \times$$

$$\text{(E-2)} \qquad \times \prod_{i=1}^{N} \underbrace{\frac{A_\alpha \cdot f(\mathrm{E_i}|E_\alpha) + A_\beta \cdot f(\mathrm{E_i}|E_\beta) + \frac{B}{\Delta \mathrm{E}}}{A_\alpha + A_\beta + B}}_{\text{Probability of observing an event with energy } E_i.}$$

$$= \exp|-(A_\alpha + A_\beta + B)| \frac{1}{N!} \prod_{i=1}^{N} \left(A_\alpha \cdot f(\mathrm{E_i}|E_\alpha) + A_\beta \cdot f(\mathrm{E_i}|E_\beta) + \frac{B}{\Delta \mathrm{E}} \right)$$

where :

A_α, A_β – *number of observed events in each line,*

E_α, E_β – *energies of the lines,*

$f(\mathrm{E}|E_k)$ – *the line shape function (formula E-1),*

B – *number of background events in the fit region* ΔE,

N – *number of fitted events.*

A minimization of $-ln\mathcal{L}$ was performed with the MINUIT program[106]. The errors were calculated exactly, by solving numerically the following equation :

$$\text{(E-3)} \qquad \frac{\left| \int_{\hat{x}}^{\hat{x} \pm \Delta_\pm(\hat{x})} \tilde{\mathcal{L}}(x)\,\mathrm{d}x \right|}{\int_{-\infty}^{+\infty} \tilde{\mathcal{L}}(x)\,\mathrm{d}x} = 0.3413 = \begin{cases} \text{probabilty of a } 1\sigma \text{ deviation} \\ \text{for a gaussian distribution} \end{cases}$$

where :

x – *a fitted quantity,*

$\hat{x}$ – *the fitted value of* 'x',

$\Delta_\pm(\hat{x})$ – *the positive and the negative fit errors on* 'x',

$\tilde{\mathcal{L}}(x)$ – *the maximized lihelihood in respect to all other parameters except for the fixed* 'x'.

The confidence level of the fit was calculated by the Monte Carlo method[1]. The line shape parameters $\sigma_\circ, \alpha, n$ were fixed in the fit at values given above. The uncertainty in these

[1] See for example Ref.41 p.271.

parameters was added to the systematic error on the line energies and the branching ratios by calculating a contribution :

$$\text{(E-4)} \qquad \Delta^2_{sys.}(\hat{x}) = \int \mathrm{d}\sigma_\circ \int \mathrm{d}\alpha \int \mathrm{d}n \quad |\hat{x}(\sigma_\circ, \alpha, n) - \hat{x}(\widetilde{\sigma_\circ}, \widetilde{\alpha}, \widetilde{n})|^2 \times$$

$$\times \frac{1}{\sqrt{2\pi}\Delta\widetilde{\sigma_\circ}} e^{-\frac{1}{2}\left(\frac{\sigma_\circ - \widetilde{\sigma_\circ}}{\Delta\widetilde{\sigma_\circ}}\right)^2} \times \frac{1}{\sqrt{2\pi}\Delta\widetilde{\alpha}} e^{-\frac{1}{2}\left(\frac{\sigma_\circ - \widetilde{\alpha}}{\Delta\widetilde{\alpha}}\right)^2} \times \frac{1}{\sqrt{2\pi}\Delta\widetilde{n}} e^{-\frac{1}{2}\left(\frac{\sigma_\circ - \widetilde{n}}{\Delta\widetilde{n}}\right)^2}$$

where :

$\hat{x}(\sigma_\circ, \alpha, n)$ – *a result of the fit for given values of the line shape parameters,*

$\widetilde{\sigma_\circ}, \widetilde{\alpha}, \widetilde{n}$ – *the values of the line shape parameters used in the basic fit to the spectrum,*

$\Delta\widetilde{\sigma_\circ}, \Delta\widetilde{\alpha}, \Delta\widetilde{n}$ – *the errors on the above parameters.*

The fit is displayed in Fig.30 and results are summarized in Table 1.

To obtain upper limits of the natural widths (Γ) of the χ_b^α and χ_b^β states, the detector response function $f(\mathrm{E}|E^*)$ (defined by Eq.E-1) must be smeared with the Breit-Wigner distribution[1] :

$$\text{(E-5)} \qquad \underset{BW}{f}(\mathrm{E}|E^*, \Gamma^*) = \int \mathrm{dE}' \quad \frac{1}{\pi} \cdot \frac{1}{(E' - E^*)^2 + (\Gamma^*/2)^2} \times f(\mathrm{E}|\mathrm{E}')$$

The corresponding likelihood function (formula E-2) depends now on the widths of the χ_b^α and χ_b^β states : $\mathcal{L}(A_\alpha, E_\alpha, \underline{\Gamma_\alpha}, A_\beta, E_\beta, \underline{\Gamma_\beta}, B)$. The likelihood function was maximized in respect to all parameters except for the investgated χ_b width :

$$\text{(E-6)} \qquad e.g. \qquad \tilde{\mathcal{L}}(\Gamma_\alpha) = \max_{A_\alpha E_\alpha A_\beta E_\beta \Gamma_\beta B} \mathcal{L}(A_\alpha, E_\alpha, \Gamma_\alpha, A_\beta, E_\beta, \Gamma_\beta, B) \quad .$$

The 90 % upper limits were obtained by solving numerically the equation :

$$\text{(E-7)} \qquad \frac{\int_0^{\Gamma^{up.\,lim.}} \tilde{\mathcal{L}}(\Gamma)\,\mathrm{d}\Gamma}{\int_0^{\infty} \tilde{\mathcal{L}}(\Gamma)\,\mathrm{d}\Gamma} = 0.90 \quad .$$

The results are given in section IV.3.

Finally, to obtain an upper limit on the number of the observed cascade transitions via the third χ_b^7 state, the third line was put into the fit at the position determined by our

[1] The nonrelativistic formula for the Breit-Wigner distribution is sufficient in our case.

inclusive result[31] : $E_\gamma^* = 163.8$ MeV, $\Delta E_\gamma^* = 3.1$ MeV :

(E-8)

$$\mathcal{L}(\underline{A_\gamma}, A_\alpha, E_\alpha, A_\beta, E_\beta, B) = \exp\left[-(A_\alpha + A_\beta + A_\gamma + B)\right] \times$$

$$\prod_{i=1}^{N}\left(A_\alpha f(E_i|E_\alpha) + A_\beta f(E_i|E_\beta) + A_\gamma \cdot \int dE_\gamma \quad f(E_i|E_\gamma) \cdot \frac{1}{\sqrt{2\pi}\Delta E_\gamma^*} e^{-\frac{1}{2}\left(\frac{E_\gamma - E_\gamma^*}{\Delta E_\gamma^*}\right)^2} + \frac{B}{\Delta E}\right)$$

(for description of symbols see Eq.E-2)

The 90 % upper limit on the number of observed transitions A_γ was obtained by the same method as described for the natural line widths (see above). The results are given in section IV.5.

APPENDIX F. Study of Detector Resolution With Inclusive π° Signal

The energy resolution is one of relevant parameters involved in the fit of the χ_b lines performed in section IV.1. The energy resolution of NaI is known to vary with energy of the incident showering particle (E) as :

(F-1)
$$\frac{\sigma_E}{E} = \frac{\sigma_\circ}{\sqrt[4]{E}} \qquad \begin{array}{l} E \text{ in } GeV \\ \sigma_\circ = const \text{ (resolution at energy of 1 } GeV) \end{array}$$

This was verified with the Crystal Ball prototype (array of 54 crystals) exposed to electron beams with different energies at SLAC[107]. The intrinsic NaI resolution $\sigma_\circ \approx 0.9$ %[108] is difficult to achieve with a large detector in the experimental conditions of e^+e^- collisions. An effective resolution must be determined from the data. It was studied, for the Crystal Ball detector, with different reactions at SPEAR : from energies of 1.5-2.2 GeV, with Bhabha electrons, down to energies of 130-260 MeV, with the χ_c lines in the inclusive photon spectrum from the ψ' decays. A value of $\sigma_\circ$ was found in the range 2.2-2.8 %, depending on the reaction and shower selection criteria[10,105]. Results with 5 GeV Bhabha electrons at DORIS-II show the similar values : 2.5-2.7 %. As the calibration lever arm (i.e. beam energy) has considerably increased, a verification of this resolution in the range of hundreds of MeV is important. The χ_b lines in the inclusive and exclusive channels are much weaker relative to their charmonium analogs. Their widths are consistent with the expected energy resolution, but precise figures are difficult to obtain[31]. We used the inclusive $\pi^\circ \to \gamma\gamma$ signal in hadronic events recorded at DORIS-II to study the detector resolution.

The two photon mass formula :

(F-2)
$$m_{\gamma\gamma} = \sqrt{(P_{\gamma_1}^\nu + P_{\gamma_2}^\nu)^2} = \sqrt{2E_{\gamma_1}E_{\gamma_2}(1 - \cos\theta_{\gamma\gamma})}$$

involves measurements of photon energies, and directions as well. Therefore, the width of the π° peak in a two photon mass distribution depends on both the photon energy resolution and the photon direction resolution. Fortunately, a determination of these two contributions can be, to a large extent, decoupled. The observed peak width for slow π°'s is dominated by the energy resolution, whereas the angular resolution dominates for fast π°'s (see below).

The inclusive yield of slow π°'s is relatively small, thus we analyzed a large sample of 0.8 million hadronic events, which included Υ', Υ,continuum and Υ''' running.

A single bump connected region was accepted as photon if no hits in the tube chambers were matching its direction. A cut on the angle to the beam direction : $|\cos\theta| < 0.75$ ensured that all layers of the tube chamber system were available for this charged particle rejection. In addition, a soft pattern cut, E2, E13<0.98, against minimum ionizing particles (see Appendix C) was applied. The photon candidate had to be more than 30° away from the other energy bumps, to secure clean energy measurement.

The two photon invariant mass was calculated for all pairs of photon candidates. The distribution of two photon mass was studied in separate bins of two photon momentum (Fig.64) :

(F-3) $$P_{\gamma\gamma} = \sqrt{E_{\gamma\gamma}^2 - m_{\gamma\gamma}^2} \qquad E_{\gamma\gamma} = E_{\gamma_1} + E_{\gamma_2}.$$

Only data with $P_{\gamma\gamma} < 600$ MeV were analyzed to restrict photons to a low energy range. The width of the π° peak was measured in each momentum bin independently, by a fit of the gaussian signal over a polynomial background. Different background parametrizations and various fit ranges were tried. Final results were calculated by averaging results of all fits to the same spectrum.

A simple Monte Carlo model was developed to extract the energy resolution from these results. Monoenergetic π°'s, from the Ball origin, were generated with either $1 + \cos^2\theta$ or a flat angular distribution. A spread of e^+e^- interaction point along the beam direction was generated by a gaussian with $\sigma_z = 1.5$ cm (see section II.1). The π° momentum was set to the mean value of each momentum bin defined for the data. Directions of photons from the π° decays were limited to the same solid angle as for the real data. Photon energies were smeared according to the NaI energy response function (formula E-1), leaving the energy resolution σ_ε as a free parameter in the Monte Carlo model. The photon directions were smeared with the detector angular resolution described by the formula :

(F-4)
$$\sigma_\varphi = \frac{\sigma_\theta}{\sin\theta}$$
$$\sigma_\theta = \lambda \cdot \sigma_\theta^{EGS}$$
$$\sigma_\theta^{EGS} = a_0 - a_1 \cdot \ln E_\gamma \ \ 10 \text{ MeV}$$
$$a_0 = 0.061 \ rad \qquad a_1 = 0.0097 \qquad (for\ E_\gamma < 1500 \text{ MeV})$$

The formula for energy dependence was developed with EGS generated MC photons of different energies. The angular resolution scale factor λ was the second free parameter in our

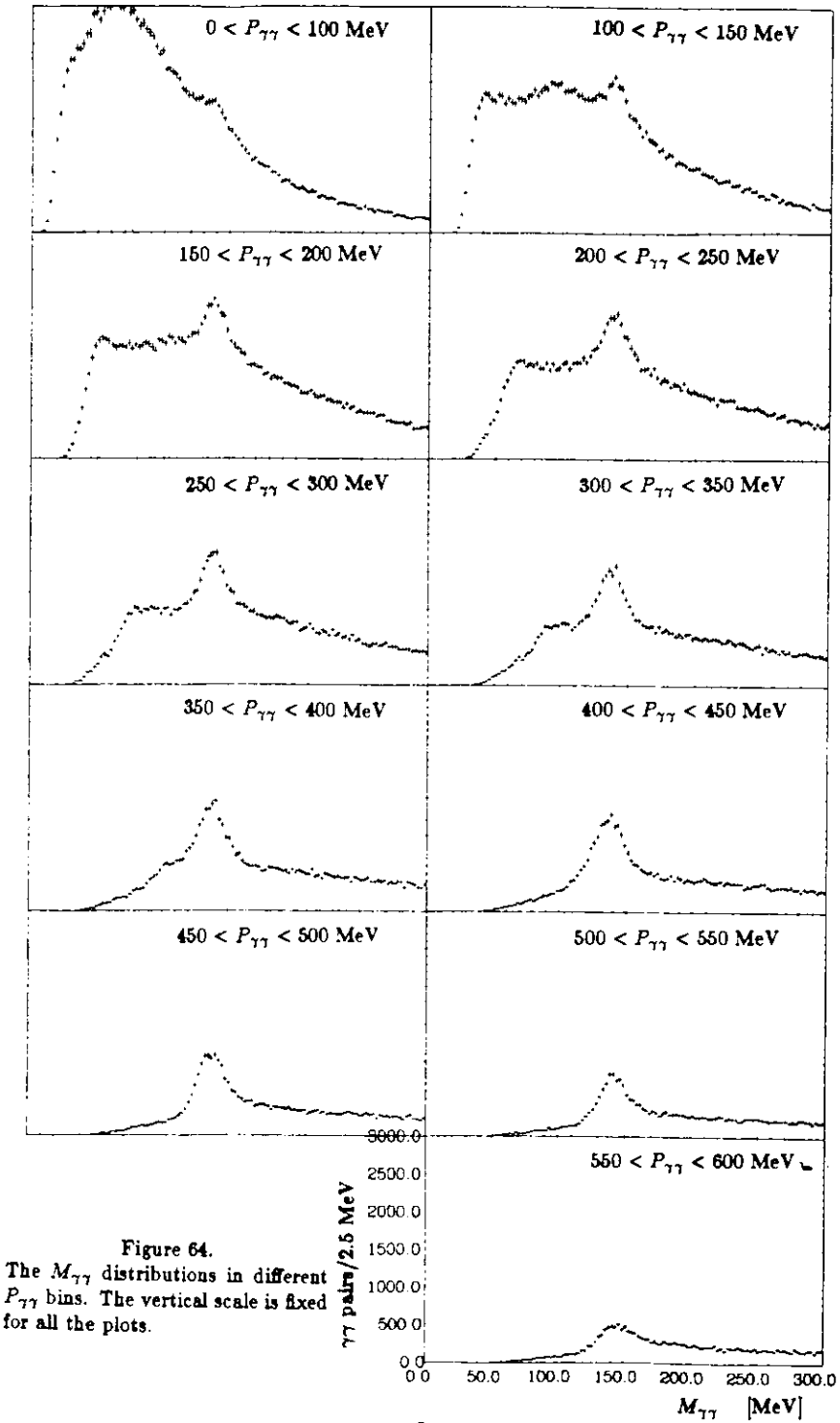

Figure 64.
The $M_{\gamma\gamma}$ distributions in different $P_{\gamma\gamma}$ bins. The vertical scale is fixed for all the plots.

Monte Carlo model, to be determined from the data. The value $\lambda = 1.0$, justifying the absolute scale from the EGS Monte Carlo, was expected.

The width of the Monte Carlo generated $m_{\gamma\gamma}$ distribution was compared to the experimental results in corresponding $P_{\gamma\gamma}$ intervals. A least-squares fit to the data of the energy resolution ($\sigma_\circ$) and the angular resolution (λ) was performed[1] :

(F-5)
$$\chi^2(\sigma_\circ, \lambda) = \sum_{i=1}^{11} \left(\frac{\sigma^{MC}_{\pi^\circ\, i}(\sigma_\circ, \lambda) - \sigma^{data}_{\pi^\circ\, i}}{\Delta\sigma^{data}_{\pi^\circ\, i}} \right)^2$$

i – counts the π° momentum bins

yielding $\sigma_\circ = 0.0279 \pm 0.0016$ and $\lambda = 1.02 \pm 0.04$ ($\chi^2/\mathrm{NDF} = 0.61$). The fit is displayed in Fig.65 Contributions to the observed π° width from the energy resolution alone and from the angular resolution alone are also indicated on the plot. Clearly, the width of the π° peak is sensitive to the value of $\sigma_\circ$ at low π° momenta and to the value of λ for the fast π° sample. The result for λ is fully consistent with the expectation from the EGS Monte Carlo.

The results are highly insensitive to the choice of the π° angular distribution model. The main systematic uncertainty comes from the details of the assumed NaI energy response function ($\Delta\sigma_\circ = \pm 0.0023$). The result $\sigma_\circ = 0.0279 \pm 0.0028$ (statistical and systematic errors have been added in quadrature) agrees well with resolution measured with Bhabha electrons at DORIS-II and with the old SPEAR results.

The energy resolution for exclusive events (e.g. $\gamma\gamma l^+ l^-$) may differ slightly from the value obtained here. It may be better because of the lack of the hadronic debris from the multi-hadron environment. On the other hand, inclusion of the tunnel region[2] for the photon detection in our exclusive analysis may degrade the average energy resolution.

[1] A computational problem of continuous free parameters in the Monte Carlo model was solved by the generation for fixed discrete values of $\sigma_\circ, \lambda$ and two-dimensional interpolation of the resulting $m_{\gamma\gamma}$ distribution width to arbitrary values of the resolution parameters.

[2] The energy resolution for the tunnel region crystals is worse due to the shower leakage at the ball edge and due to the degradation of the intrinsic resolution because of the high radiation doses at smaller angles to the beams.

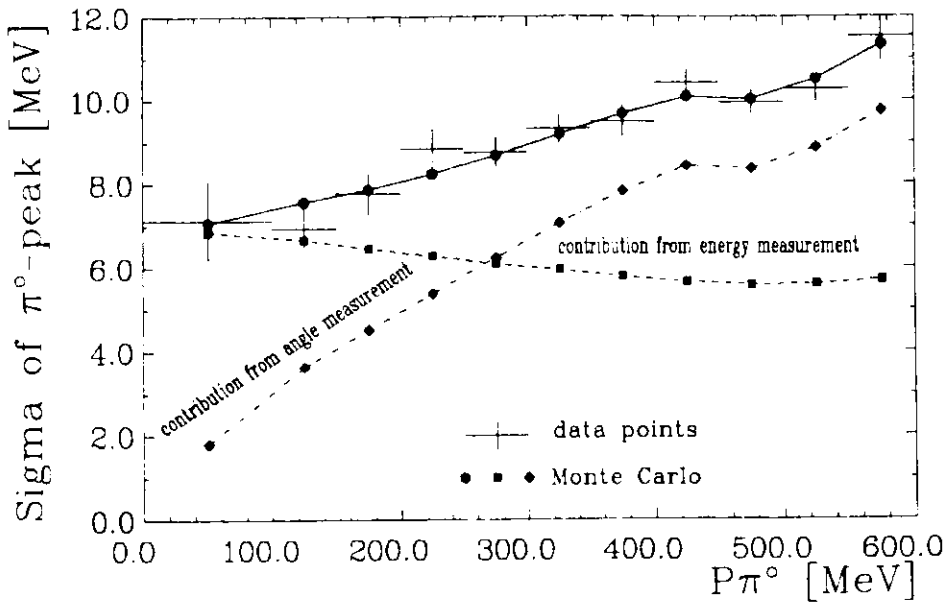

Figure 65.
The fit of $\sigma_\circ$, λ to the observed π° widths in different momentum bins. Strange behaviour of the data and MC points around 450 MeV is due to rapid "turn on" of the overlap cut between photons.

APPENDIX G. Beam Polarization Measurement

The DORIS-II beams are transversely polarized at the Υ' energy, as discussed in section II.1. This affected angular distributions in the azimuthal angle of the cascade reaction. The degree of beam polarization had to be known to utilize this φ-dependence for better discrimination between different χ_b spin hypotheses. As the beam polarization could vary from run to run depending on the particular storage ring set-up, an average polarization over the whole Υ' data taking had to be found. Well known QED reactions $e^+e^- \to \gamma\gamma$, $ee \to \mu^+\mu^-$ could serve that purpose. Events of the $e^+e^- \to \gamma\gamma$ type had to be distinguished from Bhabha scattering, $e^+e^- \to e^+e^-$. Thus, selection would be crucially dependent on the tube chamber performance. This would be rather disadvantageous, since the behaviour of the tracking device was very time dependent. Hence, we chose the $e^+e^- \to \mu^+\mu^-$ process.

Muon events were identified by strong pattern cuts ($175 < E13 < 250$ MeV, $E2/E13 < 0.96$) and collinearity requirement (9°).

The φ-dependence of the muon pair angular distribution for $\cos\theta < \cos\theta_c$ could be described, to a good approximation, by the lowest order QED formula :

$$\frac{\Delta N_\mu}{\Delta\varphi} \propto (1 + \frac{1}{3}\cos^2\theta_c) + P^2 \cdot \cos 2\varphi\,(1 - \frac{1}{3}\cos^2\theta_c) \qquad \text{(G-1)}$$

Selection of $e^+e^- \to \mu^+\mu^-$ events had to suppress cosmic ray background quite well, since it peaked at $\varphi = \pm\frac{\pi}{2}$, just at the places where Eq.G-1 exhibits polarization dependent minima. The ToF counters could not be used to separate out cosmics because of their limited azimuthal angle coverage. Time measurements from the NaI crystals themselves were used instead. Most of the cosmics were rejected by a cut on the mean ball timing relative to the beam crossing, as explained in Appendix A (see Fig.66). The rest of the cosmic background was removed by measuring the time difference between muon energy deposition in the upper and lower hemispheres ($T_{up} - T_{dn}$). The method was analogous to that using the ToF counters (Appendix C), however the direction of the muon flight had to be measured over a much smaller distance. Therefore, the annihilation and cosmic signals were not fully separated (Fig.67 – 69). Sacrificing half of the selection efficiency for $e^+e^- \to \mu^+\mu^-$ events, cosmic events were suppressed completely by a cut $T_{up} - T_{dn} \geq 0$ (see Fig.67,69). The residual cosmic background was estimated to be only 0.2 %. The φ-coordinate of the muons was

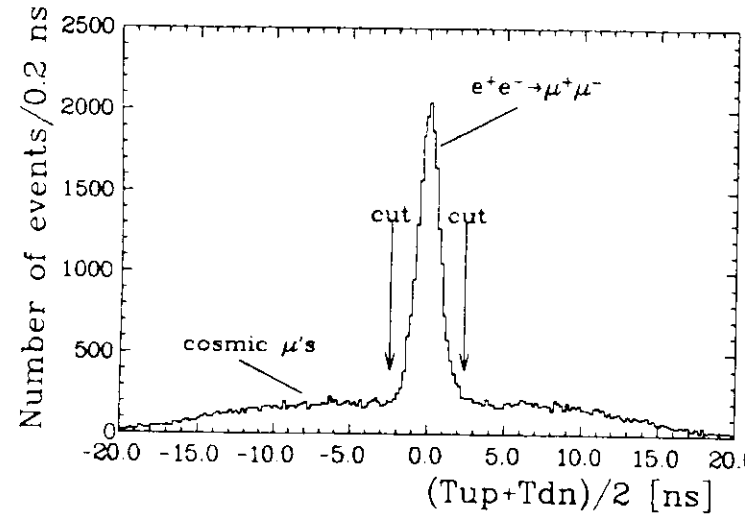

Figure 66.
The Ball timing distribution for μ-type events. The cuts used in the selection of annihilation muons for the polarization measurement are indicated. Tup, Tdn denote time of energy deposition in the upper, lower NaI hemispheres, correspondingly.

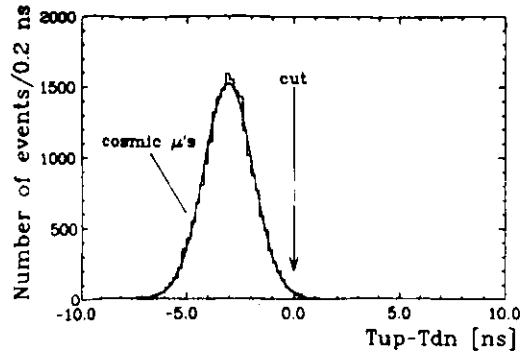

Figure 67.

The time difference between energy depositions in the upper (Tup) and lower (Tdn) Crystal Ball hemispheres for genuine cosmic muons identified by the ToF counters. The distribution peaks at −3 ns with $\sigma \simeq 1$ ns.
The cut used to reject cosmic background is indicated. Almost all cosmics are removed.

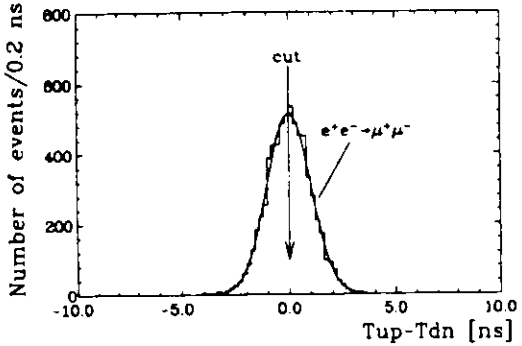

Figure 68.

The time difference between energy depositions in the upper (Tup) and lower (Tdn) Crystal Ball hemispheres for genuine $e^+e^- \rightarrow \mu^+\mu^-$ events identified by the ToF counters. The distribution peaks at 0 ns with $\sigma \simeq 1$ ns.
The cut used to reject cosmic background is indicated. Half of the efficiency for the annihilation muons is lost.

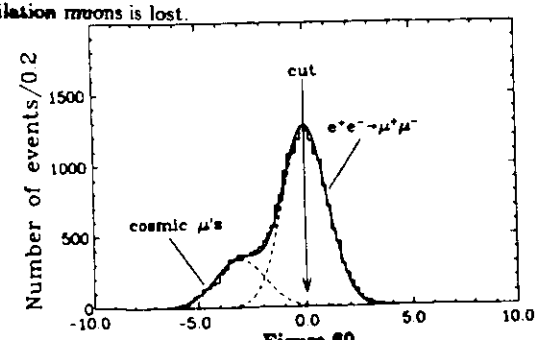

Figure 69.

The time difference between energy depositions in the upper (Tup) and lower (Tdn) Crystal Ball hemispheres for the μ-type events preselected for the beam polarization measurement. The Time of Flight cut is indicated. The fit of the cosmic and annihilation signals is shown. Positions and widths of the fitted curves were fixed at values obtained by the fits to the distributions showed in the previous two figures.

calculated from the positions of the corresponding tube chamber hits, or the bump module direction when no hits were recorded in the tracking chamber. A strong cut on the polar angle was applied ($\cos\theta_o = 0.4$) to enhance the polarization term in Eq.G-1. The muon φ-distribution for 3200 selected $e^+e^- \rightarrow \mu^+\mu^-$ events is shown in Fig.70. The fit of the formula G-1, indicated by the solid line, yielded (75 ± 3) %. Systematic uncertainties, due to the dependence on the fitting procedure, increased error on the above estimate to ±5 %. The obtained value is in good agreement with polarization measurement done by scattering of the laser light on the beams, performed for one of the Υ' runs[109]: P= (78 ± 7) %. For comparison, we show the azimuthal distribution of μ-pairs collected on the Υ resonance (Fig.71). The distribution is flat. The beam polarization is destroyed at this energy, because of a depolarizing machine resonance.

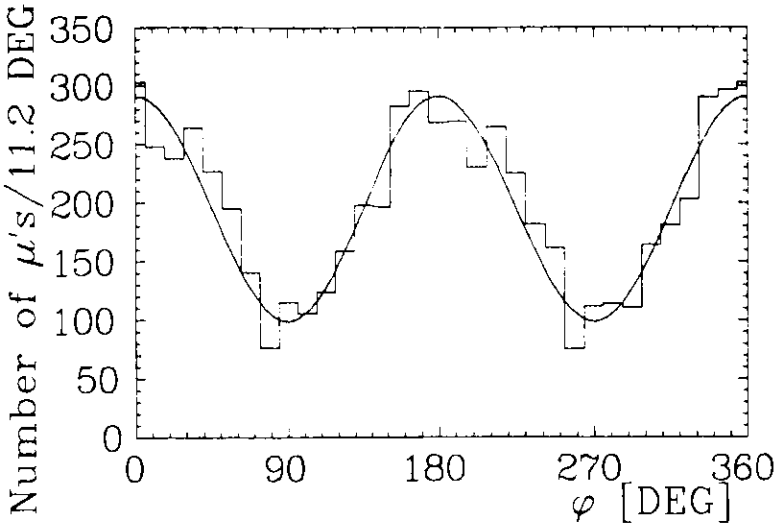

Figure 70.
The azimuthal angular distribution of muons from $e^+e^- \to \mu^+\mu^-$ annihilation at the beam energy of Υ'. The fitted value of the beam polarization, P= 75 %, corresponds to the solid line.

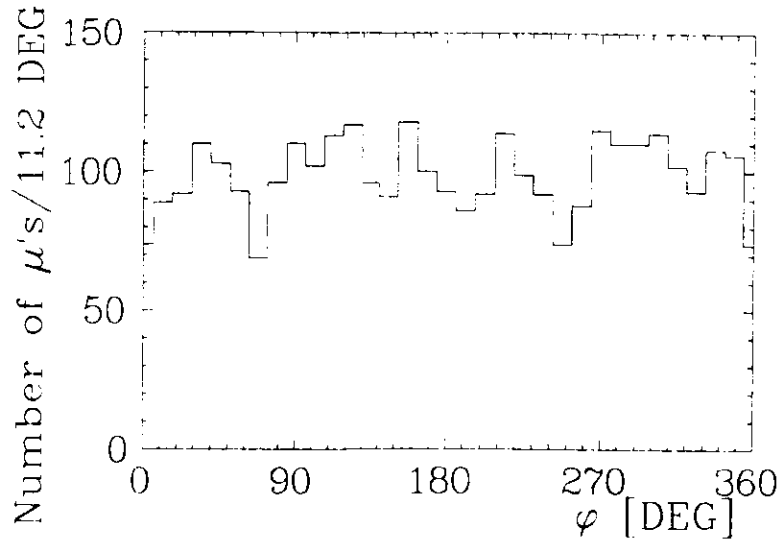

Figure 71.
The azimuthal angular distribution of muons from $e^+e^- \to \mu^+\mu^-$ annihilation at the beam energy of Υ. The data exhibit no beam polarization.

APPENDIX H. Systematic Effects in Spin Analysis

Uncertainty in the beam polarization value, feed down from the χ_b^β resonance to the χ_b^α sample, data contamination by the background processes, limited MC statistics and Gaussian approximation of the distributions of the test functions are the sources of the systematic errors in our spin analysis. Other systematic effects are small. For example, the results are highly insensitive to the details of the detector simulation.

The beam polarization assumed in the spin analysis was varied within experimental errors : P= (75 ± 5)% (Appendix G). The corresponding systematic error on a spin test result, expressed in standard deviations (SD), was estimated by :

(H-1)
$$\Delta_P^+ SD = \max\left[SD(P+\Delta P) - SD(P), SD(P-\Delta P) - SD(P), 0 \right]$$
$$\Delta_P^- SD = \min\left[SD(P+\Delta P) - SD(P), SD(P-\Delta P) - SD(P), 0 \right]$$

This was done for each spin test independently. Examples are shown in Fig.72.

To find out how events from the χ_b^β signal contributing to the χ_b^α sample might spoil the spin tests for the χ_b^α state, we added some admixture of the Monte Carlo (MC) predictions for J_β to the MC expectations for the clean J_α sample :

(H-2)
$$< T >_{J_\alpha + \epsilon_{fd} J_\beta} = (1-\epsilon_{fd}) < T >_{J_\alpha} + \epsilon_{fd} < T >_{J_\beta}$$
$$\sigma^2(T)_{J_\alpha + \epsilon_{fd} J_\beta} = (1-\epsilon_{fd})\sigma^2(T)_{J_\alpha} + \epsilon_{fd}\sigma^2(T)_{J_\beta}$$

where ϵ_{fd} denotes fraction of χ_b^β events in the χ_b^α sample. Values obtained with this formula were compared to the experimental value of the test function. For the J_α=1 hypothesis we used J_β=2, and for the J_α = 2 we assumed J_β=1. For the J_α = 0 hypothesis we did not study this kind of the systematic error, as we would have too many possibilities for a J_β spin. The test results for the χ_b^α data were studied as a function of the χ_b^β feed down. Fig.73 shows an example. The contribution to the systematic error was calculated by :

(H-3)
$$\Delta_{fd} SD = SD(\epsilon_{fd} = 0.12) - SD(\epsilon_{fd} = 0)$$

where the estimate of the feed down was taken from the fit to the E_γ^{low} spectrum, as explained at the beginning of chapter V.

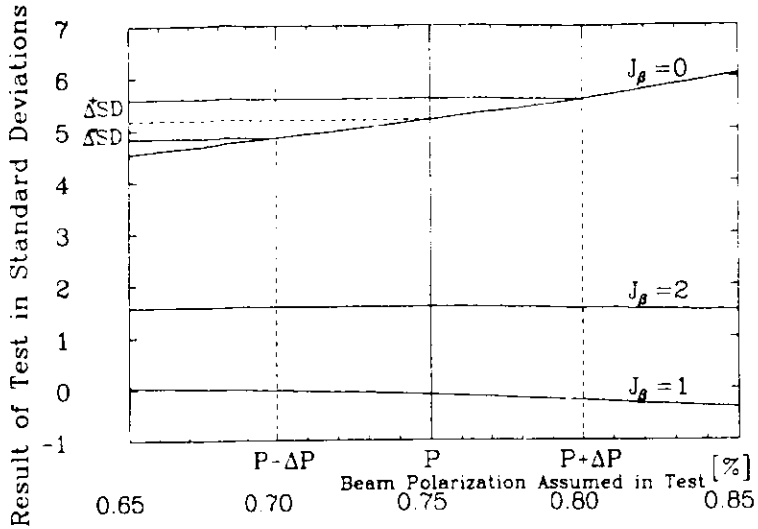

Figure 72.
The dependence of the spin tests using the likelihood for spin 0 for the χ_b^β sample on the assumed value of the beam polarization. The measured beam polarization is indicated by the vertical lines. The picture gives an example for the calculation of Δ_PSD (see text).

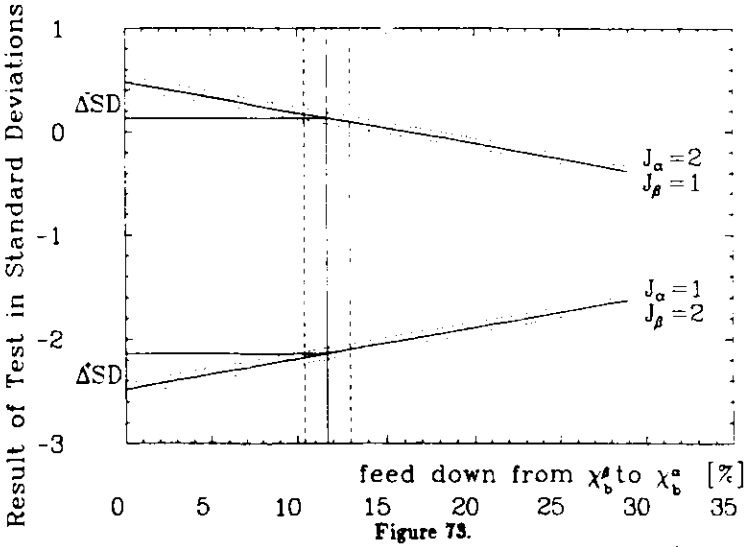

Figure 73.
The dependence of the likelihood ratio tests for the combined data of the χ_b^α and χ_b^β samples on the feed down from the χ_b^β signal to the χ_b^α sample. The vertical lines show the feed down estimated for our real χ_b^α sample. The dotted lines show uncertainties in the Monte Carlo calculations. The picture gives an example for calculation of Δ_{fd}SD (see text).

To study the influence of other background, a special background data sample was selected, as demonstrated in Fig.75. Behaviour of the test functions, applied to these events, was studied : $< T >_{bck}, \sigma^2(T)_{bck}$. Like in the feed down study, the clean MC predictions used in the spin tests were replaced by the background contaminated ones :

(H-4)
$$< T >_{J,\epsilon_{bck}} = (1 - \epsilon_{bck}) < T >_J + \epsilon_{bck} < T >_{bck}$$
$$\sigma^2(T)_{J,\epsilon_{bck}} = (1 - \epsilon_{bck})\sigma^2(T)_J + \epsilon_{bck}\sigma^2(T)_{bck}$$

Some expamples of dependence of the test results on the background contribution are shown in Fig.76. Again using the background estimate from the fit, we calculated :

(H-5)
$$\Delta_{bck}\mathrm{SD} = \mathrm{SD}(\epsilon_{bck} = 0.04) - \mathrm{SD}(\epsilon_{bck} = 0)$$

As a number of MC events was limited by available computer time, statistical fluctuations in the MC sample introduced additional uncertainty to the test results. Corresponding contribution, Δ_{MC}SD, was estimated from statistical errors on $< T >_J$ and $\sigma(T)_J$.

All systematic contributions ($\Delta_P, \Delta_{fd}, \Delta_{bck}, \Delta_{MC}$) were added lineary with appropriate sign to get total positive and negative systematic errors on SD and the corresponding confidence level. Additional systematic contribution due to the Gaussian scheme applied in our calculations was added. The deviation of the true distributions of T from their Gaussian approximations was studied with large MC sample of about 10^7 generated events for each spin hypothesis, J_{hyp}. The events were generated according to the theoretical angular distribution $W_{J_{hyp}}(\Omega)$. They were only subjected to the simple geometrical cuts and not to the full detector response simulation. Events passing all the cuts were grouped into MC experiments with a number of $\gamma\gamma\mu^+\mu^-$ and $\gamma\gamma e^+e^-$ events as in the real χ_b^α and χ_b^β samples. About $5 \cdot 10^5$ MC experiments were available for each spin hypothesis. A value of the test function was calculated for each MC experiment. Distribution of these values gave an estimate of the true distribution of the test function, independently of the Gaussian approximation. These distributions were compared to the Gaussians obtained with the same MC samples (see e.g. Fig.74). Assuming that deviations from the Gaussian distributions did not depend on those detector effects which were not simulated in this simplified MC scheme, we estimated a shift of the confidence level for each result,

(H-6)
$$\Delta CL(\mathrm{SD}) = CL^{\mathrm{non}}_{Gauss}(SD) - CL_{Gauss}(\mathrm{SD}),$$

which was added linearly to the negative or positive systematic error[1]. All spin results, presented in the section V.2, are summarized in Table 8, including systematic errors.

The systematic uncertainties, as can be seen from Table.8, are not large enough to alter our conclusions on the spin assignment to the observed χ_b states.

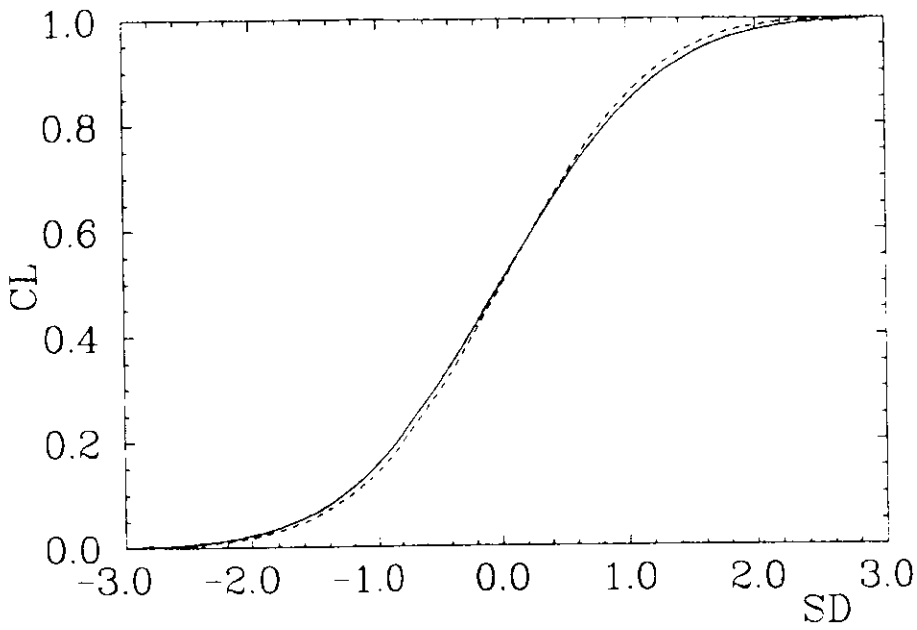

Figure 74.
Comparison between Gaussian confidence levels (solid curve) and confidence levels obtained from the MC simulation without Gaussian approximation (dashed curve) for the distribution of the test function V.2.e-1, $J_{hyp}=0$ and statistics like in the χ_b^a sample.

[1]The MC statistics used in this study were sufficient to probe with small statistical error confidence levels up to about $\pm 3\sigma$. For very high standard deviations we used as an error estimete an upper limit (at 90 % C.L.) on the confidence level difference, $\Delta CL(\mathrm{SD})$

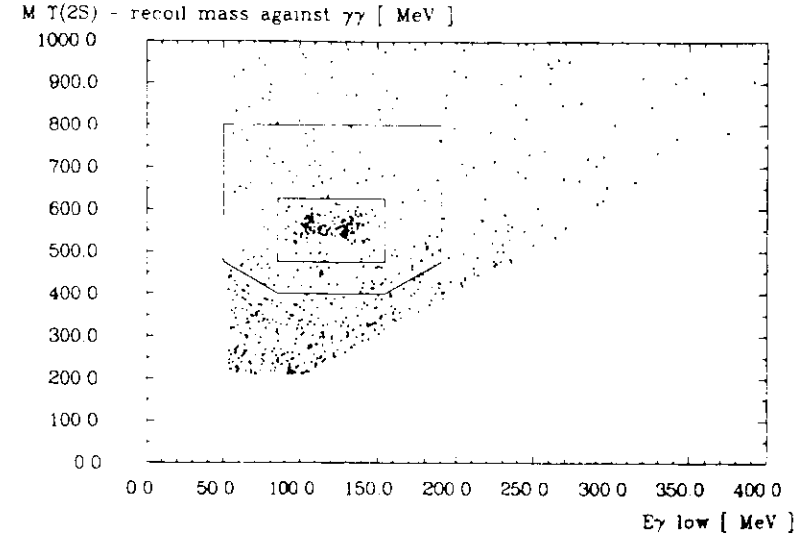

Figure 75.
The definition of the background sample for the study of the systematic errors in the spin analysis.

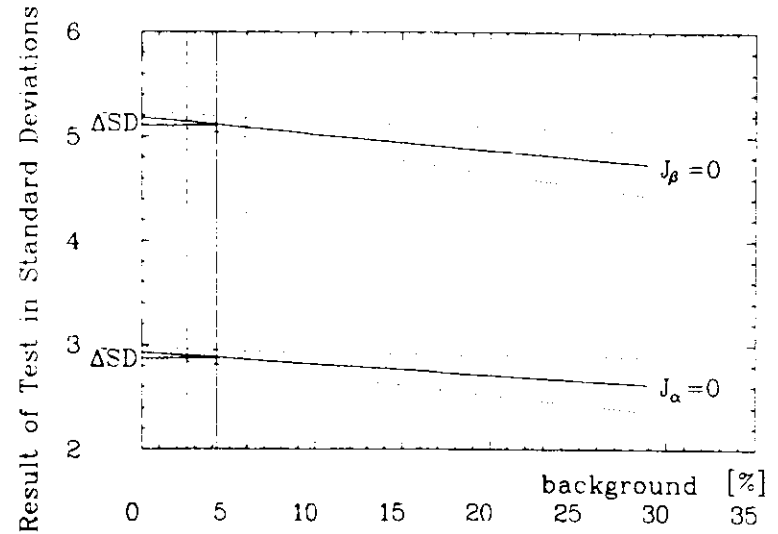

Figure 76.
The dependence of the spin 0 test for the χ_b^a and χ_b^β samples on the background level. The estimated background in the χ_b^α and χ_b^β samples is shown by the vertical lines. The dotted lines show uncertainties in the Monte Carlo calculations. The picture gives an example for the calculation of Δ_{bck}SD (see text).

APPENDIX J. Benefits of Beam Polarization

It has been pointed out[110] that polarized e^+e^- beams provide no additional information beyond that obtainable from unpolarized beams. However, there is an important experimental advantage of the polarized beams. We will discuss it here.

Let us consider[111] a polarization matrix of the Υ' for completely polarized beams (P=1). Choosing the z-axis along the polarization direction ($frame - \diamond$), it takes the form[1] :

$$\rho^\diamond = \begin{pmatrix} 0 & 0 & 0 \\ 0 & 1 & 0 \\ 0 & 0 & 0 \end{pmatrix} \tag{J-1}$$

It can be expressed as :

$$\begin{pmatrix} 0 & 0 & 0 \\ 0 & 1 & 0 \\ 0 & 0 & 0 \end{pmatrix} = 3 \begin{pmatrix} \frac{1}{3} & 0 & 0 \\ 0 & \frac{1}{3} & 0 \\ 0 & 0 & \frac{1}{3} \end{pmatrix} - 2 \begin{pmatrix} \frac{1}{2} & 0 & 0 \\ 0 & 0 & 0 \\ 0 & 0 & \frac{1}{2} \end{pmatrix} \tag{J-2}$$

The first matrix on the right side would lead to the isotropic decay, and the second one is the polarization matrix for unpolarized beams in the frame with z-axis parallel to the beam direction[2]. The decay angular distribution is uniquely defined by the spin density matrix of the parent state :

$$W^\diamond(\Omega^\diamond|\mathrm{P}=1) = 3W_I - 2W(\Omega^\diamond|\mathrm{P}=0) \tag{J-3}$$

where $W_I = \frac{1}{4\pi}$ is the isotropic angular distribution. Since the angular distribution for polarized beams can be uniquely predicted from the angular distribution for unpolarized beams, the beam polarization gives no new physics information.

However, it is still helpful from an experimental point of view. Every angular distribution can be expressed as a sum of isotropic and anisotropic terms :

$$W(\Omega) = W_I + W_A(\Omega) \qquad \int W_I \, d\Omega = 1 \qquad \int W_A(\Omega) \, d\Omega = 0 \tag{J-4}$$

[1]This can be shown, for example, from Eq.V.1-13, taking $\mathrm{P}=1, \psi'=0, \theta'=-\frac{\pi}{2}$.
[2]This again can be seen from Eq.V.1-13, by putting : $\mathrm{P}=0, \psi'=0, \theta'=0$.

Parameters of the angular distribution, for example χ_b spin, will show up in the anisotropic part. Applying Eq.J-4 to J-3 :

$$W^\diamond(\Omega^\diamond|\mathrm{P}=1) = W_I - 2W_A(\Omega^\diamond \ \mathrm{P}=0)$$
$$W_A^\diamond(\Omega^\diamond \ \mathrm{P}=1) = -2W_A(\Omega^\diamond \ \mathrm{P}=0) \tag{J-4}$$

we learn that the anisotropic term for polarized beams is twice as large as the one for unpolarized beams. This means that one would need 4 times as much data with unpolarized beams as for fully polarized beams to get the same accuracy in determining the parameters of the angular distribution.

An estimate of the gain in statistics for arbitrary polarization value is more difficult to obtain. Anyway, all our arguments hold only for the first $\Upsilon' \to \gamma\chi_b$ transitions. Strict results for the full cascade decay can be obtained from the Monte Carlo simulation. Fig.77,78 show the power of the tests we applied in section V.2.-e (for rejection confidence level of 1 %, see section V.2.d) as a function of the beam polarization. Clearly we would have had to run approximately twice as long with unpolarized beams to get similar spin results.

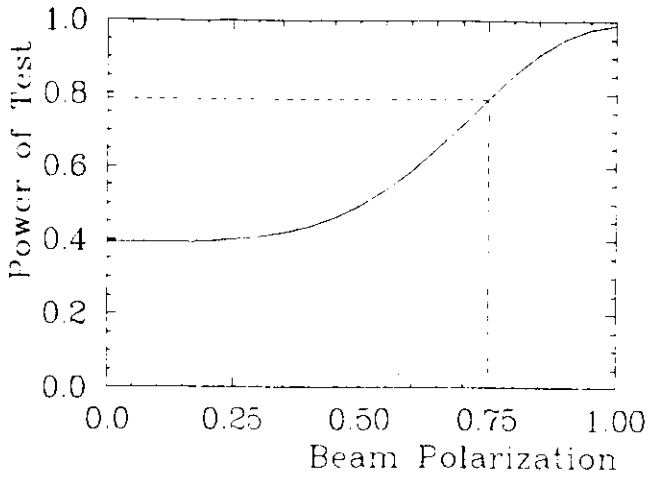

Figure 77.
The power of the spin 0 test at 1 % significance level for the spin 2 data sample (Monte Carlo study), with the statistics as observed in the real χ_b^2 sample, as a function of the beam polarization.

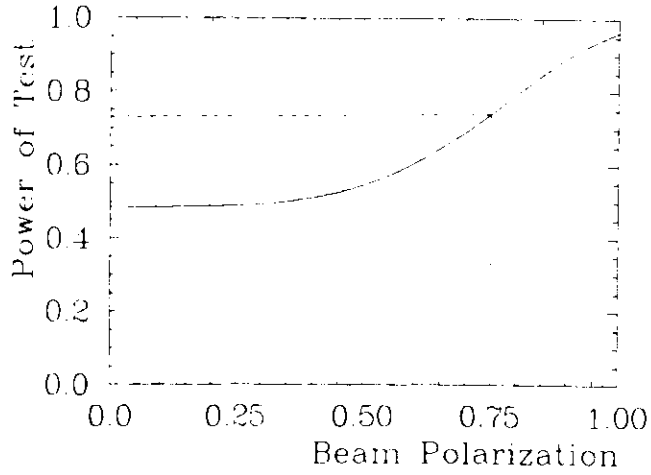

Figure 78.
The power of the likelihood ratio test of the $J_\alpha = 1$, $J_\beta = 2$ hypothesis at 1 % significance level for the $J_\alpha = 2$, $J_\beta = 1$ data sample (Monte Carlo study), with the statistics as observed in the real data χ_b samples, as a function of the beam polarization.

ACKNOWLEDGMENTS

The Crystal Ball experiment at DORIS-II, as all other high energy experiments, was possible only due to the joint effort of many people. I would like to thank all members of the Crystal Ball Collaboration for this effort and for years of friendly cooperation.

Special thanks go to Dr. W. Koch for many fruitful discussions on the analysis of the angular correlations. His ideas often proved important.

I appreciate the great assistance in writing this thesis up I have received from my promotor Prof. K. Rybicki.

Many thanks go to David Williams who had hard time making language corrections to this write-up.

I thank Dr. B. Niczyporuk for continuous encouragement and true support over many years.

I will never forget the hospitality and help of Prof. J. K. Bienlein during my stays at DESY. The same appreciation goes to Mrs. M. Bienlein.

I acknowledge Wim Walk for providing me the trigger simulation program, production of the Monte Carlo data at Nijmegen and many useful discussions on the data analysis.

I would like to thank the DESY directorate for its hospitality and financial support during the work on this thesis.

I am thankful to all my colleagues from High Energy Laboratory of the Cracow Institute of Nuclear Physics, the Filmless Detector Group especially, for friendship and support.

Finally, I would like to express appreciation to my wife, Małgosia, who has stood through all my education in physics from the early beginning.

REFERENCES

[1] J. J. Aubert et al., Phys. Rev. Lett. **33**, 1404 (1974).

[2] S. W. Herb et al., Phys. Rev. Lett. **39**, 252 (1977).

[3] T. Appelquist, H. Politzer, Phys. Rev. Lett. **34**, 43 (1975).

[4] S. Okobo, Phys. Lett. **5**, 165 (1963), G.Zweig CERN-TH-412,1964 (unpublished), J.Iizuka, Prog. Theor. Phys. Suppl. **37-38**, 21 (1966).

[5] C. Quigg, J. L. Rosner, Phys. Rep. **56**, 167 (1979).

[6] S. N. Gupta, S. F. Radford, W. W. Repko, Phys. Rev. **D26**, 3305 (1982).

[7] M. Krammer, H. Krasemann, Acta Phys. Austriaca, **Suppl. XXI**, 259 (1979).

[8] C. Berger et al., Phys. Lett. **76B**, 243 (1978), C. W. Darden et al., Phys. Lett. **76B**, 246 (1978), J. K. Bienlein et al., Phys. Lett. **78B**, 360 (1978), C. W. Darden et al., Phys. Lett. **78B**, 364 (1978), D. Andrews et al., Phys. Rev. Lett. **44**, 1108 (1980), T. Böhringer et al., Phys. Rev. Lett. **44**, 1111 (1980),D. Andrews et al., Phys. Rev. Lett. **45**, 219 (1980), G. Finocchiaro et al., Phys. Rev. Lett. **45**, 222 (1980),D. M. J. Lovelock et al., Phys. Rev. Lett. **54**, 377 (1985),D. Besson et al., Phys. Rev. Lett. **54**, 381 (1985).

[9] W. Buchmüller, G. Grunberg, S.-H. Tye, Phys. Rev. Lett **45**, 103 (1980), W. Buchmüller, S.-H. Tye, Phys. Rev. **D24**, 132 (1981).

[10] J. Gaiser, PhD thesis, Stanford 1982, SLAC-255.

[11] J. Gaiser, SLAC-PUB-2887 and New Flavors, (Proc. of Moriond Workshop, Les Arcs, France, Jan. 24-30, 1982), ed. Tran Thanh Van and L. Montanet, Editions Frontiéres, Gif-sur-Yvette, France, 1982, p.11., and Ref.10.

[12] R. Partridge et al., Phys. Rev. Lett. **45**, 1150 (1980). C. Edwards et. al., Phys. Rev. Lett. **48**, 70 (1982), and Ref.11

[13] K. Han. et al., Phys. Rev. Lett. **49**, 1612 (1982).

[14] G. Eigen et al., Phys. Rev. Lett. **49**, 1616 (1982).

[15] C. Klopfenstein et al., Phys. Rev. Lett. **51**, 160 (1983).

[16] F. Pauss et al., Phys. Lett. **130B**, 439 (1983).

[17] P. Haas et al., Phys. Rev. Lett. **52**, 799 (1984).

[18] H. Albrecht at al., DESY 85-068, 1985, to be published.

[19] Particle Data Group, Rev. Mod. Phys. **56**, No.2, Part II (1984).

[20] M. Oreglia, PhD thesis, Stanford 1980, SLAC-236.

[21] M. Oreglia et al., Phys. Rev. **D25**, 2259 (1982), and Ref.20

[22] DESY Storage Ring Group : DORIS, Proc. of the IXth International Conference on High Energy Accelerators, Stanford 1974.

[23] The DORIS Storage Ring Group, DESY 79-08 (unpublished).

[24] H. Nesemann, K. Wille IEEE Trans. of Nucl. Sci. **NS-30**, 1998 (1983) , DESY Internal Report DESY-M-83-09.

[25] D. P. Barber et al., Phys. Lett. **135B**, 498 (1984).

[26] A. A. Sokolov, I. M. Ternov, Sov. Phys. Dokl., **16**, 1203 (1964).

[27] D. P. Barber et al., DESY 83-065, (unpublished).

[28] D. P. Barber et al., DESY M-83-14, (unpublished).

[29] R. P. Horisberger, PhD thesis, Stanford 1984, SLAC-266.

[30] R. Nernst, PhD thesis, Hamburg University 1985, DESY Internal Report : DESY F31-85-01.

[31] R. Nernst et al., Phys. Rev. Lett. **54**, 2195 (1985), and Ref.30.

[32] D. Peterson, CLEO Collaboration, presented at the 1985 International Conference on Hadron Spectroscopy, Collage Park, Maryland, April 20-22, 1985.

[33] R. Ford, W. Nelson, SLAC-210 (1978)

[34] C. Edwards et al., SLAC-PUB-3030 (1983), and Ref.30.

[35] H. B. Henriques, B. H. Kellett, R. G. Moorhouse, Phys. Lett. **64B**, 85 (1976).

[36] L. S. Brown, R. N. Cahn, Phys. Rev. **D13**, 1195 (1976).

[37] G. Karl, S. Meshkov, J. L. Rosner, Phys. Rev. **D13**, 1203 (1976).

[38] L. A. Copley, G. Karl, E. Obryk, Nucl. Phys. **B13**, 316 (1969).

[39] G. Karl, S. Meshkov, J. Rosner, Phys. Rev. Lett. **45**, 215 (1980).

[40] B. Stugu (Fysisk Institutt, Universitetet I Oslo), private communication.

[41] W. Eadie et al., **Statistical Methods in Experimental Physics**, North-Holland Amsterdam (1971).

[42] W. Tanenbaum et al., Phys. Rev. **D17**, 1731 (1978).

[43] For a review, see J. Kuti, Proc. Lepton Photon Symp., Cornell University, edited by D. G. Cassel and D. L. Kreinick (1983).

[44] See, for instance, S. W. Otto, J. D. Stack, Phys. Rev. Lett. **52**, 2328 (1984).

[45] P. Moxhay, J. L. Rosner, Phys. Rev. **D28**, 1132 (1983).

[46] R. McClary, N. Byers, Phys. Rev. **D28**, 1692 (1983).

[47] J. L. Richardson, Phys. Lett. **82B**, 272 (1979).

[48] G. Bhanot, S. Rudaz, Phys. Lett. **78B**, 119 (1978).

[49] E. Eichten, F. Feinberg, Phys. Rev. **D23**, 2724 (1981).

[50] M. Bander, D. Silverman, B. Klima, U. Maor, Phys. Lett. **134B**, 258 (1984), Phys. Rev. **D29**, 2038 (1984).

[51] C. Quigg, J. L. Rosner, Phys. Lett. **71B**, 153 (1977), and Ref.5.

[52] R. Ram, R. Leon, Lett. Nuovo Cimento, **36**, 205 (1983).

[53] C. Quigg, J. L. Rosner, Phys. Rev. **D23**, 2625 (1981).

[54] R. Y. Levine, Y. Tomozawa, Phys. Rev. **D21**, 840 (1980).

[55] H. Krasemann, S. Ono, Nucl. Phys. 154B, 283 (1979), see also Phys. Rev **D29**, 110 (1984).

[56] A. Soni, M. D. Tran, Phys. Lett. **109B**, 393 (1982).

[57] M. Martin, Phys. Lett. **100B**, 511 (1981).

[58] A. Khare, Phys. Lett. **98B**, 385 (1981).

[59] O. Abe, H. Haruyama, A. Kanazawa Phys. Rev. **D27**, 675 (1983).

[60] S. Ono, Z. Phys. **C8**, 7 (1981), Phys. Rev. D20, 2975 (1979).

[61] H. F. De Carvalho, A. B. D'Oliveira, Lett. Nuovo Cimento **33**,572 (1982).

[62] J. R. Hiller, Phys. Rev. **D30**, 1520 (1984).

[63] J. S. Kang, Phys. Rev. **D20**, 2978 (1979).

[64] D. Beavis, S.-Y. Chu, B. R. Desai, P. Kaus, Phys. Rev. **D20**, 2345 (1979).

[65] W. Celmaster, H. Georgi, M. Machacek, Phys. Rev. **D17**, 879 (1978).

[66] K. Heikkilä, N. A. Törnqvist, S. Ono, Phys. Rev. **D29**, 110 (1984), S. Ono, N. A. Törnqvist, Z. Phys. **C23**, 59 (1984).

[67] G. Fogleman, D. B. Lichtenberg, J. G. Wills, Lett. Nuovo Cimento **26**, 369 (1979).

[68] D. Beavis, S.-Y. Chu, B. R. Desai, P. Kaus, Phys. Rev. **D20**, 743 (1979).

[69] D. B. Lichtenberg, J. G. Wills, Nuovo Cimento **47A**, 483 (1978).

[70] H. Crater, P. Van Alstine, Phys. Rev. Lett., **53**, 1527 (1984).

[71] J. Carlson, J. B. Kogut, V. R. Pandharipande, Phys. Rev. **D28**, 2807 (1983).

[72] H. Grotch, D. A. Owen, K. J. Sebastian, Phys. Rev. **D30**, 1924 (1984).

[73] D. P. Stanley, D. Robson, Phys. Rev. **D21**, 3180 (1980).

[74] E. Eichten, K. Gottfried, T. Kinoshita, K. D. Lane, T. M. Yan, Phys. Rev. **D17**, 3090 (1978), Phys. Rev. **D21**, 203 (1980).

[75] R. K. Bhaduri, L. E. Cohler, Y. Nogami, Nuovo Cimento, **65A**, 376 (1981).

[76] D. Pignon, C. A. Piketty, Phys. Lett. **74B**, 108 (1978).

[77] S. N. Jena, Phys. Lett. **123B**, 445 (1983).

[78] N. Barik, S. N. Jena, Phys. Rev. **D24**, 680 (1981).

[79] D. B. Lichtenberg, J. G. Wills, J. T. Kiehl, Phys. Rev. Lett. **39**, 1592 (1977).

[80] J. Baacke, Y. Igarashi, G. Kasperidus Z. Phys. **C13**, 131 (1982).

[81] E. Eichten et al., Phys. Rev. Lett **34**, 369 (1975).

[82] K. J. Miller, M. G. Olsson, Phys. Lett., **109B**, 314 (1982).

[83] M. A. Shifman, Proc. Lepton Photon Symp., Bonn, edited by W. Pfeil (1981).

[84] M. A. Shifman, A. I. Vainshtain, V. I. Zakharov, Nucl. Phys. **B147**, 385, **448**, 519 (1979).

[85] For a recent review, see L. J. Reinders, H. Rubinstein, S. Yazaki, preprint CERN-TH-4079/84 (1984).

[86] M. B. Voloshin, preprint ITEP-21 (1980), see also Ref.83.

[87] R. A. Bertlman, Nucl. Phys. **B204** 387 (1982).

[88] D. Gromes, Z. Phys. **C26**, 401 (1984).

[89] For the first attempt, see P. de Forcrand, J. D. Stack, Univ. of Illinois preprint, ILL-(TH)-85-37, June 1985.

[90] W. Buchmüller, Phys. Lett. **112B**, 479 (1982).

[91] W. Buchmüller, Y. J. Ng, S.-H. H. Tye, Phys. Rev. **D24**, 3003 (1981)

[92] See, for example, J. L. Rosner, Univ. of Chicago preprint, EFI-84-33 (1984), Invited talk given at the 6th International Symposium on High Energy Spin Physics, 12-19 September, 1984, Marseille, France.

[93] J. Baacke, Y. Igarashi, G. Kasperidus, Z. Phys. **C9**, 203 (1981).

[94] See, e.g., E. Remiddi, Proc. of Workshop on Physics at Lear, Erice, eds. U. Gastaldi and R. Klapish (1982).

[95] R. Barbieri, R. Gatto, E. Remiddi, Phys. Lett. **61B**, 465 (1976).

[96] T. Appelquist, R. M. Barnett, K. Lane, Ann. Rev. Nucl. Sci. **28**, 387 (1978).

[97] R. Barbieri, M. Caffo, R. Gatto, E. Remiddi, Nucl. Phys. **B192**, 61 (1981).

[98] P. B. Mackenzie, G. P. Lepage, Phys. Rev. Lett. **47**, 1244 (1981).

[99] M. G. Olsson, A. D. Martin, A. W. Peacock, Phys. Rev. **D31**, 81 (1985).

[100] S. N. Gupta, S. F. Radford, W. W. Repko, Phys. Rev. **D30**, 2424 (1984).

[101] K. Hagiwara, S. Jacobs, M. Olsson, K. Miller, Phys. Lett. **131B**, 455 (1983).

[102] D. Gelphman, PhD thesis, Stanford 1985, SLAC-286.

[103] L. Landau, Journal of Physics, **8**, 201 (1944).

[104] J. Berge, F. Solmitz, H. Taft, Rev. Sci. Inst. **32**, 538 (1961), O. Dahl, T. Day, F. Solmitz, N. Gould, Group A Programming Note No. P-126, Berkeley (LBL), July 1968.

[105] R. Lee, PhD thesis, Stanford 1985, SLAC-282.

[106] F. James, M. Roos, Computer Physics Communications **10**, 343 (1975).

[107] Y. Chan et al., IEEE Trans. on Nucl. Sci. **NS-25**, 333 (1978).

[108] E. B. Hughes et al., IEEE Trans. of Nucl. Sci. **NS-19**, 126 (1972).

[109] D. P. Barber et al., DESY Internal Report, M-83-15.

[110] Footnote 9 in Ref.36.

[111] W. Koch (Deutsches Electronen-Synchrotron DESY, Hamburg), private communication.